INVESTIGATION INTO THE TECTONIC SIGNIFICANCE OF THE ALONG STRIKE VARIATIONS OF THE PENINSULAR RANGES BATHOLITH, SOUTHERN AND BAJA CALIFORNIA

by

Paul H. Wetmore

A Dissertation Presented to the
FACULTY OF THE GRADUATE SCHOOL
UNIVERSITY OF SOUTHERN CALIFORNIA
In Partial Fulfillment of the
Requirements for the Degree
DOCTOR OF PHILOSOPHY
(GEOLOGICAL SCIENCES)

December 2003

Dedication

To Arturo and Celia Balbuena

"We make ourselves rich by making our wants few."
-Henry David Thoreau

Acknowledgements

The research reported in this dissertation was funded through numerous grants from the Geological Society of American, Sigma Xi, and the Department of Earth Sciences at the University of Southern California. Additional funding was provided by Keegan L. Schmidt and Scott R. Paterson through a grant from National Science Foundation (EAR9614682). A number of geochemical and geochronogical data were also donated by Jean Morrison, George Gehrels, Charles Herzig, and Mihai Ducea.

First of all, I'd like to thank my advisor Scott R. Paterson for lots of encouragement and for having more faith in me than I had in myself. I'd also like to thank him for gathering together such a large and diverse group as that represented by the Strain Group. There can be no substitute for the free exchange of ideas and that's what Scott creates with his group. I'd like to extend thank Jean Morrison for always being in my corner on my committee and always finding time to help me out. Especially near the end when her schedule grew very tight. I'd also like to thank William Weber for being the most interesting member of my committee. I knew from our first meeting that I'd made a wise choice in asking you to be my outside member.

There are also a number of other faculty members from the Dept. of Earth Sciences that I wish to thank for their contributions to my education and research. Greg Davis, you should know that I probably learned as much from our arguments as I did from any other aspect of my time at USC. Thank you for all the great classes, field trips, and discussions. Thanks also to Lawford Anderson for many great field trips to the Old Woman Mountains and discussions that didn't always have to do with the rocks. Thanks to David Bottjer for all your help with the Mesozoic time scale and the fossils of southern

and Baja California. Thanks to James Dolan for his insights into academia and for all those terrible jokes. Go Sox! Thanks to Bob Douglas and Donn Gorsline for some great trips to Baja and insightful discussion about Baja Geology. Sorry I had to drive so fast. Thanks to Steve Lund for some spirited and insightful discussions on the paleomag of the western Cordillera. Thanks to Ann Blythe for helping me with the mineral separations and for lots of interesting discussions. Special thanks are also extended to the office staff for always having the answers to my questions and taking the time to help me.

The work presented in this dissertation was also aided by a number of researchers. In particular I wish to thank Keegan L. Schmidt, James Faulds, Charles Herzig, Helge Alsleben, Paul Schultz, Robert Trzebski, Michelle Sutherland, Pedro Marenco, Melisa Paramo, Kurt Burmeister, and Geoff Pignotta. All of you donated either time or data or both to this project and I am forever in your debt because of it. I'd also like to thank David Kimbrough, John Fletcher, Francisco Suarez-Vidal, Jorge Ledesma, Richard Sedlock, Erwin Melis, and Scott E. Johnson for lots of insightful discussion of the Mesozoic geology of western Mexico. Thanks to Oscar Gonzalez for key logistical support and for an education in Baja life and culture.

On a more personal note, I've had the honor of being a member of the Strain group at USC and as such I've shared time with some the most interesting and inventive folks I've ever known. Thank you very much to Geoff Pignotta for all your help (there's far too much to enumerate here) over the past five years. Now get writing. Thanks to Michael "Michael Motorcycle" Potter, Helge "the Hel-gi-na-tor" Alsleben, Markus "Rattlesnake" Albertz, Gunnilla "Aunt Bunny" Andreasson, David "Teabag" Farris, Melissa "Missy" Boysun, and Luke "Loooke" Jensen for all the great discussions, and especially the good

times. Thanks to Brian "BJ" Darby for providing order around the lab refrigerator and all the good times. Thanks also to all the other graduate and undergraduate students in the Dept. of Earth Sciences who made my time here so much fun.

Special thanks are due to Arturo and Celia Balbuena who allowed me to stay with them every summer and shared with me their love and kindness.

Special thanks to my family for their love and support throughout the many, many years of my education. I miss you all and I hope you will us visit soon.

And finally, the greatest thanks of all are due to my wonderful and beautiful wife Melanie, without whom I would have left L.A. years ago without a degree. Thank you very much for all your patience and unyielding support. I Love You with all my heart.

TABLE OF CONTENTS

LIST OF FIGURES

LIST OF TABLES

ABSTRACT

The Mesozoic evolution of the Peninsular Ranges of southern California, USA and Baja California, Mexico remains a controversial aspect of Cordilleran tectonics with multiple, often mutually exclusive, models potentially viable. A fundamental reason for the lack of agreement between the proposed tectonic models is that they are based on one dimensional, arc perpendicular observations of the batholith from widely separated locations on opposite sides of the ancestral Agua Blanca fault, an active strike slip fault with an earlier Mesozoic history. North of the ancestral Agua Blanca fault, the Late Triassic through Jurassic was characterized by deep to moderately deep marine sedimentation of continentally-derived turbidite sequences of the Bedford Canyon Complex. These strata were deformed within an accretionary prism setting and were subsequently uplifted and beveled by subaerial erosion. During the Early Cretaceous the continental margin arc associated with the earlier-formed accretionary prism migrated westward and developed within and on the Bedford Canyon Complex.

South of the ancestral Agua Blanca fault Jurassic strata are only preserved locally in the central zone. During the Early Cretaceous this part of the arc subsided below sea level and became the site of turbidite sedimentation before being uplifted and dominated by the deposition of submarine, succeeded by subaerial volcanics derived from the continental margin arc present in the central and eastern zones. Outboard, the Alisitos arc, developed through and on oceanic crust, began to impinge upon the continental margin in the Early Cretaceous (~115 and 108 Ma). During accretion of the Alisitos arc across the Main Mártir thrust and ancestral Agua Blanca fault the Late Triassic-Jurassic accretionary prism (correlative to the Bedford Canyon Complex) was structurally

removed from between the arc and the continent by forcible subduction. If this model is correct, it implies that the Late Cretaceous uplift of the central zone of the Peninsular Ranges batholith, both north and south of the ancestral Agua Blanca fault, was not driven by accretion-related deformation at the trench.

CHAPTER 1: INTRODUCTION

Active continental margins are arguably, the most geologically complicated lithospheric systems on the planet. The vast majority of Phanerozoic crustal growth has occurred at active convergent plate boundaries as material is added to the overriding plate in the form of melts derived from the underlying mantle lithosphere/asthenosphere, and from the down-going plate, in the form of sediments, sea mounts, arc complexes and pieces of the oceanic crust/lithosphere. The addition of these materials, particularly those derived directly from oceanic plates, are commonly associated with the deformation of large regions resulting in crustal shortening/thickening and orogenesis.

The material added at subduction zones represents a geologically unique problem as the origins of the myriad of tectonic blocks accreted to continental margins are often difficult to constrain. This difficulty, in part, arises from lateral variations in the composition of tectonic blocks that become accreted, which is directly related to the spatial heterogeneity of geologic features (e.g., sea mounts) upon any oceanic plate, and any lateral variations in the proportion of material that is ultimately transferred to the overriding plate. Adding to the problem is the possibility of post-accretion removal/dislocation of all or parts of these tectonic blocks by a variety of processes including tectonic erosion along the interface between the subducting and overriding plates (e.g., Middle America Trench, Fisher et al., 1994), and the translational removal along; a) transcurrent faults that form to partition oblique convergence between two plates (e.g., Sumatra-Java arc, McCaffrey et al., 2000), or b) transform faults that form after the cessation of subduction (e.g., San Andreas, Suppe, 1970).

While identification of the transitions between preexisting continental margins and subsequently accreted materials has been facilitated by the results of regional mapping and geochemical studies, individual accreted tectonic blocks the structures juxtaposing them have not always been quite as easily delineated. In part, the lack of contrast between these blocks arises from the fact that most of tectonic elements formed on or are partly composed of oceanic lithosphere. This common origin fundamentally defines the petrochemical and geophysical compositions of these accreted tectonic blocks. As a result of this, it is possible that individual accreted tectonic blocks have been combined together thereby oversimplifying our understanding of their origins and evolutions.

Subduction of the Kula and Farallon plates defined the western and southwestern margins of North American during much of the Mesozoic and Cenozoic (Engebretson et al., 1985. As a result, a substantial proportion of western Cordillera is composed of accreted tectonic blocks as well as several large batholiths. Post-accretion removal/dislocation of portions of the western Cordillera occurred as a direct result of the termination of Farallon subduction as the San Andreas Fault formed between the North American and Pacific plates (Atwater, 1970). However, additional modification may also be attributed to subduction erosion and transcurrent dislocation (e.g., Schaaf et al., 1995; Irving et al., 1996). In southern California, and Baja California Norte, Mexico, the western half of the Baja Peninsula has long been interpreted to be composed of an accreted oceanic arc complex (e.g., Gastil et al., 1975). By contrast, the eastern side of the northern Baja Peninsula is interpreted to represent a fragment of pre-Mesozoic continental margin that, together with the western zone, was displace ~300 km northward

during the opening of the Gulf of California/slip along the San Andreas Fault(Gastil, 1993).

Several tectonic models have been proposed to explain the juxtaposition of the island arc assemblages of the western zone of the Peninsular Ranges with the continental margin of the eastern zone. These models derived from a variety of different types of studies (e.g., sedimentological, geochemical) from numerous locations north and south of the international border. Though many of the proposed models argue for an accretionary event to account for the juxtaposition of the two zones, not all models dissociate the western zone from the continental margin. For example, Walawender et al., (1991) and Kimbrough and Herzig (1994) argue that the western zone arc was built upon a preexisting join between the basements of the two zones. Others argue that the western zone was rifted from the North American margin only to be reaccreted during the late Early Cretaceous (e.g., Busby et al., 1998). The substantial differences between each of the proposed models notwithstanding, nearly all describe the entire western zone as a coherent tectonic block that evolved sympathetically throughout. A notable exception to this is a model proposed by Gastil et al. (1981) that divided the western zone into northern and southern arc segments separated by the trace of the active Agua Blanca fault.

The Gastil et al. (1981) model derived from the observations that while the Santiago Peak arc segment to the north of the Agua Blanca fault was characterized by a low gravity and magnetic signatures, and subarially-deposited volcanics that were believe to be Late Jurassic-Early Cretaceous, the Alisitos arc segment to the south was characterized by high gravity and magnetic signatures, and subaqueously-deposited

volcanics that were latest Early Cretaceous. Gastil and others still proposed that the entire western zone shared a similar early evolution as a rifted fringing arc but had subsequently reaccreted diachronously, Santiago Peak first.

The model proposed by Gastil et al. (1981) represents a point of departure for the study presented here. During the nearly two decades since the Gastil et al. model was proposed and the initiation of this investigation, several additional studies were completed and accompanied by tectonic models that typically ignored the observations that lead to the proposal of that earlier model. However, as these studies continued to accumulate so did the number of observed differences between the northern and southern parts of the western zone. Differences that seemed to be most pronounced across the Agua Blanca fault. Hence, in the fall of 1998 I, with the help of Scott R. Paterson, and Keegan L. Schmidt, began to compile all data sets bearing on the western zone of the Peninsular Ranges of southern and Baja California and, in the spring of 1999 began to map in the Agua Blanca fault. A number of additional researchers contributed to this study, not the least of which were two undergraduates from the University of Southern California, Paul S. Schultz, and Michelle Sutherland, who did mapping projects in the Peninsular Ranges as part of their senior research projects. As a result of this investigation I and my collaborators have proposed a vastly different model to explain the collection of observed differences north and south of the Agua Blanca fault.

The results of this investigation and the newly proposed model are present in the following three chapters. The first chapter, which is a paper published in the journal Geology (Wetmore et al., 2002), outlines the differences between the Santiago Peak and Alisitos arc segments and presents an early version of the tectonic model. Chapter three

is another paper accepted for publication in a Geological Society of America Special Paper in honor of Gordon R. Gastil. In this chapter the geologic details relevant to the middle Mesozoic evolution of the western and central parts of the Peninsular Ranges are described, including the results from the senior research study by Michelle Sutherland. The model present in chapter three differs from that of chapter two only in that it includes more detailed discussion on the origin and evolution of the central part of the Peninsular Ranges. Chapter four reports the results of the detailed mapping, strain, geochronology, and geochemistry from the Agua Blanca fault region. In particular, this chapter describes the deformation associated with the ancestral Agua Blanca fault, a southwest vergent ductile shear zone interpreted to be a suture between the two arc segments of the western zone.

The final chapter (five) in this dissertation reports the results of a satellite study of primary fabrics in volcanics and volcaniclastics. It relates directly to strain data collected from volcanics and volcaniclastics reported in chapter four of this dissertation. This study of primary fabrics represents a continuation of previous studies completed by Scott R. Paterson and coworkers (Paterson and Yu, 1994; Paterson et al., 1995) on immature sandstones and mudrocks. In addition to the description of grain preferred shapes and orientations, methods for primary fabric corrections are discussed. A manuscript form of this chapter has been submitted to the Journal of Structural Geology and is in review at present.

CHAPTER 2: TECTONIC IMPLICATIONS FOR THE ALONG-STRIKE VARIATION OF THE PENINSULAR RANGES BATHOLITH, SOUTHERN AND BAJA CALIFORNIA

Introduction

The Peninsular Ranges batholith (Fig. 2.1A) of southern and Baja California is the southern most segment of a chain of North American Mesozoic batholiths extending from Alaska to the tip of Baja. Similar to other segments of this chain, the Peninsular Ranges batholith is laterally zoned with a mafic western zone juxtaposed with a felsic eastern zone. The basement of the western zone (i.e., that through and upon which batholithic plutons and volcanics were emplaced) is inferred to be oceanic lithosphere (e.g., DePaolo, 1981). In contrast, the basement of the eastern zone is inferred to be transitional to continental crust. The timing of, and processes responsible for, the juxtaposition of these two disparate lithospheric types remains a controversial and unresolved issue in Peninsular Ranges geology.

Several tectonic models have been proposed to explain the Mesozoic evolution of the Peninsular Ranges batholith and the relationship of the western zone to the continental margin. These may be distilled down to two end members: (1) a single inboard-propagating arc developed across a pre-Triassic join between oceanic and continental lithospheres (Walawender et al., 1991; Thomson and Girty, 1994); and (2) an exotic island arc accreted to the continent between 115 and 108 Ma (Johnson et al., 1999a). We suggest that the differences between these models reflect tectonically significant along-strike variations in the character of the batholith. The study areas upon which each model

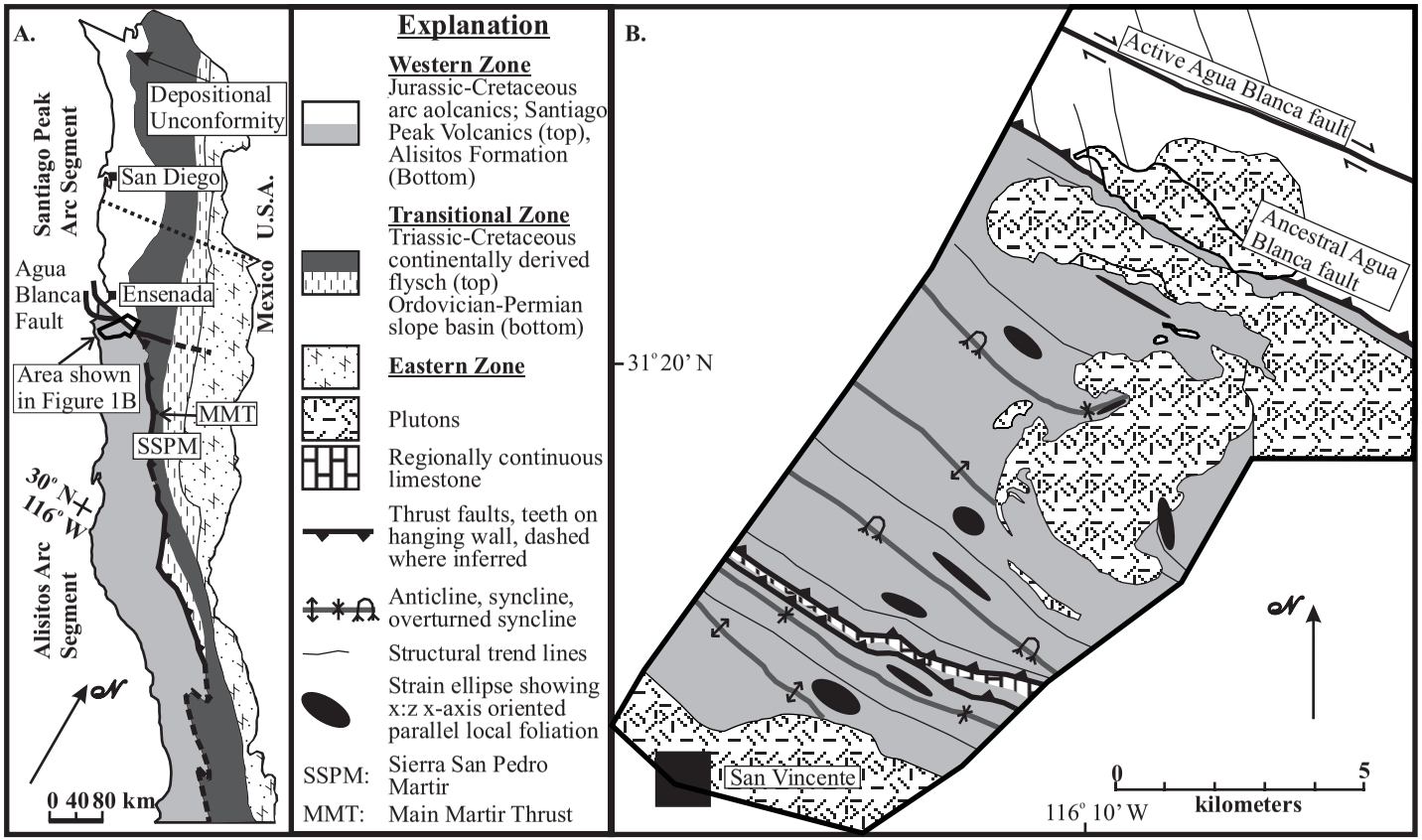

Figure 2.1. A) Tectonic map of the PRb showing the three zones of the batholith, component lithologies of the western and transitional zones, and the segments of the western zone. Modified from Gastil (1993). B) Preliminary geologic map of the San Vincent-Agua Blanca fault region of western Peninsular Ranges batholith.

is based are separated by the Agua Blanca fault, an active dextral strike slip fault that we suggest originated as a sinistrally transpressive fault during the Mesozoic evolution of the Peninsular Ranges batholith (Fig. 2.1A).

In this investigation we review the significant along-strike variations of the Peninsular Ranges batholith, propose a tectonic model that fits the disparate data sets from various parts of the batholith, and discuss some of the implications for this model.

Zonation of the Peninsular Ranges Batholith

The Peninsular Ranges batholith has traditionally been divided into distinct NW-SE trending zones delineated by a number of criteria, including prebatholithic stratigraphy, pluton composition, Fe-Ti oxide mineralogy, geochemistry, level of crustal exposure, and structural history. Given that these criteria are not all coincident in space but rather define a relatively broad zone, we propose that a transitional zone exists between typical western and eastern zones (Fig. 2.1A). Furthermore, based on recent investigations of Sierra San Pedro Mártir, it appears that the transitional zone had a distinct geologic history relative to regions to the west and east (e.g., Schmidt, 2000).

Plutons of the Peninsular Ranges batholith intrude a series of batholith-parallel, lithostratigraphic belts (Fig. 2.1A) that define the three zones of the batholith. Jurassic-Cretaceous arc volcanics and volcaniclastics compose the western zone, Triassic to Cretaceous continentally derived flysch and, locally, Ordovician-Permian slope basin deposits dominate the transitional zone, and Ordovician-Permian slope basin to Late Proterozoic-Paleozoic miogeoclinal assemblages characterize the eastern zone (Gastil, 1993). Western zone plutons are generally gabbros to granodiorites characterized by

depleted rare earth element (REE) abundances (Gromet and Silver, 1987) and primitive isotopic signatures (Taylor and Silver, 1978;DePaolo, 1981). Transitional and eastern zone plutons are generally granodiorites to granites characterized by eastward-increasing light REE enrichments and evolved isotopic signatures. The change from western to transitional and eastern zones also includes a change from punctuated weak to moderate deformation at shallow crustal levels (~2 kbar; Johnson et al., 1999b) in the western zone, to protracted intense deformation at deeper crustal levels (4-6+ kbar) in the transitional and eastern zones. However, a critical structure in the late Early Cretaceous evolution of the batholith is the ancestral Agua Blanca fault which is coincident with several significant along-strike variations to the character of western and transitional zones.

Santiago Peak Arc Segment and Adjacent Transitional Zone

The Santiago Peak arc segment extends from the Agua Blanca fault to the Transverse Ranges of southern California (Fig. 2.1A). The Santiago Peak Volcanics, the Jurassic-Cretaceous arc stratigraphy of this segment, yield Late Jurassic fossils (Fife et al., 1967) and U-Pb zircon ages that range from 138 to 120 Ma (Silver and Chappell, 1988), many samples exhibiting Precambrian inheritance. The volcanics are characterized by dense-welded, subarially deposited ridge-forming tuffs of mafic to felsic composition, rare interbedded sediments (Herzig, 1991), and a deep marine basin along the western side of the Santiago Peak arc in southern California (Balch et al., 1984).

The transitional zone adjacent to the Santiago Peak arc segment is relatively broad (>100 km) due both to laterally extensive exposures of continentally derived flysch (>50 km) and relatively gentle west-east geochemical gradients (e.g., Taylor and Silver, 1978).

The boundary between this arc segment and the transitional zone is not observed as tectonic. Kimbrough and Herzig (1994) reported a depositional unconformity between the flysch and the Santiago Peak Volcanics in the Santa Ana Mountains.

The southern part of the Santiago Peak arc segment exhibits little evidence to suggest displacement with respect to the transitional zone or the Agua Blanca fault. The boundary between the arc segment and the transitional zone is characterized by depositional contacts with little to no deformation. Similarly, the regional trends of strata and broad open folds are truncated by the west-northwest-trending Agua Blanca fault without significant deflection, increased strain intensity, or metamorphism (Fig. 2.1B).

Alisitos Arc Segment and Adjacent Transitional Zone

The Alisitos arc segment extends from the Agua Blanca fault to at least the Sierra Calamajue area, south of which it is covered by younger strata. The Alisitos Formation, the Jurassic-Cretaceous arc stratigraphy of this segment, yields Albian-Aptian fossils (Silver et al., 1963; Allison, 1974) and U-Pb zircon ages of 116 ± 2 Ma and 115 ± 1.1 Ma (Carrasco et al., 1995; Johnson, In press) without observed inheritance. The formation is characterized by poorly welded, subaqueously deposited tuffs, abundant interbedded volcaniclastics, a regionally extensive ridge-forming limestone, and locally abundant pillow basalts. Suarez-Vidal (1986) noted that the strata along the eastern side of the arc segment represent deposition in a tectonically calm marine environment.

The transitional zone adjacent to the Alisitos arc segment is fairly restricted in lateral extent (≤25 km; Fig. 2.1A) with limited exposures of the continentally derived flysch strata (≤10 km). The Main Mártir thrust (Fig. 2.1A; a prominent ductile, east-dipping,

west-vergent shear zone within a larger fold and thrust belt along this boundary) of the northern Sierra San Pedro Mártir, and its along-strike correlatives (Griffith and Hoobs, 1993; Schmidt, 2000), marks the lithologic, petrochemical, barometric, and structural boundaries between the arc segment and the transitional zone. These boundary faults also mark the western limit of all continentally derived material and form the only means of juxtaposition of such strata with the Alisitos Formation. Johnson et al. (1999a) defined the timing of this juxtaposition by the age of stitching plutons between 115 and 108 Ma.

The Alisitos arc segment exhibits evidence of substantial displacement with proximity to both the Main Mártir thrust and the Agua Blanca fault. The regional structural trend of the Alisitos arc segment, defined by folds axes and the strike of intraformational thrust faults of the southwest-vergent fold and thrust belt generally range between N15°W and N40°W (e.g., Johnson et al., 1999a). This trend is subparallel to that of the eastern boundary faults. Open folds, lower greenschist metamorphism, and low strain intensities (<20% shortening) in the western and central portions of the arc segment change to tight and isoclinal folds, lower amphibolite grade metamorphism, and intense strain (>60% shortening) along the eastern boundary (Fig. 2.1B; Schmidt, 2000). North of the Sierra San Pedro Mártir the fold and thrust belt exhibits a gradual rotation from subparallel to the Main Mártir thrust to subparallel to the Agua Blanca fault (i.e. N60°-65°W). Along the Agua Blanca fault, this fold and thrust belt is also characterized by increased metamorphic grade and strain, similar to that observed adjacent to the Main Mártir thrust (Fig. 2.1B).

Tectonic Implications

A comparison of the Alisitos and Santiago Peak arc segments defines several variations in the along-strike character of the western and transitional zones of the batholith. These include (Table 1): (1) age of magmatism; (2) existence of inherited zircons; (3) depositional environment of the arc strata; (4) location of extraarc basins; (5) lateral extent of the transitional zone and continentally derived flysch strata; (6) nature of the boundary between the arc segments and the transitional zone; and (7) character of deformation associated with the ancestral Agua Blanca fault. These variations are most pronounced across the Agua Blanca fault and, when taken together, imply profound differences in the tectonic evolution of the Peninsular Ranges batholith north and south of the fault.

Models suggesting a prebatholithic juxtaposition of the western zone with the continental margin (e.g., Walawender et al., 1991) are most applicable to observations made of the Santiago Peak arc segment and the adjacent transitional zone, where zircon inheritance and depositional contacts between the volcanics and the underlying flysch indicate that at least the eastern portion of the Santiago Peak arc segment must be developed through and on basement that included continental deposits. Furthermore, the lack of a discrete boundary (i.e., high strain/shear zone) between the arc segment and the transitional zone, or even synmagmatic basin strata preserved between the two zones and with the observed depositional contacts between volcanics and flysch clearly imply that the arc developed in situ and not as a rifted fringing arc.

Table 2.1. Variations between the two western zone arc segments

Arc segment	Santiago Peak	Alisitos
Age of Magmatism	130 to 120 Ma	117 to 108 Ma
Inherited zircons	Observed within both volcanics and plutonics	Not observed
Depositional environment of Jurassic-Cretaceous stratigraphy	Subarial	Submarine
Geography of extra arc basins	West of active arc	East of active arc
Lateral extent of flysch and transitional zone	Flysch ≤ 50 km Transitional zone ≤ 100 km	Flysch ≤ 5 km Transitional zone ≤ 25 km
Western to transitional zone boundaries	Depositional unconformity	Large ductile shear zone
Distribution of deformation	Distribution of deformation	Plutonic aureoles, along eastern and northern limits to the arc segment
Deformation associated with Agua Blanca fault	Deformation associated with Agua Blanca fault	Regional change in structural trend, high strain intensities and amphibolite grade metamorphism

In contrast, the exotic arc model is best supported by observations of the Alisitos arc segment and its adjacent transitional zone. The lack of observed zircon inheritance suggests that it did not develop through crust with a continental component. Similarly, the lack of observed depositional contacts between arc and continentally derived strata and the identification of a laterally continuous west-vergent ductile shear zone (e.g., Main Mártir thrust) that separates the two zones, suggests that this arc segment did not develop on basement that evolved juxtaposed to the continental margin.

If correct, then the following must be true. (1) A large proportion of the transitional zone currently adjacent to the Alisitos arc segment was tectonically removed from the margin. (2) The Agua Blanca fault originated as a continuation of the suture between the arc segment and the North American margin, here juxtaposing the two arc segments, it likely underwent sinistral transpression.

Several plutonic bodies <5 km east of the Main Mártir thrust yield ages between 133.9 ± 1.5 and 127.8 ± 1.6 Ma (Johnson et al., 1999a) and possibly as young as 118 ± 3 Ma (Schmidt, 2000). Thus, an arc, the southward continuation of the Santiago Peak arc, existed within the transitional zone just prior to the accretion of the Alisitos arc. However, the forearc to this arc is not preserved. The identification of juxtaposition of disparate lithospheric types such as that observed in the Sierra San Pedro Mártir suggests the potential for major strike-slip dislocations (e.g., Salmon River Suture, Idaho; Lund and Snee, 1988). Nevertheless, detailed structural studies in the Sierra San Pedro Mártir by Johnson et al. (1999a) and Schmidt (2000) identified little evidence to support arc-parallel translations. An alternative to translation is subduction of the forearc. This alternative is easily tested because forearc subduction may produce a geochemically observable signature identifiable through comparison of the transitional and eastern zone plutons north and south of the Agua Blanca fault.

If the Alisitos arc segment was exotic to North America then the Main Mártir thrust and its along-strike equivalents form a nonterminal suture (Dewey, 1977). Similar arguments must be true for the Agua Blanca fault since it juxtaposes two arc segments that were not related prior to accretion of the Alisitos. However, the fault strikes oblique to the axis of the batholith and thus must have undergone both contraction and sinistral translation. The observed counterclockwise rotation of the structural trends in the northern portion of the Alisitos arc segment away from subparallelism with the Main Mártir thrust and to subparallelism with the Agua Blanca fault is consistent with a deflection associated with a sinistral shear zone.

Summary

Several tectonic models have been proposed to explain the origin of the lateral zonation of the Peninsular Ranges batholith. However, these models typically fail to agree even on the most fundamental aspects of the timing and means by which the mafic western zone came to be juxtaposed with the continental margin. The differences in these models result partly from the observation that the western and transitional zones of southern and Baja California exhibit several along-strike variations in character that are most pronounced across the Agua Blanca fault. We propose a model (Fig. 2.2) that whereas the Santiago Peak arc segment developed on oceanic basement that had been structurally juxtaposed with the continental margin prior to arc magmatism, the Alisitos arc segment and its oceanic basement was exotic to North America prior to its accretion in the late Early Cretaceous. Santiago Peak basement served as a depositional substratum for material being shed from the continent during the early and middle Mesozoic evolution of the Peninsular Ranges batholith. Basins of similar composition and size probably extended the length of the batholith. However, accretion of the Alisitos arc segment implies that a significant proportion of these basins, which also formed the forearc to the southward continuation to the Santiago Peak arc, must have been removed, possibly through subduction. Furthermore, this diachronous accretion model also implies that the currently active Agua Blanca fault is an inherited structure that originated as a sinistral transpressional continuation of the suture that juxtaposes the Alisitos arc segment with the continent.

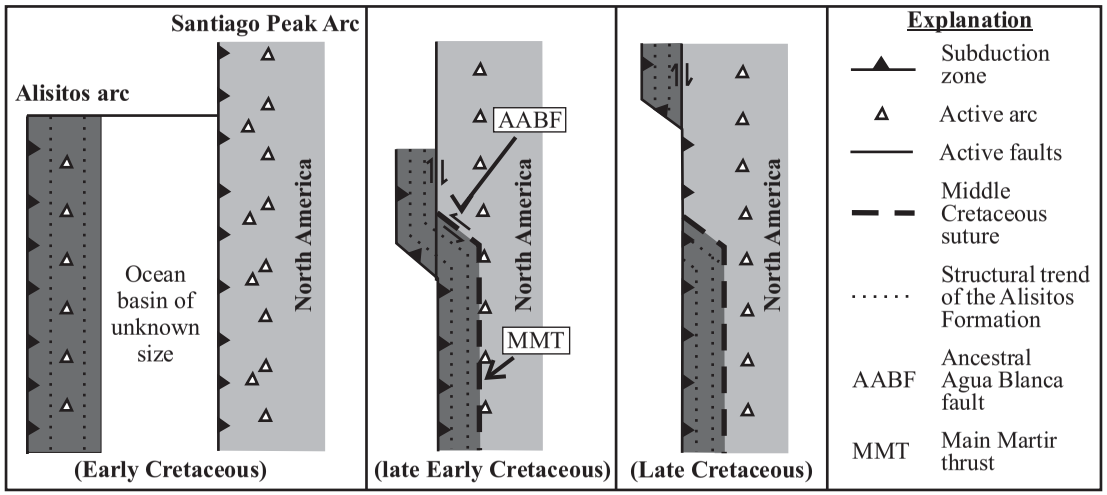

Figure 2. Tectonic model for Mesozoic evolution of Peninsular Ranges batholith.

CHAPTER 3: MESOZOIC TECTONIC EVOLUTION OF THE PENINSULAR RANGES OF SOUTHERN AND BAJA CALIFORNIA

Introduction

The Mesozoic tectonic evolution of the Peninsular Ranges province of southern California, USA and Baja California, Mexico remains a poorly constrained component of North American Cordilleran geology. Although a variety of tectonic models have been proposed, they differ in their most fundamental aspects, such as whether or not arc-continent collision occurred (e.g., Todd et al., 1988; Thomson and Girty, 1994). Differences between these models, at least in part, result from models being based on observations made in locations separated by faults that are interpreted to have been active during the Mesozoic. The presence of these faults calls into question the validity of extrapolating the findings of local, one dimensional studies to the entire Peninsular Ranges and beyond (e.g., Dickinson and Lawton, 2001). In order to address some of the long-standing geologic problems associated with the Peninsular Ranges we present a compilation of multiple data sets from several widely distributed parts of the central and western Peninsular Ranges to identify along strike variations in the character of this region and to provide better constraint to the Mesozoic tectonic evolution.

This study is an expansion of results reported in Wetmore et al. (2002). There, evidence was presented to support the conclusion that during the Early Cretaceous the western zone of the Peninsular Ranges (defined below) evolved as two distinct tectonic blocks, a continental margin arc to the north and an island arc to the south. The two arcs were ultimately joined due to the accretion of the southern island arc near the end of the

Early Cretaceous. In this paper the details of the Mesozoic depositional, structural, and paleogeographical evolution of the Peninsular Ranges are discussed to fully describe, evaluate, and justify the earlier proposed model.

Geologic Background

The geology of the Peninsular Ranges is intrinsically tied to the Peninsular Ranges batholith, which forms the core of this province. The Peninsular Ranges batholith is the southern most segment of a chain of North American Mesozoic batholiths that extend from Alaska to the southern tip of Baja California. It is exposed from the Transverse Ranges in southern California to as far as the 28th parallel. Recent studies have also correlated the intrusives of the Los Cabos block in southern most Baja California Sur with those of the Peninsular Ranges batholith to the north (Kimbrough et al., 2002). To the east the Peninsular Ranges batholith is bounded by the San Andreas-Gulf of California transform-rift system. To the west the batholith is bounded by the Continental Borderlands, a collage of Mesozoic rocks variably formed and deformed within trench, forearc, and arc tectonic settings (e.g., Sedlock et al., 1993). Paleogeographic relationships between the Continental Borderlands and the Peninsular Ranges are highly speculative due to the Mesozoic and Cenozoic history of a series of strike-slip faults within the Borderlands (e.g., Busby et al., 1998), some of which may coincide with active structures (e.g., Legg et al., 1991).

The Peninsular Ranges batholith is a world-class example of a laterally zoned batholith, with a mafic western (outboard) zone and a felsic eastern zone. Several data sets document the existence of east-west transitions between eastern, central, and western

batholith-parallel zones (Fig. 3.1). These data include rare earth elemental (REE) abundances (Gromet and Silver, 1987); oxygen isotopic signatures (Taylor and Silver, 1978); and Sr initial ratios and ε_{Nd} determinations from plutonic rocks (DePaolo, 1981). In addition, the Fe-Ti oxide mineralogy of the batholith exhibits an east-west transition where plutons of the western zone contain magnetite and ilmenite while those of the eastern zone contain the latter mineral phase (Gastil et al., 1990).

The above plutons intrude four major lithostratigraphic belts which parallel the long axis of the batholith (Gastil, 1993). These are, from east to west, Late Precambrian to Permian miogeoclinal strata, Ordovician to Permian (Early Triassic?) slope basin deposits, (Late?) Triassic to Cretaceous "back-arc" sedimentary rocks, and Jurassic(?) to Cretaceous arc volcanics. The Peninsular Ranges has thus been subdivided into three zones (eastern, central, and western), the trends of which parallel the batholith (Fig. 3.1). Typically the eastern zone includes miogeoclinal and slope basin deposits, the central zone "back-arc" sedimentary rocks, locally overlying slope basin strata, and the western zone volcanic arc rocks (Gastil, 1993).

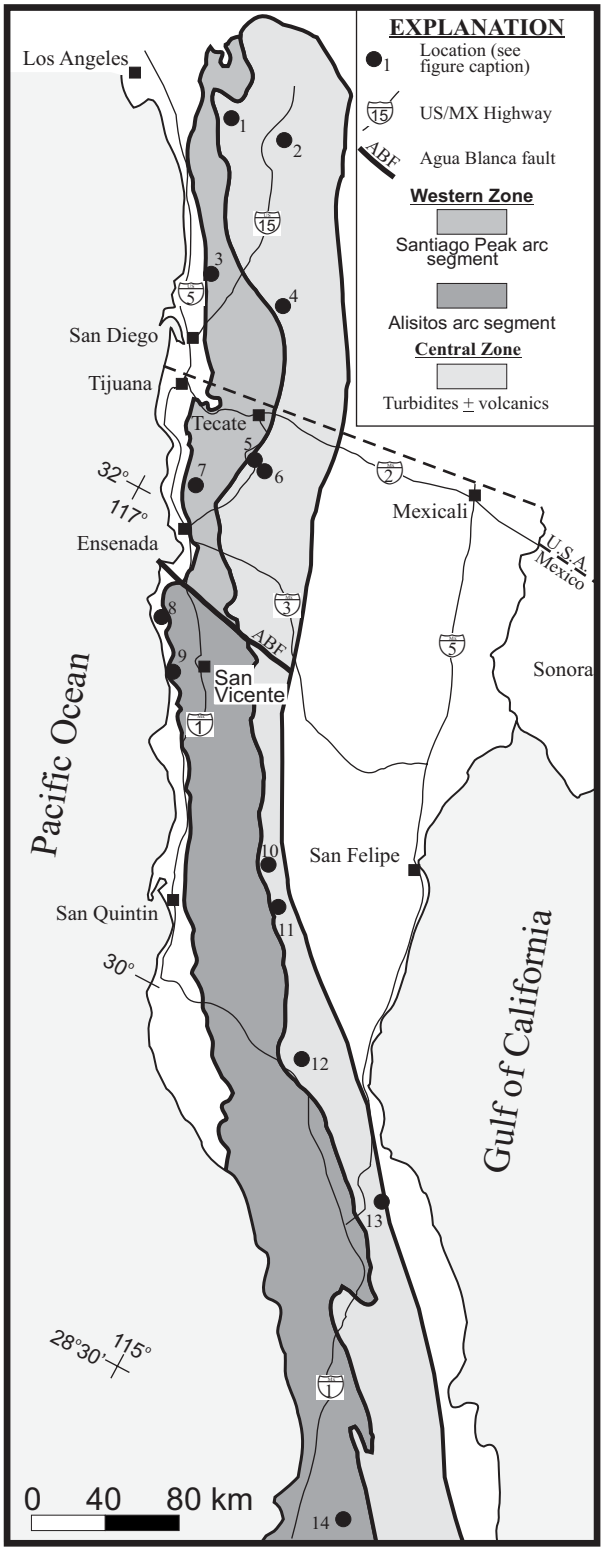

Figure 3.1. Map of southern California and Baja California Norte showing the western and central zones of the Peninsular Ranges batholith and localities discussed in the text (modified from Gastil, 1993). Locations: 1-Santa Ana Mountains; 2-Winchester area; 3-central San Diego County; 4-eastern San Diego County; 5-Rancho San Marcos; 6-Rancho Vallecitos; 7-Cañon La Mision; 8-Punta China; 9-Erendira; 10-northern Sierra San Pedro Mártir; 11-southern Sierra San Pedro Mártir; 12-El Marmol; 13-Sierra Calamajue; 14-El Arco.

These across-strike variations of the host rock stratigraphy and batholith have been interpreted to reflect a change in basement composition (e.g., DePaolo, 1981; Silver and Chappell, 1988), where the primitive western zone, with its island arc signature, is underlain by oceanic lithosphere, and the eastern zone is underlain by older lithosphere of continental composition. These observations and interpretations have provided the foundations for a series of tectonic models seeking to explain the juxtaposition of these disparate lithospheric types.

Tectonic Models for the Mesozoic evolution of the Peninsular Ranges batholith

The models most often proposed for the Mesozoic tectonic evolution of the Peninsular Ranges batholith may be distilled down to three end members: (1) a single eastward migrating arc developed across a pre-Triassic join between oceanic and continental lithospheres (Walawender et al., 1991; Thomson and Girty, 1994); (2) an exotic island arc accreted to the North American margin across a non-terminal suture (Johnson et al., 1999a; Dickinson and Lawton, 2001); and (3) the reaccretion of a rifted and fringing arc to the North American margin (Gastil et al., 1981; Busby et al., 1998).

Models requiring the western zone of the Peninsular Ranges batholith to have been initially rifted from the continental margin and subsequently reaccreted are generally based on regional observations of stratigraphy and structure. However, the specific geometric requirements a rift-reaccretion model implies are inconsistent with existing data sets. For example, a rift-reaccretion model requires that a basin form between the arc and the continental margin implying that the ages of strata should oldest within the

arc and the continent and youngest in the basin. However, as discussed below, the ages of the stratigraphy of the Peninsular Ranges decrease continuously toward the west.

The observations that led to the single migrating arc (Thomson and Girty, 1994) and exotic arc (Johnson et al., 1999a) models were derived from studies of the Peninsular Ranges batholith in southern California and the Sierra San Pedro Mártir, Mexico (Fig. 3.1), respectively. These two areas are separated by the Agua Blanca fault, an active dextral strike slip fault south of Ensenada, Mexico (e.g., Allen et al., 1960; Rockwell et al., 1989; Suarez-Vidal et al., 1991). Gastil et al. (1981), on the basis of observed differences in the apparent age and environment of deposition of the volcanics on either side of the Agua Blanca fault, identified it as an inherited structure with a Mesozoic origin as a transform fault. Gastil et al. (1981), thus, divided the western zone into northern and southern arc segments called the Santiago Peak and Alisitos, respectively. In their model the fault is interpreted as having accommodated the diachronous accretion of the two arc segments to the western margin of North American.

Since the Gastil et al. (1981) study our understanding of the geology of the Peninsular Ranges has improved substantially through numerous studies of the regional geology. However, few have followed up on the apparent discontinuity within the western and central zone of the batholith across the Agua Blanca fault. Here we focus on the along-strike variation in the Peninsular Ranges north and south of the Agua Blanca fault with particular attention paid to the temporal evolution of sedimentation and deformation within the central zone, and the structural relationships of the central zone strata to western zone volcanics. We will use these observations to constrain the tectonic evolution of the Peninsular Ranges batholith during the Late Triassic through the Early

Cretaceous, and will reevaluate recently proposed models (e.g., Busby et al., 1998; Dickinson and Lawton, 2001) for the Peninsular Ranges batholith evolution.

Peninsular Ranges North of the Agua Blanca Fault

The pre-batholithic stratigraphy of the central and western zones of the Peninsular Ranges north of the Agua Blanca fault range in age from Late Triassic through Early Cretaceous. They can be subdivided into pre-Cretaceous and Cretaceous groups, on the basis of general lithology, deformational history, and depositional setting. Those of the older group largely represent turbidite sequences (e.g., Germinario, 1993) subsequently deformed within an accretionary prism adjacent to the North American continental margin (e.g., Criscione et al., 1978). The Early Cretaceous sequences are generally the volcanic products of the western arc developed on and through the older accretionary prism.

Late Triassic through Jurassic: Turbidite sedimentation and deformation

Late Triassic through Jurassic sedimentary strata has been described from several locations in both southern and Baja California north of the Agua Blanca fault and have commonly been given local formational names. In the north, from west to east, these are the Bedford Canyon Formation, French Valley Formation, Julian Schist, and further south the Vallecitos Formation. We also include with this group the volcaniclastic-rich turbidite sequences of central San Diego County (Fife et al., 1967; Balch et al., 1984) west of exposures of the Julian Schist for reasons discussed below. Collectively, these

strata have long been interpreted to be a correlative group of deep to moderately deep submarine fan deposits (Gastil, 1993).

Bedford Canyon Formation. The Bedford Canyon Formation, exposed in the Santa Ana Mountains of Orange and Riverside Counties of southern California, is the most well studied of the middle Mesozoic turbidite sequences. The formation is dominated by alternating lithic and feldspar-rich sandstones (litharenites to lithic arkoses) and shales, with lesser amounts of limestone, conglomerate, chert, pebbly mudstones, and tuffaceous sequences (Moscoso, 1967; Moran, 1976). Additionally, isolated exposures of serpentinite occur along fault contacts within the formation (Moran, 1976; Criscione et al., 1978; Herzig, 1991). Deformation of the Bedford Canyon Formation is characterized by disrupted bedding, well-formed bedding-parallel foliation, and a second axial planar foliation associated with abundant tight to isoclinal folds, and ubiquitous small faults, typically subparallel to bedding and with some ramp-flat geometries.

The age of the Bedford Canyon Formation has been difficult to resolve because the formation is, in general, poorly fossiliferous with the exception of several allochthonous (olistostromal?) limestone blocks which contain Bajocian to Callovian (176.5 to 159.4 Ma) fossils (Silberling et al., 1961; Imlay, 1963, 1964; Moscoso, 1967). Moscoso (1967) noted that the ages of these fossils become older towards the east (Fig. 3.2). The age of deposition for the Bedford Canyon Formation, therefore, may be constrained as being between Bajocian (176.5 Ma, Gradstein et al., 1994) and the age of the overlying basal unit of the Santiago Peak Volcanics (127 ± 2 Ma; Herzig, 1991). Isotopic studies of the Bedford Canyon Formation are similar with a 175.8 ± 3.2 Ma Rb/Sr whole-rock isochron age (Criscione et al., 1978). The lower intercept age of 210 ± 49 Ma derived from a

mixed detrital zircon population (Bushee et al., 1963; Gastil and Girty, 1993) is also consistent with a Middle Jurassic age of deposition for the Bedford Canyon Formation.

French Valley Formation. The French Valley Formation crops out east of the Elsinore Fault near Winchester, California (Fig. 3.1). Immature sandstones and shales dominate within the French Valley Formation with lesser amounts of conglomerate and chert, as well as horizons composed of olistostromes (Schwartz, 1960), all indicative of a medium to deep submarine fan depositional setting. The French Valley Formation has been isoclinally folded and pervasively cleaved.

The age of the French Valley Formation may be Late Triassic as indicated by bivalves (Lamb, 1970). Detrital zircons yield a U/Pb lower intercept age of 285 ± 130 Ma (Gastil and Girty, 1993). However, a Rb/Sr whole-rock isochron age of 151 ± 11 Ma (Davis and Gastil, 1993) appears far too young and may reflect a subsequent metamorphic event rather than the age of deposition.

Julian Schist. The Julian Schist of eastern San Diego County (Fig. 3.1) is composed predominantly of sandstones and shales with minor amounts of carbonate and other lithologies (Germinario, 1993). The depositional environment, therefore, is inferred to have been within the distal and medial portions of a deep to moderately deep submarine fan. Unlike may of the other correlative formations the Julian Schist has been metamorphosed to amphibolite grade and strongly deformed resulting from the emplacement of multiple intrusives and multiple episodes of deformation associated with the Cuyamaca Laguna Mountain Shear Zone (Thomson and Girty, 1994).

The age of the Julian Schist is poorly constrained. Only one fossil has ever been reported from these strata, the imprint of an ammonoid that was interpreted to be Triassic

(Hudson, 1922). Unfortunately the sample was subsequently lost. U/Pb analyses of detrital zircons collected from the Julian Schist are strongly discordant with a poorly constrained lower intercept at ~260 Ma (Gastil and Girty, 1993). However, this lower intercept is at least consistent with the age of the Harper Creek gneiss, which had a tonalite to granite protolith (Leeson, 1989), and intruded the Julian Schist at 156 ± 16 Ma (Girty et al., 1993).

Contact relationships with younger stratigraphy, such as the Santiago Peak Volcanics, have not been described for the Julian Schist. Thus, correlation of tectonic events observed elsewhere (e.g., Santa Ana Mountains) cannot be unambiguously established in the eastern part of San Diego County.

Vallecitos Formation. Further south, the Vallecitos Formation, described from the Rancho Vallecitos and Rancho San Marcos areas in northern Baja California (Fig. 3.1; Reed, 1993), is characterized by lithologies and internal structures similar to that from other turbidite sequences further north. Reed (1993) interprets recrystallized sandstones and shales within the formation to have been deposited in the distal portions of a submarine fan. The presence of pebbly mudstones and large (5 km^2) olistostromal blocks of Ordovician miogeoclinal strata (Lothringer, 1993, Gehrels et al., 2002), further indicate proximity to a slope of the continental margin. U/Pb analysis of detrital zircons from these Ordovician strata by Gehrels et al. (2002) indicate a North American source providing a definitive tie between the Mesozoic turbidite sequences and the continent.

Deformation and metamorphism of the Vallecitos Formation is variable and largely dependant upon proximity to the multiple large intrusive bodies present near Rancho Vallecitos (Reed, 1993; Sutherland and Wetmore, unpublished mapping). Away from

intrusives recrystallization, cleavage, bedding-parallel faulting, and folding are perceived to be only slightly more intense than that observed of the Bedford Canyon Formation in the Santa Ana Mountains.

The age of the Vallecitos Formation, like that of more northerly formations, is not well defined. Gastil and Girty (1993) report the lower intercept of a mixing line formed from U/Pb analyses of detrital zircons collected from the formation to be 369 ± 59 Ma. A Rb/Sr whole-rock isochron age of 206 ± 12 Ma is suggested by Davis and Gastil (1993) indicating a possible Late Triassic age of deposition.

Tres Hermanos-Santa Clara area. The descriptions of the southernmost exposures of turbidite sequences north of the Agua Blanca fault are from the Tres Hermanos-Santa Clara area (Fig. 3.1; Chadwick, 1987). Sandstone and shale dominated strata of this area have been intruded by several plutonic bodies that have imparted a strong metamorphic overprint as well as a significant component of emplacement-related deformation. Chadwick (1987) reports the presence of earlier-formed northwest-trending structures that include tight and isoclinal folds and associated foliation within the turbidite sequences.

Isotopic ages for the Tres Hermanos-Santa Clara strata are similar to those described for the Vallecitos Formation. U/Pb analyses of detrital zircons yield a lower intercept of 302 ± 61 Ma and a Rb/Sr isochron age of 167 ± 9 Ma (Chadwick, 1987), suggesting a slightly younger Early Jurassic age of deposition. The age of intrusive bodies within these strata are all Early Cretaceous (132 ± 1.25 Ma or younger; Chadwick, 1987),

approximately the same age as the Santiago Peak Volcanics, and thus, do not constrain well, the age of these pre-Cretaceous strata.

Central San Diego County volcaniclastics. Exposed in central San Diego County (Fig. 3.1) are a series of volcaniclastics, deposited in a submarine environment (named the Santiago Peak volcaniclastics by Balch et al. (1984)), that have long been correlated with the Santiago Peak Volcanics (Fife et al., 1967; Balch et al,. 1984). Based on depositional environment, structural relationship to younger volcanic sequences, and age of these strata, we believe that they are better correlated with the pre-Cretaceous continentally derived turbidite sequences (e.g., the Bedford Canyon Formation) for reasons discussed below.

These volcaniclastics are epiclastically reworked breccias composed of andesites, dacites, and latites of similar composition to the Santiago Peak Volcanics. However, the deposits are exposed in sections containing turbidites, sandstones, and shales interpreted to have been deposited in medial to distal submarine fans (Balch et al., 1984) similar to those of the Bedford Canyon Formation. The Santiago Peak Volcanics, sensu-stricto, on the other hand are interpreted to have been deposited in a subaerial environment.

The volcaniclastic-rich sandstones and shales in central San Diego Country are characterized by a penetrative bedding parallel foliation, tight and locally overturned(?) folds, and brittle faults, all of which are truncated along the structural top of the section by an erosional surface. Overlying these volcaniclastic-rich turbidite sequences across an angular unconformity are volcanics that dip moderately and do not possess the deformational features of the underlying volcaniclastic and turbidite sequences. This relationship is remarkably similar to that observed between the Bedford Canyon

Formation and the Santiago Peak Volcanics in the Santa Ana Mountains (described below).

Fife et al. (1967) established the age of the strata in central San Diego as Tithonian based upon the presence of the fossil *Buchia Piochii*. A recent U/Pb zircon age of ~152 Ma from a volcanic flow (dike?) within the package of volcaniclastic-rich turbidites is consistent with the fossil age (Anderson, 1991). Thus, given that the basal unit of the Santiago Peak Volcanics in the type section of the sequence yields an age of 127 ± 2 Ma (Herzig, 1991), correlation between the strata of central San Diego County and the Santiago Peak Volcanics is unfounded and a more appropriate correlation is made with the Bedford Canyon Formation.

The above descriptions of the turbidite sequences of the central zone north of the Agua Blanca fault reveal consistent features throughout this region. These include similar lithologies and inferred depositional environment, style and magnitude of deformation, presence of olistoliths, detrital zircon populations that indicate a source that included Precambrian to Triassic exposures, and a general depositional age that ranges between Late Triassic and Jurassic. The identification of volcaniclastic layers within these strata is common only within those formations clearly identified as being deposited in the Jurassic (e.g., Bedford Canyon Formation and the volcaniclastic-rich turbidite sequences of central San Diego County). Additionally, a general east to west younging of the strata is indicated for the southern California sequences. That is, the French Valley Formation that contains Early Triassic fossils is east of the Bedford Canyon Formation which is Jurassic and which exhibits an intraformational westward younging (Bajocian on the east to Callovian on the west; Fig. 3.2). Similarly, the Triassic Julian Schist in

eastern San Diego County is east of the volcaniclastic-rich turbidites of central San Diego County, which yield Tithonian fossils. Because of the similarities between all of these formations, we propose that they should be incorporated under a single group herein named the Bedford Canyon Complex.

Early Cretaceous: Development of the Santiago Peak Arc

The Early Cretaceous arc volcanic strata of the western zone north of the Agua Blanca fault are dominated by the Santiago Peak Volcanics. Rocks of similar stratigraphic position, such as the Estelle Mountain Volcanics, exposed east of the San Andreas Fault east of the Santa Ana Mountains, (named the Temescal Wash quartz latite porphyry by Larsen, 1948), possess almost identical ages, contact relationships, petrologies, geochemistries, and degree of deformation to those described for the Santiago Peak Volcanics (Herzig, 1991). Hence, it seems practical to include all such units with the Santiago Peak Volcanics.

The most extensive studies of the Santiago Peak Volcanics have been completed in the Santa Ana Mountains (Larsen, 1948; Peterson, 1967; Gorzolla, 1988; Herzig, 1991), and central and northern San Diego County (Hanna, 1926; Adams, 1979; Tanaka et al., 1984; Anderson, 1991; Reed, 1992; Carrasco et al., 1993). South of the international border, where exposures are substantially better than to the north, studies have been completed in Cañon La Mision (Meeth, 1993) and the Ensenada area (Schroeder, 1967). Together these studies provide a relatively coherent picture of the volcanic products of the Early Cretaceous arc that existed along the western side of the Peninsular Ranges batholith north of the Agua Blanca fault.

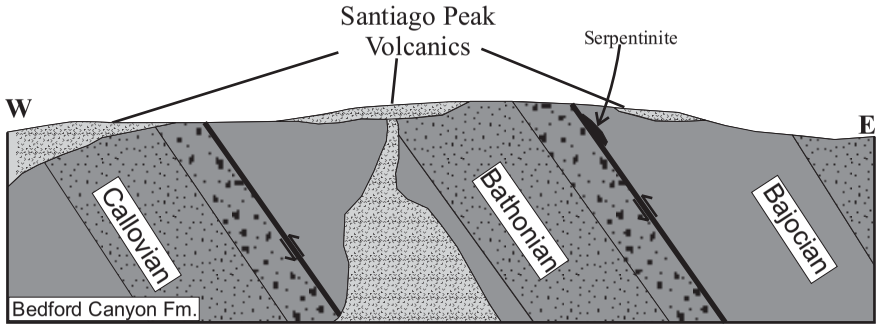

Figure 3.2. Schematic cross section through the Santa Ana Mountains based on our own field observations and age constraints from Moscoso (1967).

Lithology and Petrochemistry of the Santiago Peak Volcanics. The Santiago Peak Volcanics are composed of flows, volcaniclastic breccias, welded tuffs, hypabyssal intrusions, and relatively rare epiclastic deposits (Larsen, 1948; Schroeder, 1967; Adams, 1979; Gorzolla, 1988; Herzig, 1991; Reed, 1992; Carrasco et al., 1993; Meeth, 1993). The volcanics are inferred to be subarially deposited based on the abundance of accretionary lapilli, and preserved paleosols, as well as the apparent absence of pillow lavas, thick and laterally extensive epiclastic deposits, and other marine deposits.

A relatively large body of geochemical data exists for northern exposures of the Santiago Peak Volcanics (e.g., Hawkins, 1970; Tanaka et al., 1984; Gorzolla, 1988; Herzig, 1991; Reed, 1992; Meeth, 1993), and, when combined with that for intrusive bodies from the same arc segment (e.g., Taylor and Silver, 1978; DePaolo, 1981; Gromet and Silver, 1987; Silver and Chappell, 1988; Carollo and Walawender, 1993) a coherent picture of the generation and evolution of magmas from the region may be drawn. Many of the early geochemical investigations focused on the intrusive suites and variations in the REE and isotopic compositions across the batholith (e.g., Taylor and Silver; 1978; DePaolo, 1981; Gromet and Silver, 1987). These studies identify a relatively primitive western zone underlain by oceanic lithosphere juxtaposed with a relatively evolved central/eastern zone underlain by transitional to continental lithosphere.

Major and trace element, as well as isotopic data from the Santiago Peak Volcanics indicate that they, like the plutons that intrude them (e.g., DePaolo, 1981), were derived from a depleted, oceanic mantle source (Herzig, 1991). However, some significant modification of the magmas is indicated by observed low Ni concentrations and slightly

more evolved Nd and Sr isotopic values for the rhyolites. Such observations are suggestive of fractional crystallization of olivine and clinopyroxene, likely promoted by the hydrous character of the magmas (e.g., Nicholls and Ringwood, 1973), as well as the assimilation of some minor amounts of radiogenic crustal material. The most likely assimilant, at least near the level of extrusion, would have been continentally derived turbidite sequences, such as the Bedford Canyon Complex, which have an isotopic signature consistent with a continental provenance (Criscione et al., 1978). Assimilation, however, is not perceived to be significantly more than ~10% for even the most felsic units because of the relatively consistent concentrations of the incompatible elements (Herzig, 1991; Herzig and Wetmore, in progress).

One hundred and seventeen whole rock geochemical analyses of the Santiago Peak Volcanics define a wide range of lava types from basalts to rhyolites (Fig. 3.3). Major elemental determinations of lava type indicate that the Santiago Peak arc was most likely a continental margin arc rather than an island arc (e.g., Todd et al., 1988). For example, although the mean lava type is andesite, basalts are uncommon and rhyolites comprise ~25% of the samples analyzed. This is in direct contrast with the petrologic characterization of active island arc systems as being largely composed of basalts and basaltic andesites (Marsh, 1979). Furthermore, rhyolites comprise the basal unit to the Santiago Peak Volcanics in many studied localities (e.g., Santa Ana Mountains; Herzig, 1991). This precludes the possibility that Santiago Peak arc was long-lived and evolved into a felsic island arc.

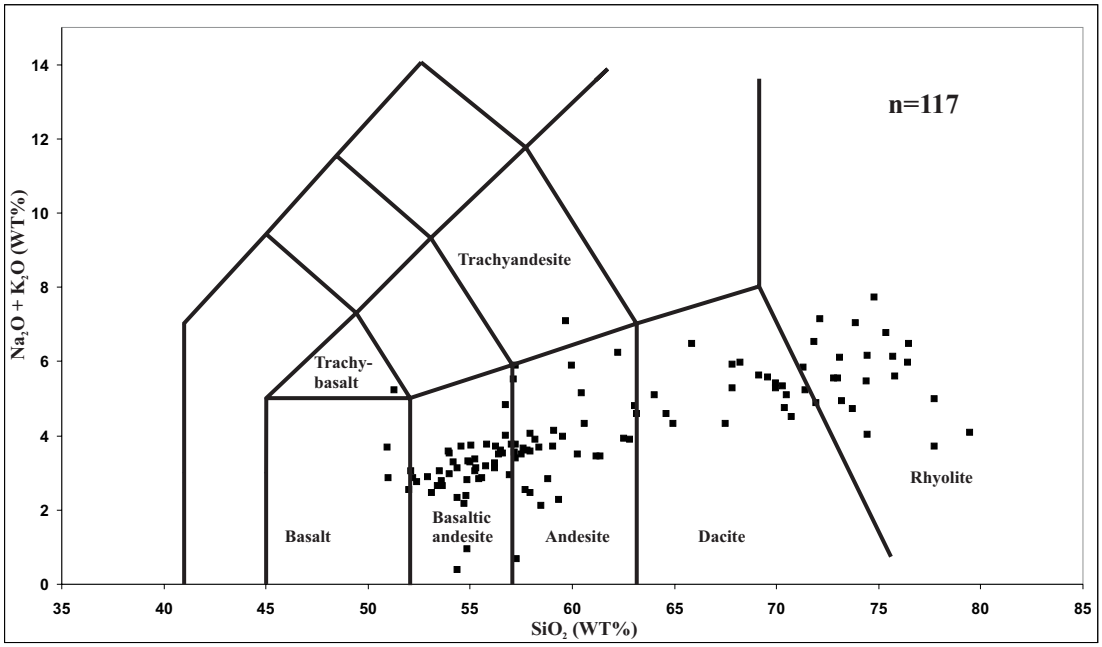

Figure 3.3. Chemical classification plot of lava types from the Santiago Peak Volcanic. Diagram of Le Maitre et al. (1989) Data compiled from Tanaka et al. (1984), Gorzolla (1988), and Herzig (1991).

Contact relations between the Santiago Peak Volcanics and the Bedford Canyon Complex. Contact relations between the Santiago Peak Volcanics and the underlying Bedford Canyon Formation in the Santa Ana Mountains are often not well exposed. This fact has lead to some erroneous interpretations that have been perpetuated in the literature through the years. Initial descriptions by Larsen (1948) as well as later descriptions by Schoellhamer et al. (1981) indicated a depositional contact between the two stratigraphic units. However, several subsequent studies concluded that the two were juxtaposed across a low angle fault (e.g., Peterson, 1967; Criscione et al., 1978). Many of the early tectonic models for the Mesozoic evolution of the Peninsular Ranges batholith were thus based on an accretionary juxtaposition of the Santiago Peak arc to the North American continent (e.g., Gastil et al., 1981; Todd et al., 1988). Such interpretations have persisted and can be found the most recent models (e.g., Dickinson and Lawton, 2001).

We have reexamined several key exposures of the contact between the Santiago Peak Volcanics and the Bedford Canyon Complex in the Santa Ana Mountains (Herzig, 1991; Sutherland, unpublished mapping), in central San Diego County (Wetmore and Herzig, unpublished mapping), and the Vallecitos area in Baja California (Sutherland and Wetmore, unpublished mapping). In each area several observations strongly suggest that this contact is an angular unconformity. At each exposure the moderately well-formed cleavage and folds, characteristic of the Bedford Canyon Complex strata, were oriented at high angles to, and truncated at, the contact (Fig. 3.4a-c). In Santa Ana Mountains and Vallecitos area an uncleaved conglomerate composed of chert and/or sandstone pebbles in a muddy matrix is locally preserved along the contact. Also in the Santa Ana

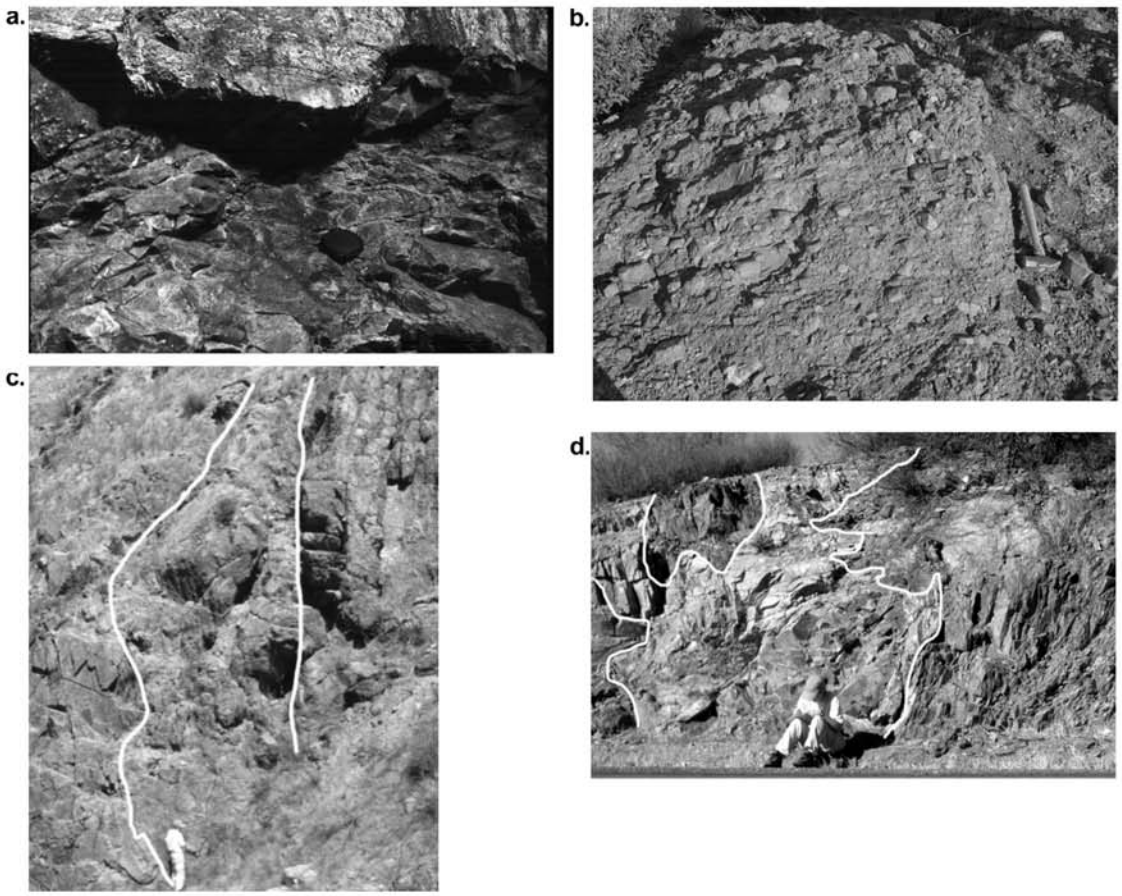

Figure 3.4. a) Contact between Bedford Canyon Formation and Santiago Peak Volcanics (top) in Santa Ana Mountains.; b) Basal conglomerate exposed along the contact between the Bedford Canyon Formation and Santiago Peak Volcanics in the Santa Ana Mountains.; c) Contact between Vallecitos Formation (left) and Santiago Peak Volcanics (right) with basal conglomerate preserved along the contact. Steep dip of contact is the result of rotation in the structural aureole of nearby pluton.; d) Hypabyssal intrusion of Santiago Peak Volcanics feeding overlying flows.

Mountains, the basal flows of the Santiago Peak Volcanics contain accidental sandstone and greywacke clasts from the underlying Bedford Canyon Formation. Additionally, Herzig (1991) reports that feeder dikes within the Bedford Canyon Formation may be traced directly into flows of the overlying Santiago Peak Volcanics (Fig. 3.4d).

Geochronology of the Santiago Peak Volcanics. Recent U/Pb geochronology studies of the Santiago Peak Volcanics by D. L. Kimbrough (San Diego State University) and his students (Anderson, 1991; Meeth, 1993; Carrasco et al., 1995) yield mildly discordant ages that range from 128 to 116 Ma. For example, a welded tuff that unconformably overlies the Bedford Canyon Formation in the Santa Ana Mountains and is inferred to be the basal unit of the Santiago Peak Volcanics, yielded an U/Pb zircon age of 127 ± 2 Ma (Anderson, 1991; Herzig, 1991). The 116 Ma age, derived from a sample 200 m below the mapped top of the Santiago Peak Volcanics section in the Cañon La Mision area (Fig. 3.1; Meeth, 1993), is assumed to be a minimum age for the end of Santiago Peak arc magmatism. Overlying the Santiago Peak Volcanics are course clastic forearc strata of Late Cretaceous age (e.g., Rosario Formation). Thus, the true termination of Santiago Peak volcanism is at some time between 116 Ma and the Late Cretaceous.

Observed discordance in the U/Pb zircon analyses of the Santiago Peak Volcanics and associated plutonics provide further evidence that the Santiago Peak arc was a continental margin arc and not an island arc. Anderson (1991) suggests that the observed discordances resulted from both minor lead loss and some inheritance of radiogenic lead. The possibility of inheritance is also supported by the presence of a small fraction of discolored zircons that did not appear to be consistent with the majority of clear, euhedral zircons. This observation suggests that these discolored crystals are xenocrysts derived

from minor amounts of incorporation of the country rock through which the plutons were emplaced (e.g., Bedford Canyon Complex). This is consistent with the observation that sandstone and greywacke xenoliths of apparent Bedford Canyon Formation are entrained within the basal flows and volcaniclastic units of the Santiago Peak (Herzig, 1991). These observed discordances and inferred inheritance occur in study areas for the entire length of the Santiago Peak arc segment including the San Diego area (Anderson, 1991), and the Cañon La Mision area south of the international border (Meeth, 1993).

Deformation of the Santiago Peak Volcanics. The deformational history of the Santiago Peak Volcanics is one of the most poorly constrained aspects of this part of the Peninsular Ranges. Our mapping in the Santa Ana Mountains, and central San Diego County has resulted in the identification of high angle brittle faults, and gentle to moderately steep tilting and open folding of the volcanics. However, the observed cleavage and ductile strain that characterizes the underlying Bedford Canyon Complex is not observed within the Santiago Peak Volcanics. In fact, fabric ellipsoids determined from lithic-rich samples from the Santiago Peak Volcanics do not significantly deviate from those measured in undeformed volcanics (Sutherland et al., 2002).

Mapping of the Santiago Peak Volcanics near Rancho Vallecitos (Sutherland et al., 2002) and north of the active Agua Blanca fault (Fig. 3.1 and 3.5B) has resulted in the identification of pronounced tilting and ductile strain, including a pervasive and well-developed cleavage, within the structural aureoles of plutons in both these areas. However, away from these intrusive bodies the minor deformation observed affecting the volcanics is similar to that characterizing exposures north the international boarder.

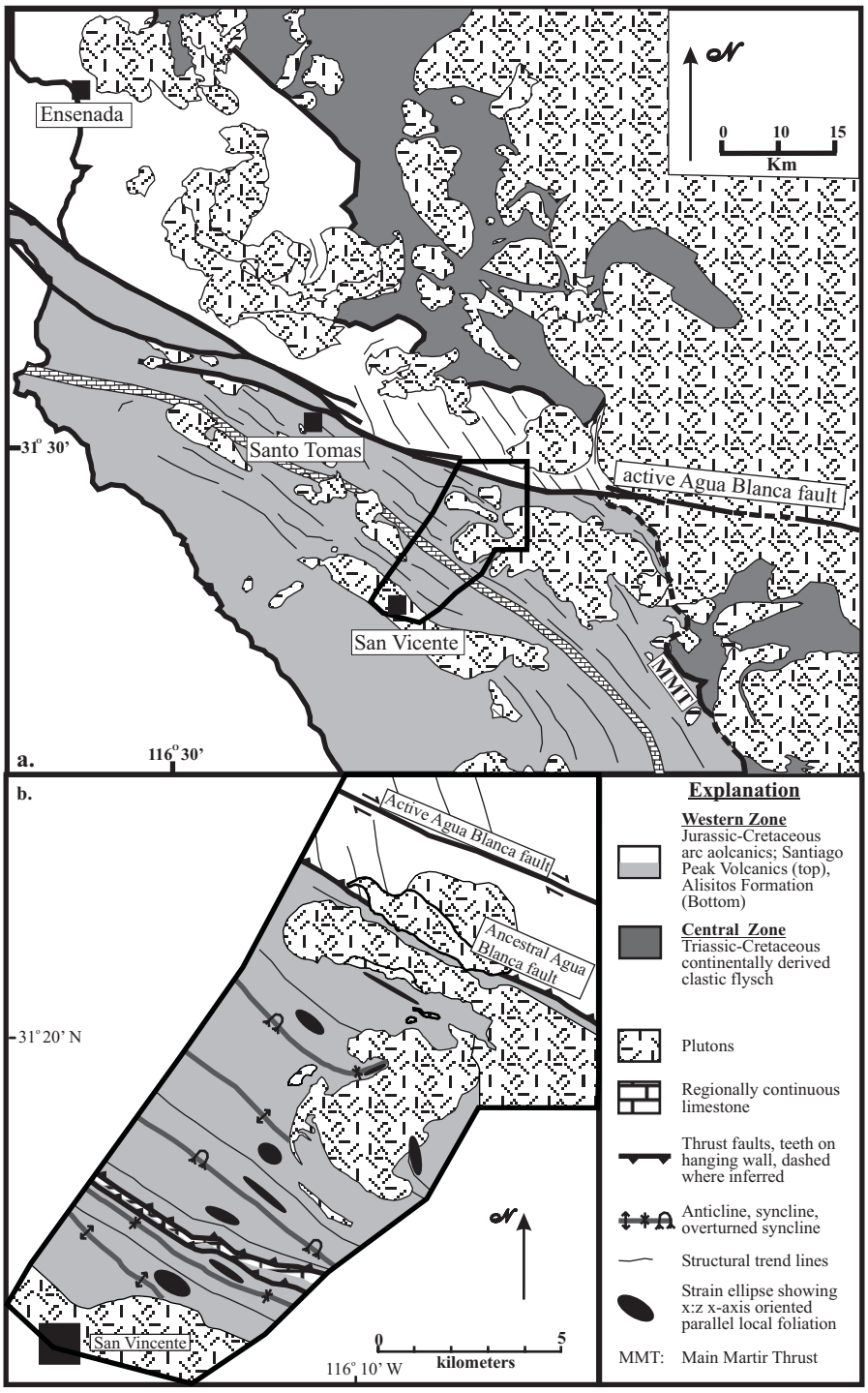

Figure 3.5. a) Geologic map of the Agua Blanca Fault based on Gastil et al. (1975); b) Map of the northern Alisitos arc northeast of San Vicente (mapping by Wetmore).

In the area of the Agua Blanca fault the Santiago Peak Volcanics are cut discordantly by both the northwest trending active strike slip structure, and an older dip slip fault. The structural trends defined by the axes of open folds, minor west-vergent faults, and the average strike of bedding are truncated at the southern extent of the Santiago Peak Volcanics by what has been mapped as the ancestral Agua Blanca fault (Fig. 3.5) (Wetmore et al., 2002). This steeply northeast-dipping shear zone parallels the active Agua Blanca fault, but is located ~2 km to the south. While some deflection (drag) of these regional trends are observed with proximity to the active structure, no deflection has been observed associated with the older ancestral Agua Blanca fault. Furthermore, no increase in finite ductile strain, or increases in metamorphic grade are observed with proximity to the latter structure.

The above description of the Santiago Peak Volcanics and associated intrusives indicate that the Santiago Peak arc north of the Agua Blanca fault developed atop the Late Triassic through Jurassic Bedford Canyon Complex. Initiation of Early Cretaceous arc magmatism began after the earlier-formed strata were deformed, uplifted, and erosionally beveled as indicated by the truncation of fabrics and structures within the Bedford Canyon Complex at the contact with the overlying volcanics. Evidence supporting a depositional contact between the volcanics and the Bedford Canyon Complex strata, include a basal conglomerate present along the contact, xenoliths and xenocrysts of Bedford Canyon Complex derivation in the Santiago Peak Volcanics, a pronounced break in deformation across the contact without any indication of shear, and

hypabyssal intrusions that cross-cut the turbidites and the contact to feed the overlying volcanics.

Peninsular Ranges South of the Agua Blanca Fault

South of the Agua Blanca fault there have been considerably fewer geologic investigations of the western and central zones of the Peninsular Ranges. However, those that have been completed describe a Late Triassic through Early Cretaceous history that is markedly different from that to the north of the Agua Blanca fault. The most salient differences south of the ancestral Agua Blanca fault are the lack a Late Triassic through Jurassic accretionary prism (cf., Bedford Canyon Complex) to the south, and that the western and central zones are juxtaposed across a well-defined east dipping ductile shear zone (Main Mártir thrust). Below we describe the central and western zones in this region (Fig. 3.1).

Central Zone

Sierra San Pedro Mártir. The central zone in the Sierra San Pedro Mártir area (Fig. 3.1) has been the focus of two recent structural studies, Johnson et al. (1999a) in the northern part, and Schmidt (2000) in the southern. In each area the thermal affect of the numerous plutonic bodies has metamorphosed most of the preserved country rock screens to at least amphibolite grade. As such, the age and depositional environments of these prebatholithic strata cannot be constrained unequivocally. However, along the western-most exposures of the central zone in both the northern and southern Sierra San Pedro

Mártir the strata are comprised of calc-silicates, metavolcanics and quartzo-feldspathic metapelites.

Plutons that intrude these strata range in age from ~134 Ma to ~97 Ma (Johnson et al., 1999a; Schmidt, 2000) with two major pulses, one between 134 and ~128 Ma and the other associated with the Late Cretaceous La Posta event between 100 and 94 Ma (e.g., Walawender et al., 1990). Thus, the age of the host stratigraphy must be greater than ~134 Ma. Correlation of these strata with the Paleozoic through Early Triassic continental slope basin deposits exposed elsewhere in the central zone south of the Agua Blanca fault is possible but the presence of a volcanic component is inconsistent with lithologies described for the older strata. We therefore, suggest that the strata exposed in the westernmost exposures of the Sierra San Pedro Mártir were most likely deposited during the Middle to Late Jurassic when arc magmatism is known to have been active in eastern parts of the central zone (Schmidt, 2000) and further east in mainland Mexico (e.g., Damon et al., 1983).

Two deformational events are recorded within the prebatholithic strata of the central zone in the Sierra San Pedro Mártir (Schmidt, 2000). The oldest event predates the ~134 Ma plutons as host rocks in the middle part of the central zone possess a foliation which is not preserved in the intrusives of the earlier pulse of magmatism. In the western part of the central zone this earlier fabric is strongly overprinted by mylonitic fabrics associated with the Main Mártir thrust (discussed below), the west directed shear zone that juxtaposes the central and western zones (Johnson et al., 1999a). Deformation associated with this structure may have initiated as early as ~132 Ma as indicated by igneous sheets

and high temperature subsolidus fabrics in plutons of this age along the western margin of the central zone (Schmidt, 2000).

El Marmol Area. The El Marmol area is located ~80 km south-southeast of the southern Sierra San Pedro Mártir (Fig. 3.1). Paleozoic to Early Triassic continental slope basin deposits that overlapped older North American miogeoclinal assemblages (Buch and Delattre, 1993; Campbell and Crocker, 1993; Gastil, 1993) are exposed in this part of the central zone. The slope basin stratigraphy is comprised of thin-bedded argillite, sandstones, and cherts with interbedded calcareous quartzarenite and pebble conglomerates with clast compositions of chert and quartzite. These strata are interpreted to have been deposited by sediment gravity flows with intervening intervals of quiescent pelagic sedimentation (Buch and Delattre, 1993).

Paleozoic to Early Triassic strata are overlain with angular discordance by the Early Cretaceous Olvidada Formation in the El Marmol area (Fig. 3.6; Phillips, 1993). Phillips (1993) describes lower, middle, and upper members of this formation. The lower member is composed of boulder-pebble conglomerate and sandstone, some containing volcanogenic detritus and minor limestones clasts. Phillips (1993) interprets this member to represent shallow marine deposition. The gradationally overlying middle member is composed of rhythmically bedded cherts, sandstones, and shales and is interpreted to represent deep-water slope basin to abyssal plain deposition. These marine strata are unconformably overlain by the upper member of the formation that consists of cobble conglomerate containing clasts that appear to be derived from the middle member of the formation, and sandstones and shales. The section is capped by vesicular andesites interpreted to have been deposited in a subaerial environment.

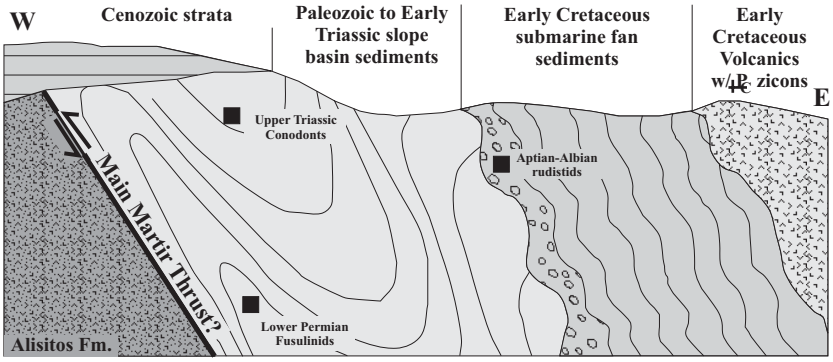

Figure 3.6. Schematic cross section through the El Marmol area. Based on mapping and descriptions from Buch and Delattre (1993) and Phillips (1993).

Deformation of the Paleozoic through Early Cretaceous strata of the El Marmol area includes an overall east tilting of the entire section as well as two generations of folding (Buch and Delattre, 1993). The first generation of folding appears to affect only the Paleozoic to Early Triassic strata and is characterized by tight to isoclinal folds with northwest-striking, northeast-dipping axial planes. The second generation of folding affects both pre-Cretaceous and Early Cretaceous strata but not Late Cretaceous dikes and sills. Similar to the earlier-formed folds, the second generation of folds are tight to isoclinal but with axial surfaces that strike more westerly than those of the former generation. Tertiary and Quaternary volcanic and sedimentary deposits obscure contact relationships between the strata of the El Marmol area and that of the western zone volcanics.

Sierra Calamajue. The Sierra Calamajue is located ~80 km south-southeast of the El Marmol area. Mapping in this area was completed by Griffith and Hoobs (1993) and is being remapped as part of a regional transect by H. Alsleben (unpublished mapping). The stratigraphy of the Sierra Calamajue is dominated by metavolcanics and volcaniclastics with subordinate amounts of carbonate, phyllite, chert, and limestone pebble to cobble conglomerate. According to Griffith and Hoobs (1993) the strata in the Sierra Calamajue range from Mississippian through the Early Cretaceous. However, D.L. Kimbrough is presently reevaluating many of the U/Pb age determinations for the volcanic stratigraphy in this part of the central zone. An early observation from this work indicates that the analyzed units from this area are that all of the volcanics are Early Cretaceous and contain some component of inherited Precambrian zircons.

Perhaps similar to the El Marmol section, the westernmost exposures in the Sierra Calamajue are comprised of Paleozoic(?) deep marine strata, represented here by the Cañon Calamajue unit (Griffith and Hoobs, 1993). Lower parts of the Cañon Calamajue unit are composed of cherts and phyllites. Near the top of the unit is a limestone cobble conglomerate with a volcaniclastic matrix. The blocks of this conglomerate yield Chesterian age conodonts of North American affinity. However, the allochthonous nature of these blocks suggests that this is a lower age limit and not necessarily the age of deposition for the Cañon Calamajue unit.

Northeast of the Cañon Calamajue unit are a series of metavolcanic units with interbedded limestones juxtaposed with phyllite-dominated units, with lesser volcanics, across northeast dipping, southwest vergent thrust faults (Griffith and Hoobs, 1993). Deformation of these units reaches a maximum intensity within Cañon Calamajue, an observation that lead Griffith and Hoobs (1993) to suggest that this zone was the suture between North America and the Alisitos arc of the western zone. However, due to the presence of strata with North American provenance and volcanics containing Precambrian zircons west of the faults, alternative interpretations are possible (see Discussion section).

In summary, the along strike lithologic character of the central zone south of the ancestral Agua Blanca fault does exhibit several differences from place to place but, as a whole it appears to have experienced a broadly similar evolution throughout along its length. For example, while the ratio of volcanics to marine sediments is not the same for any of the two areas, the observation of marine deposition of clastic sediments succeeded by the subaqueous deposition of volcanics is common to all three. This indicates the

presence of a basin or basins along the southwestern margin during the latest Jurassic through much of the Early Cretaceous. However, missing from each of these areas are the Late Triassic through Jurassic turbidite sequences that dominate the central zone of the Peninsular Ranges north of the ancestral Agua Blanca fault.

Western Zone

Early Cretaceous arc strata of the western zone of the Peninsular Ranges batholith south of the Agua Blanca fault are included in the Alisitos Formation. Most early studies of the Alisitos Formation focused on stratigraphy, paleontology, and depositional environment (e.g., Allison, 1955, 1974; Silver et al., 1963; Suarez-Vidal, 1986) with many of these studies confined to northernmost exposures. Recent studies have expanded the understanding of the stratigraphy to more southern areas (e.g., Beggs, 1984; Fackler-Adams, 1997), and have begun to focus on the structural/tectonic and magmatic evolution of this part of the Peninsular Ranges (e.g., Goetz, 1989; Johnson et al, 1999a,b; Tate and Johnson, 2000; Tate et al., 1999; Schmidt, 2000; Wetmore et al., 2002).

Alisitos Formation. The Alisitos Formation is composed of reworked or epiclastic volcaniclastics, volcanogenic argillites and sandstones, several primary volcanic flows and breccias, and a regionally extensive prominent limestone/marble member that can be traced continuously from Punta China to the northern Sierra San Pedro Mártir (Silver et al., 1963; Fig. 3.1 and 3.5). Subaqueous deposition dominated during the emplacement of the Alisitos Formation based on the observed volcaniclastic lithologies and the abundant fossils preserved within them, and the presence of several basaltic lava flows exhibiting pillow structures (Leedom, 1967; Reed, 1967; Allison, 1974; Beggs, 1984;

Suarez Vidal, 1986, 1993; Fackler-Adams, 1997). Subaerial deposition occurs locally near inferred volcanic edifices (Fackler-Adams, 1997).

Petrologic classifications of the volcanics of the Alisitos Formation lack the support of the large geochemical data set in existence for the Santiago Peak Volcanics. However, descriptions from hand samples and thin sections suggest that the two share a similar range in composition (e.g., Fackler-Adams, 1997). However, based on the few published stratigraphic columns (e.g., Leedom, 1967, Allison, 1974), combined with our own mapping near San Vicente (Wetmore, unpublished mapping; Fig. 3.1) and in the western part of the Sierra San Pedro Mártir (Schmidt, 2000) we believe that basalts, basaltic andesites, and andesites overwhelmingly dominate and that more siliceous volcanics (e.g., rhyolites) are uncommon.

The presence of moderate to deep water, clastic and biochemical sediments in the Alisitos Formation is reported by Suarez-Vidal (1986; 1993) and Johnson et al. (1999a). Suarez-Vidal (1993) suggested that the package of clastic sediments that he mapped in an area south of the Agua Blanca fault and near El Arco (Fig. 3.1), represented a regionally continuous depositional package that comprised the northern and eastern exposures of the Alisitos Formation. In the northern Sierra San Pedro Mártir, Johnson et al. (1999a) mapped a north-northwest trending belt of equivalent rocks bounded on the west and east by west-vergent thrust faults. Suarez-Vidal (1993) further suggested that the presence of such rocks indicated deposition in a "tectonically quiet" setting, such as a back-arc environment.

Paleontological investigations of the Alisitos Formation have consistently yielded Early Cretaceous fauna (e.g., Allison, 1955, 1974; Silver et al., 1963). Some early

confusion may have existed concerning the exact age (Aptian-Albian) of some of the fossils, but ultimately an age of Albian was determined by Allison (1974). Subsequently, a small number of U/Pb zircon ages have been reported for both the volcanics, as well as for some of the plutons that intrude the Alisitos Formation. Carrasco et al. (1995) and Johnson et al. (in press) report ages from the volcanics of 116 $\pm$ 2 and 115 $\pm$ 1.1 Ma. Johnson et al. (1999a) further report ages from plutons of the western part of the Sierra San Pedro Mártir area that range from 116.2 $\pm$ 0.9 to 102.5 $\pm$ 1.6 Ma. None of these U/Pb zircon studies have resulted in the observation of any component of Precambrian inheritance.

The most complete geochemical data sets for the Alisitos arc segment are from the Zarza Intrusive Complex and the San José tonalite of the northern Sierra San Pedro Mártir area reported in Tate et al. (1999) and Johnson et al. (in press; Fig. 3.1). Similar to data from the Santiago Peak Volcanics, these intrusive bodies yield major and trace element, and isotopic signatures that are consistent with melt derivation from within depleted oceanic lithosphere. However, unlike the Santiago Peak Volcanics, interpreted contamination is consistent with assimilation of metabasite (Tate et al., 1999) rather than more silicic continentally derived clastic sedimentary sequences. Combined with the observed lack of any inherited component to the zircons from either intrusive or extrusive igneous rocks, these observations strongly suggest that the basement of the Alisitos arc segment does not contain continentally derived materials (Johnson et al., 1999a, Wetmore et al, 2002).

Structures attending the boundaries of the Alisitos arc. Contact relationships between the Alisitos Formation and the continentally derived clastic sedimentary sequences of the

central zone have been described in both the northern and southern Sierra San Pedro Mártir (Goetz, 1989; Johnson et al., 1999a; Schmidt, 2000). In each of these areas the two lithostratigraphic belts are juxtaposed across a large, east over west, ductile shear zone known as the Main Mártir thrust. A similar structural juxtaposition exists between the Alisitos Formation and the Santiago Peak Volcanics to the north across a newly identified southwest-vergent reverse fault (Wetmore et al., 2002). To the south of the Sierra San Pedro Mártir the presence of structures clearly juxtaposing the Alisitos Formation with central zone deep water sediments and successive volcanics have not, as yet, been clearly identified.

Studies of deformation within the Alisitos Formation have traditionally focused on structures developed along the eastern margin of this part of the western zone (Goetz, 1989; Johnson et al., 1999a; Schmidt, 2000). Strong deformation characterizes each of these areas where west-vergent ductile shear zones place the continentally derived clastic sedimentary sequences over the Alisitos Formation (Fig. 3.1 and 5). Our reconnaissance work across the Alisitos indicates that the intensity of deformation increases from shallowly west dipping strata without observed internal fabrics in western exposures, to openly folded strata with horizontal axes, moderate-well formed cleavages, and intermediate strain intensities (<~40% shortening in the z-direction), and finally to isoclinally folded strata with inclined axes, strongly developed foliations, and large strain intensities (>~60% shortening) adjacent to the Main Mártir thrust. The overall across strike width of this fold and thrust belt is ~25 km (Johnson et al., 1999a; Wetmore et al., 2002). The Main Mártir thrust also corresponds to the transition between intrusives to the west that exhibit no observed inherited older zircons, and yield primitive isotopic

signatures, from those to the east that do possess Precambrian zircons and evolved isotopic signatures (Johnson et al., 1999a). Johnson et al. (1999a) constrain the timing of the main pulse of deformation within this fold and thrust belt and across the Main Mártir thrust to be between ~115 and 108 Ma.

In the northern part of the arc segment the fold and thrust belt that includes the Main Mártir thrust is deflected into sub-parallelism with the trace of the ancestral Agua Blanca fault (Wetmore et al., 2002). This deflection involves as much as 50° of strike rotation in a counterclockwise sense (i.e. from ~N15°W to N65°W; Fig. 3.5). Our recent mapping in the area south of the fault (Fig. 3.5) has resulted in the identification of a pronounced break in strain intensity across a northeast dipping ancestral Agua Blanca fault. Overall deformation increases dramatically with proximity to the ancestral Agua Blanca fault with folds becoming isoclinal and strain intensities becoming immeasurably large. Shear sense determined from lineation-parallel sections within the underlying Alisitos Formation suggest a strong component of northeast side up motion across the fault which is also consistent with the southwest vergence of all folds developed in this region. However, additional kinematic information was obtained from sections perpendicular to the lineation suggesting an additional component of sinistral shear, opposite current motion across the nearby active brittle fault.

In summary, the western zone of the Peninsular Ranges south of the ancestral Agua Blanca fault is composed of plutons that intrude the Albian Alisitos Formation, which is characterized by subaqueous volcanic deposits (dominantly basalts and andesites), reworked epiclastic volcanic sediments, and subordinate amounts of carbonate. Geochemical and geochronological studies of the volcanics and plutonics suggest

derivation from a depleted mantle source without contamination from continental crust or continentally derived deposits. The northern and eastern boundaries of the Alisitos arc are characterized by broad (>20 km) southwest-vergent fold and thrust belts with the Main Mártir thrust and the ancestral Agua Blanca fault juxtaposing the Alisitos arc with the central zone and Santiago Peak Volcanics, respectively.

Discussion

The above descriptions of the western and central zones of the Peninsular Ranges batholith clearly illustrate the dramatic differences north and south of the ancestral Agua Blanca fault. These differences include the following (Table 3.1): (1) the presence or absence of Late Triassic through Jurassic continentally-derived turbidite sequences (north) and/or Early Cretaceous submarine sedimentary strata (south), (2) the environment of deposition of Early Cretaceous western zone volcanics, and contact relations between these volcanics and the continentally-derived strata of the central zone (depositional, north; fault, south), (3) presence of xenocrystic Precambrian zircons in plutons and volcanic flows of the western zone (present, north; absent, south), (4) the frequency of lava types of western zone volcanics (abundant rhyolites, north; abundant basalts, south), (5) the general distribution and intensity of deformation within the western zone (minor to moderate, north; 20 km wide fold and thrust belt, south), and (6) the character of deformation associated with the ancestral Agua Blanca fault (truncation, north; deflection into subparallelism, south). We believe that these differences unambiguously indicate that the ancestral Agua Blanca fault is the along-strike continuation of the Main Mártir thrust as together they served as a nonterminal suture

accommodating the juxtaposition of the Alisitos arc segment to the Santiago Peak arc segment and North America. Additionally, the ancestral Agua Blanca fault must have been an accommodating structure to the tectonic removal of the pre-Cretaceous accretionary prism, represented by the Bedford Canyon Complex to the north, prior to Alisitos arc accretion.

An Alternative Tectonic Model

During the Late Triassic through at least the Jurassic the southwestern margin of North America north of the ancestral Agua Blanca fault was the site of a considerable amount of turbidite sedimentation. These deposits, which contain Precambrian zircons and olistostromal blocks of miogeoclinal quartzite, clearly exhibit a North American provenance. The presence of an arc to the east (Damon et al., 1983; Saleeby et al, 1992), active contemporaneously with turbidite sedimentation combined with observed serpentinite blocks, olistostromes included within the section suggest that the deformation exhibited by these sequences likely resulted during incorporation into an accretionary prism (Fig. 3.7a and 7b (line A-A')). Additionally, the westward younging of east-dipping Bedford Canyon Complex strata is consistent with the imbrication of coherent (albeit internally deformed) packages of stratified sediments forming duplexes in an accretionary wedge associated with a west facing arc (e.g., Lash, 1985; Sample and Fisher, 1986; Sample and Moore, 1987).

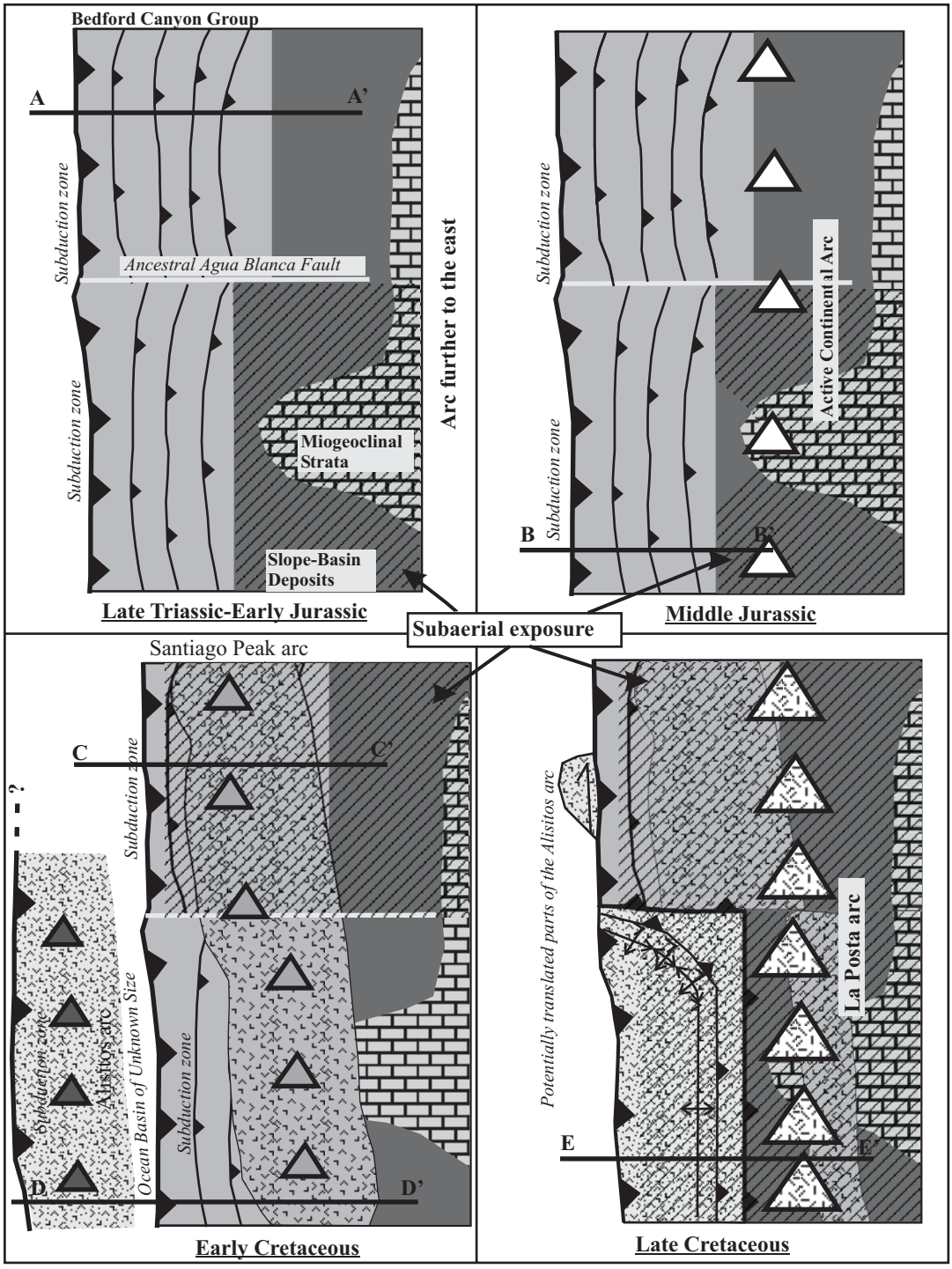

Figure 3.7. a) Schematic depiction of the Late Triassic through Early Cretaceous tectonic evolution of the Peninsular Ranges batholith. b) Cross sections (lines A-A' and C-C') through the Peninsular Ranges batholith north of the ancestral Agua Blanca fault. c) Cross sections (lines B-B', D-D', and E-E') through the Peninsular Ranges batholith south of the ancestral Agua Blanca fault.

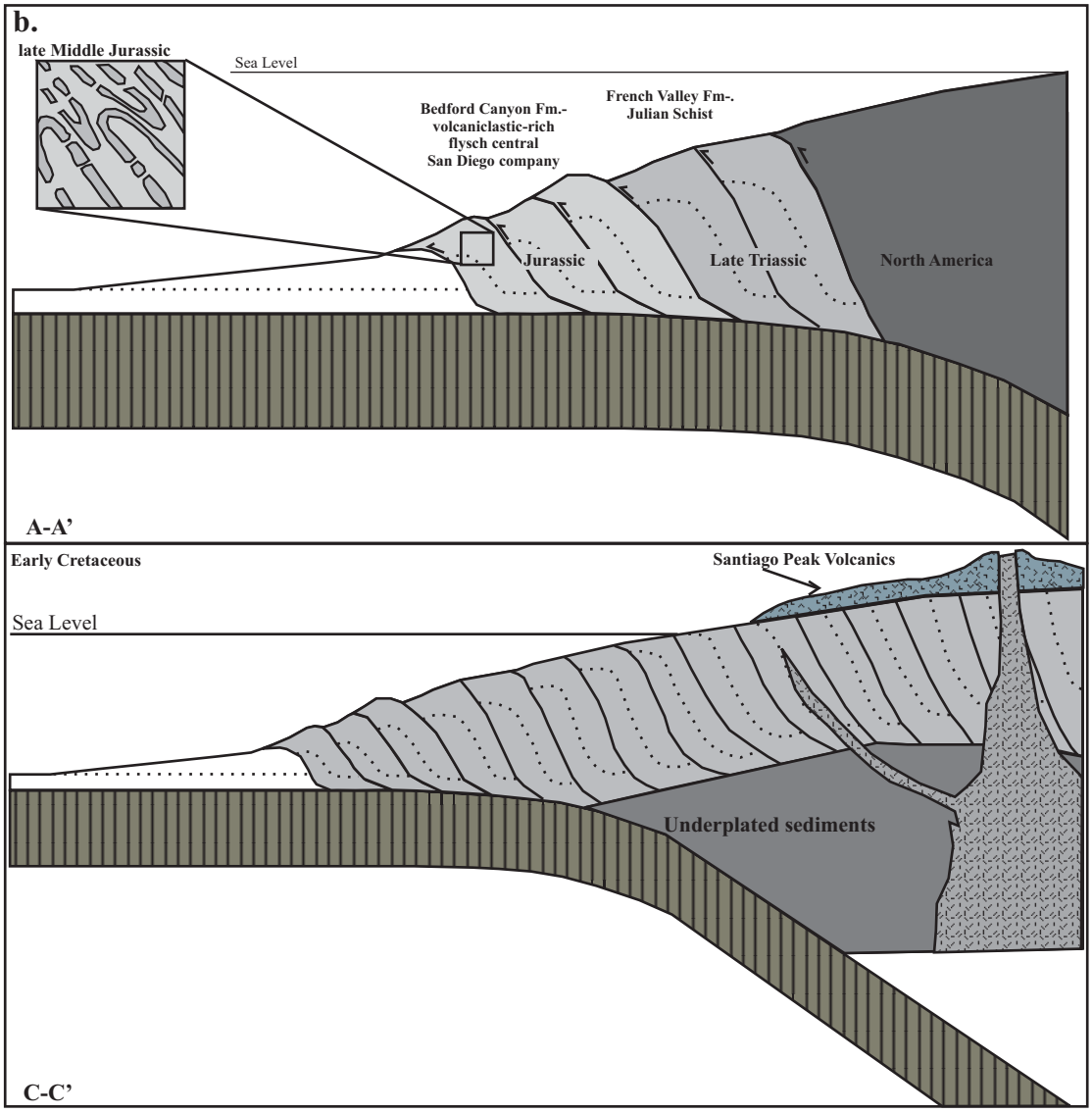

Figure 3.7: Continued

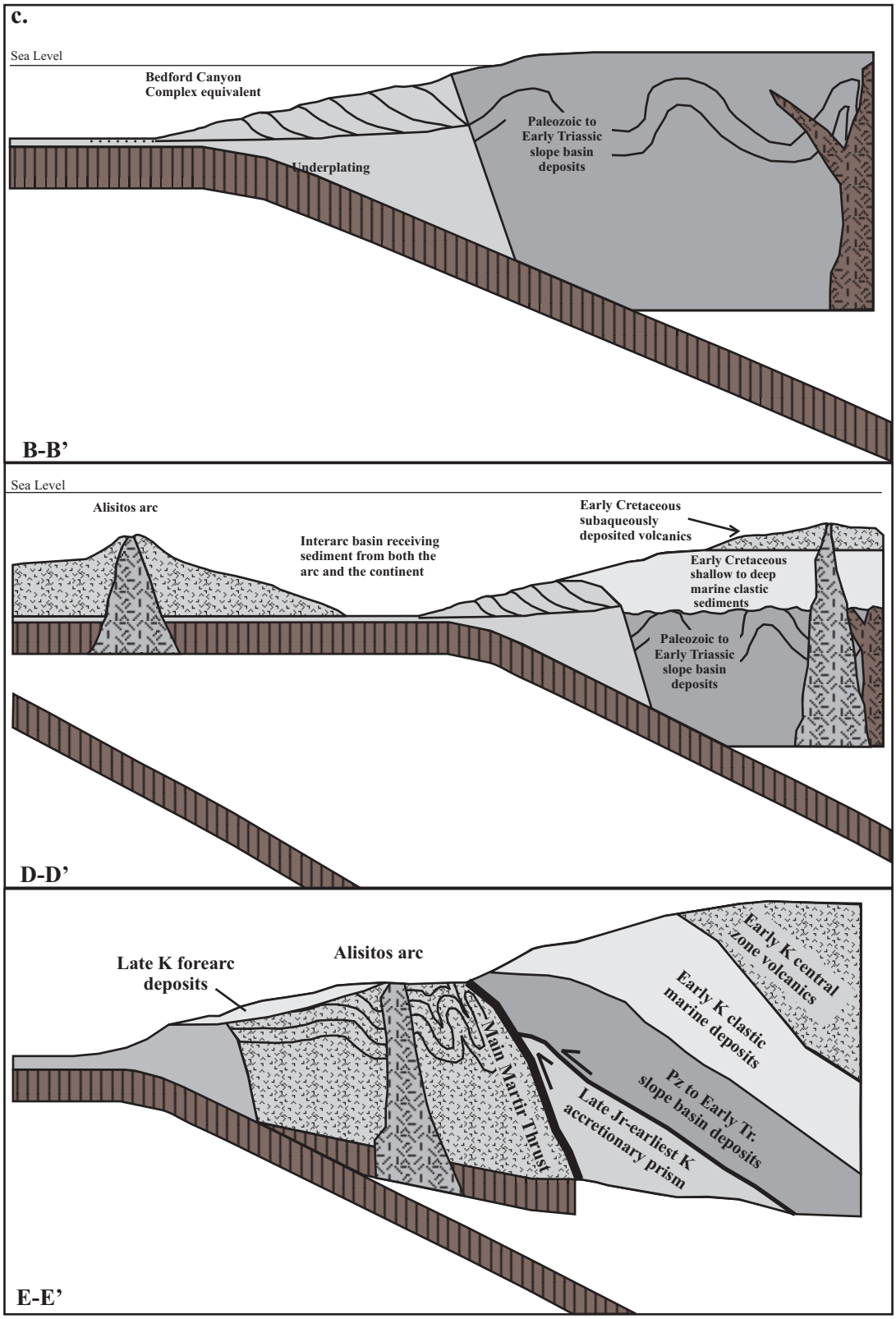

Figure 3.7: Continued

Following deposition of the Bedford Canyon Complex and deformation within an accretionary prism setting, the entire section appears to have been uplifted, subaerially exposed and erosionally beveled (Fig. 3.7a and 7b (line C-C')). This is consistent with the interpretation that the Santiago Peak Volcanics were deposited in a subaerial environment. A specific uplift event is not necessary to expose these strata to subarial erosion. Rather, the strata of the Bedford Canyon Complex could have simply moved toward higher elevations as a function of time and the addition of material into the wedge, both scrapped off at the toe, as the Bedford Canyon Complex appears to have been, and underplated in a manner similar to the process proposed for the uplift and exhumation of the Cascadia accretionary wedge in Washington state (Brandon et al., 1998).

In addition to uplift of strata within the accretionary prism, a further result of long-term accretion of material to the southwestern margin of North American may have been the apparent westward migration of magmatism that impinged upon the Late Triassic to Jurassic accretionary prism in the Early Cretaceous (Fig. 3.7a). However, other options could include a steepening of the subducting slab or the initiation of a new subduction zone outboard of an older one.

Table 3.1. Variations in the Peninsular Ranges batholith north and south of the Agua Blanca fault.

	North of Agua Blanca fault	South of Agua Blanca fault
Late Triassic-Jurassic clastic turbidites	Yes	No
Early Cretaceous clastic sediments	No	Yes
Depositional environment of Cretaceous arc volcanics	Subarial	Submarine
Contact relations between Early Cretaceous volcanics and continentally-derived sediments of the central zone	Depositional unconformity	Large ductile southwest-vergent shear zone
Inherited zircons	Observed within both volcanics and plutonics	Not observed in either volcanics or plutonics
Lava types	Andesites most abundant, but with ~40% comprised of dacites and rhyolites	Dominated by basalts, basaltic andesites, and andesites, dacites and rhyolites rare
Regional deformation	Weak to moderate, somewhat elevated in southeastern exposures	Intense within fold and thrust belt along eastern and northern limits to the Alisitos arc
Deformation associated with Agua Blanca fault	Truncation of regional structures without increases in strain or metamorphism	Regional change in structural trend, high strain intensities and amphibolite? grade metamorphism

Regardless of the mechanism that caused the apparent migration, by the Early Cretaceous the Santiago Peak arc was being built on and through the southwestern margin of the North American continent. This interpretation is supported by observed depositional contacts between the volcanics and the continentally derived stratigraphy, xenocrysts Precambrian of zircon in both the volcanics and plutonics, xenoliths of sandstone and greywacke in the volcanic flows, and the presence of intrusions that cut the Bedford Canyon Complex and can be traced directly into the overlying flows of the Santiago Peak Volcanics. Furthermore, while the overall chemistry of the intrusive and extrusive magmas of the Santiago Peak arc are clearly derived from a depleted mantle

source, the volcanics have been altered by moderate amounts of assimilation of silicic material and fluid enhanced fractional crystallization, such that the overall distribution of lava types is strongly skewed away from the typical island arc assemblage and toward more silicic dacites and rhyolites.

Deformation within the Santiago Peak Volcanics is somewhat enigmatic in that the regional deformation is typically very minor (upright, open folds and minor offset (< 50m), high angle brittle faults). While part of this deformation may have been Early Cretaceous in age some proportion of it must be Late Cretaceous or younger given the steeply west dipping paraconformity(?) between the Santiago Peak Volcanics and the overlying Late Cretaceous clastic strata western Santa Ana Mountains.

South of the ancestral Agua Blanca fault the fact that Late Triassic through Jurassic sedimentary strata have been preserved only locally (i.e., Sierra San Pedro Mártir) suggests that this part of the Peninsular Ranges was largely emergent during this time (Fig. 3.7a and 7c (line B-B')). However, given that a continental arc did exist in Sonora, Mexico (Ramon et al., 1983) during this time, the trench and accretionary prism represented by the Bedford Canyon Complex to the north of the ancestral Agua Blanca fault should have existed west of the present location of the central zone south of the fault. This is also consistent with the presence of earliest Cretaceous plutonics in the hanging wall of the Main Mártir thrust (Johnson et al., 1999a).

During the Early Cretaceous the central zone of the Peninsular Ranges batholith south of the Agua Blanca fault subsided below sea level and began receiving clastic detritus from the east (Fig. 3.7a and 7c (line D-D')). This appears to have been a relatively short-lived condition as later in the Early Cretaceous this basin was filled or uplifted as clastic

sedimentation gave way to the deposition of proximally derived volcanics that grade upward from submarine into subaerial deposits. The transition between clastic and volcanic deposits was contemporaneous with the deformation of the clastic strata prior to the deposition of the volcanics. This suggests that termination of the latest Jurassic-Early Cretaceous central zone basin may have, in part, resulted from tectonic closure. Like the Santiago Peak Volcanics, the volcanics of the central zone bear the signature of contamination by continentally derived materials implying derivation from sources within the central zone or from further east.

The volcanics/volcaniclastics of the Alisitos arc south of the Agua Blanca fault were deposited in a submarine environment and are believed to be everywhere in fault juxtaposition with continentally-derived strata, including the Santiago Peak Volcanics (Fig. 3.7a). In fact, volcanic strata of the Alisitos arc exhibit no indication that rocks of continental derivation exist in the basement of this arc, such as the presence of xenocrystic Precambrian zircons in volcanics or plutonics, or evolved magmas which can be shown to have otherwise assimilated clastic detrital material (e.g., Bedford Canyon Complex). Such observations led Johnson et al. (1999a) to argue that the Alisitos arc originated as an island arc developed on oceanic crust not previously associated with North America. This interpretation is also consistent with the prominence of basalts and andesites as the dominant petrologic types for volcanics of the Alisitos Formation.

The deformation within the Alisitos arc is much more widespread and, along its eastern margin, of greater intensity than that observed within the Santiago Peak arc to the north. Deformation associated with the southwest-vergent fold and thrust belt that parallels the Main Mártir thrust, the structure juxtaposing the Alisitos arc with North

America-derived strata, suggests a causal link between the two. Goetz (1989), Johnson et al. (1999a), and Schmidt (2000) all concluded that this belt of deformation reflects the accretion of the western arc to the continental margin in the Early Cretaceous (Fig. 3.7a and 7c (line E-E')). In all of these models the accretion occurs across an east dipping subduction zone along the western continental margin. This is consistent with the southwest-vergence of all identified structures associated with the Main Mártir thrust (Johnson et al., 1999a; Wetmore et al., 2002).

The fold and thrust belt along the ancestral Agua Blanca fault represents a unique feature within the Peninsular Ranges and is best explained by tectonic juxtaposition of the two western zone arc segments. The counterclockwise rotation of structures within the Alisitos arc into subparallelism with the ancestral Agua Blanca fault in the northern part of the arc, along with observed kinematics in this area suggest that the northern Alisitos was strongly affected by sinistral transpression, opposite to displacements along the active fault. The continuation of southwest vergent thrusting from the Main Mártir thrust to the ancestral Agua Blanca fault suggests that the latter represents the northward continuation of the former. Therefore, the ancestral Agua Blanca fault is interpreted to be the suture zone which juxtaposes the two arc segments of the western zone (e.g., Wetmore et al., 2002).

Additional Tectonic Considerations

The above tectonic history brings several additional tectonic problems into focus. Deformations observed in eastern San Diego County associated with the Cuyamaca Laguna Mountain Shear Zone (CLMSZ) and that of the faults in Cañon Sierra Calamajue

have been interpreted as sutures juxtaposing western and central zones. However, these interpretations are not reconcilable with the above models and thus, further discussion is necessary. Additionally, the above tectonic model implies that components of the central zone observed north of the ancestral Agua Blanca fault must have been tectonically removed to the south of the fault and that the Late Cretaceous exhumation observed in the central zone along the length of the Peninsular Ranges cannot everywhere be attributed to accretion-related deformation.

Deformation in the Sierra Calamajue was interpreted by Griffith and Hoobs (1993) as resulting from the accretion of the Alisitos arc to the North American margin. However, as noted above, volcanics containing inherited Precambrian zircons and limestone conglomerates yielding North American affinity fossils are observed west of the faults mapped in Cañon Calamajue. These observations are inconsistent with those from the Alisitos Formation in other areas of the Peninsular Ranges. Two alternative explanations for this apparent inconsistency are: (1) these faults do not form the suture, rather the suture likely exists further to the west of the Sierra Calamajue; and (2) continentally-derived sediments and volcanics dominated the Early Cretaceous basin that existed between the continent and the Alisitos arc such that these strata were deposited across the intervening trench and onto the Alisitos island arc. The existence of the suture at a more westerly position than the Cañon Calamajue is certainly possible give the overall lack of mapping in this area combined with the large areas to the west of the Sierra Calamajue covered by Tertiary and Quaternary strata. The latter alternative is likewise possible given that the Alisitos arc was largely submerged throughout its depositional history and as the arc got progressively close to North American the basin between the two

continually shrank. However, more detailed study of this part of the Peninsular Ranges is required before these or other potential alternatives can be distinguished.

The Cuyamaca Laguna Mountain Shear Zone (CLMSZ) is a northwest striking, east dipping ductile shear zone exposed in eastern San Diego County (Fig. 3.1). This structure, which is approximately coincident (±10 km) with many of the major chemical, petrological, and mineralogical transitions between western and central zones (e.g. Silver et al., 1979), has traditionally been identified as an Early Cretaceous suture between North America and the Santiago Peak arc (e.g., Todd et al., 1988). However, a recent study of the structural evolution of the CLMSZ by Thomson and Girty (1994) reinterpreted Early Cretaceous deformation exhibited by the structure as having resulted from strain concentration upon a preexisting lithospheric boundary between oceanic and continental crusts. This interpretation is largely based on the observation that the continentally derived strata of the Julian Schist are present on both sides of the CLMSZ. We believe that the designation of this structure as an intra-arc shear zone by Thomson and Girty (1994) and not an arc-continent suture is consistent with the data present in this paper.

The juxtaposition of the Alisitos arc with the central zone implies that a substantial portion of the western margin of North America in this region must have been removed. This follows from the interpretation that the Alisitos arc, unlike the Santiago Peak arc, did not develop across the former accretionary prism, but rather, was built on oceanic crust. Wetmore et al. (2002) proposed two hypotheses to explain the missing accretionary prism: strike-slip translation, and subduction. They cite the observed steep lineation with northeast side up sense of shear along the Main Mártir thrust and lack of

kinematic indicators suggesting a component of lateral translation in this area to argue that the missing terrane was most likely subducted beneath the central zone. They further suggest a means of testing this hypothesis through the geochemical study of the Late Cretaceous intrusive bodies present in the central zone of the Peninsular Ranges batholith north and south of the Agua Blanca fault. In this instance, if the accretionary prism south of the Agua Blanca fault was subducted it should be recorded as an identifiable chemical signature within these magmas (e.g., Ducea, 2001) and be absent from magmas north of the fault.

During the Late Cretaceous the entire length of the central zone of the Peninsular Ranges batholith experienced an enormous amount of exhumation and denudation (Lovera et al., 1999; Schmidt, 2000; Kimbrough et al., 2001). This uplift and associated deformation has commonly been attributed to the accretion or reaccretion of the western zone of the batholith (e.g., Todd et al., 1988). However, if the above model is correct then accretion only affected the central zone adjacent to the Alisitos arc and no such mechanism can be called upon to drive the Late Cretaceous event in the central zone adjacent to the Santiago Peak arc. Additionally, the timing of this exhumation event, between 100 and 85 Ma (Schmidt, 2000), is as much as 15 m.y. after the accretion of the Alisitos arc to the continental margin indicating that even this accretion event was unlikely to have been fully responsible for the observed Late Cretaceous uplift and exhumation in the central zone adjacent to the Alisitos arc.

In the absence of terrane accretion to drive deformation and exhumation within the central zone of the Peninsular Ranges batholith two alternative models have been proposed: increased coupling between the subducting and overriding plates at the trench

(Schmidt et al., 2002), and the thermal-mechanical effects associated with the emplacement of the volumetrically large La Posta suite of plutons (Kimbrough et al., 2001). While the temporal overlap between magmatism, uplift and exhumation are enticing, the true mechanism(s) for magmatism to drive the latter two processes are simply too vague at present to view the coincidence of these events as one of cause and effect. Additionally, the temporal overlap between the La Posta event and uplift is only partial in that uplift both pre- and postdates the magmatic event by several million years each. Conversely, the relative plate motion vectors (Engebretson et al., 1985) indicate a high angle of convergence between North America and subducted oceanic crusted during the 100 to 85 Ma time at relatively high velocities which is consistent with an increased coupling model. However, additional constraints are required to further resolve the mechanism(s), which drove this Late Cretaceous event.

Alternative Models

Tectonic models discussed in the introduction require some dramatically different processes and tectonic geometries to explain the present configuration of the Peninsular Ranges. These include the rifted-fringing arc model (Gastil et al., 1981; Busby et al., 1998) and the accretion of an exotic east facing island arc (Dickinson and Lawton, 2001). The rifted-fringing arc model proposed by Gastil et al. (1981) and Busby et al. (1998) is based on observations made from areas both north and south of the ancestral Agua Blanca fault, as well as from the Continental Borderlands terrane.

Rifted-fringing arc models are commonly based on the observation of large amounts of "flysch-like" strata preserved within the central portions of batholiths (e.g., Gastil et

al., 1981). Gastil et al. (1981) and Gastil (1993) correlated the turbidite sequences of the central zone for the entire length of the batholith and identified them all as "Triassic-Cretaceous back-arc clastics." The Gastil et al. (1981) model proposes that the entire western zone of the batholith was rifted from the continental margin in the Triassic, allowing for the deposition of these strata. Several objections can be raised against this interpretation. First, if a fragment of the continent were rifted in the Triassic, then the ages of the strata should be older in the western and eastern zones and younger in the central zone. This is not consistent with the age distributions of central zone strata, either north or south of the ancestral Agua Blanca fault. Second, if rifting and the development of a fringing arc occurred in the Triassic, volcanics and plutonics of this age should be present in the western zone. While some Jurassic epiclastically reworked volcaniclastics have been observed in central San Diego County their volume is far to small to support the their interpretation as a Triassic-Jurassic arc. Triassic magmatism may be preserved in eastern San Diego County (e.g., Thomson, 1994), but no evidence supports the existence of an arc of this age in the western zone north or south of the ancestral Agua Blanca fault.

The rifted-fringing arc model proposed by Busby et al. (1998) is based on observations of the western zone in the area south of the ancestral Agua Blanca fault (e.g., Fackler-Adams and Busby, 1998) and stratigraphy preserved in the Continental Borderlands terrane. Busby et al. (1998) partition their model into three phases which correspond to time periods of 220-130 Ma (Phase one), 140 to 100 Ma (Phase two), and 100 to 50 Ma (Phase three). In their model phase one represents the rifting of a fragment of the continental margin to form the extensional fringing arc of phase two which

ultimately becomes reaccreted to the continental margin during phase three. In general the same objections that were raised against the Gastil et al. (1981) rifted-fringing arc model apply here. However, there are several additional complications from the Busby et al. (1998) model that are described below.

The identification of an early Mesozoic accretionary prism with continental ties (e.g., Boles and Landis, 1984; Sedlock and Isozaki, 1990) within the Continental Borderlands terrane implies that this terrane must have been adjacent to a continent in the Mesozoic. However, strike-slip translation of this terrane during the Late Cretaceous (e.g., Busby et al., 1998) makes correlations between the Jurassic and Early Cretaceous strata of the Continental Borderlands terrane and the Early Cretaceous arc strata of the western zone of the Peninsular Ranges batholith highly suspect. Presently, no data exist to indicate that the Continental Borderlands were adjacent to the Peninsular Ranges batholith prior to the Late Cretaceous (e.g., Klinger et al., 2000).

Detailed mapping of structures and stratigraphic sequences within the Alisitos arc southeast of San Quintin by Fackler-Adams and Busby (1998) form the basis for events in phases one and two of the Busby et al. (1998) model. It is important to note here that strata and intrusive bodies older than ~116 Ma have not been identified within the Alisitos arc. Therefore, none of phase one and only the last 16 million years of phase two are potentially represented in this part of the Peninsular Ranges. This 16 m.y. coincides with the time when we propose that the Alisitos arc is characterized by northeast-southwest directed shortening associated with its accretion to the continental margin. Fackler-Adams and Busby (1998) however, argue for a rifting arc model based on the presence of northeast-trending dikes and small-offset (<100 m) normal faults, and ~200

m of basalts capping the section. Their interpretation of these observations seems somewhat overstated given that all extensional features are oriented perpendicular to the extension directions suggested by Busby et al. (1998), and that the magnitudes of fault offset and dike-induced dilation are all very small. Furthermore, the relatively small volume of basaltic lavas termed "rift-related," could just as easily be ocean island basalts. No reported chemical data support the designation of these lavas as being rift-related. Similarly, north of the ancestral Agua Blanca fault the identification of extensional structures and volcanic petrologies have not been reported even though a greater percentage of the time discussed in the Busby et al., (1998) model is preserved in the rock record.

Finally, if the western zone of the Peninsular Ranges were to have developed as a reaccreted rifted-fringing arc, at least some proportion of the basement of this fringing arc must have be composed of continentally-derived materials. It therefore follows that volcanics and plutonics that were emplaced through and deposited on these continental materials should show some contamination, such as that observed in the Santiago Peak Volcanics and associated plutonic units. However, this is not the case for the Alisitos arc. We conclude that models identifying any portion of the western zone of the Peninsular Ranges batholith as having evolved as a rifted-fringing arc are untenable.

Dickinson and Lawton (2001) recently proposed a tectonic model wherein the western zone of the Peninsular Ranges batholith, as part of the larger Guerrero superterrane, originated as an east facing island arc, exotic to North America. This proposal arises from supposition that the only proposed alternative models are one of a rifted-fringing arc (e.g., Busby et al., 1998), combined with the observation of east-

directed thrusting along the eastern margin of the Guerrero superterrane in mainland Mexico (Tardy et al., 1994). Dickinson and Lawton (2001) are also influenced by the tradition of poorly constrained age ranges for magmatism within the western zone of the batholith (i.e. that it was a Jurassic-Cretaceous arc).

As discussed in detail above, models supporting the accretion of the western zone of the Peninsular Ranges batholith (either as an east or west facing arc) do not conform with the relationships that exist between the Santiago Peak Volcanics and the continentally-derived Bedford Canyon Complex. South of the ancestral Agua Blanca fault the Alisitos arc and adjacent central zone define a broad west-vergent fold and thrust belt. Early Cretaceous east-vergent structures are known locally from the eastern zone in the southern Sierra San Pedro Mártir area (Schmidt, 2000) but have not been reported from most areas of the Peninsular Ranges. If the Alisitos arc had been an east-facing arc, and a contemporaneous west-facing continental arc existed in the present location of the central zone, then the accretionary prisms associated with both of these arcs have been removed. Given the lack of east directed structures to support this interpretation, the additional tectonic complexity of having to remove an additional accretionary prism seems unnecessary. Finally, given the descriptions here of the dramatic differences in the tectonic evolution of the Peninsular Ranges across the ancestral Agua Blanca fault, then there is no reason to think that similar transitions cannot exist between the Peninsular Ranges and its on-strike continuation in mainland Mexico.

Conclusions

The Mesozoic tectonic evolution of the southwestern margin of North America has been one of the more poorly resolved aspects of Cordilleran geology. A variety of competing models have been proposed, most of which disagree on even the most fundamental aspects (e.g., origin of the western zone of the Peninsular Ranges). We suggest that, in part, the differences between these models are the result of tectonically significant variations in the along-strike character of the continental margin which are most pronounced across the Agua Blanca fault of northern Baja California, Mexico. Variations across this fault can be observed in the geology of the central and western zones of the Peninsular Ranges strata as old as the Late Triassic. These variations include: (1) the presence or absence of Late Triassic through Jurassic continentally-derived turbidite sequences (north) and/or Early Cretaceous submarine sedimentary strata (south), (2) the environment of deposition of Early Cretaceous western zone volcanics, and contact relations between these volcanics and the continentally-derived strata of the central zone (depositional, north; fault, south), (3) presence of xenocrystic Precambrian zircons in plutons and volcanic flows of the western zone (present, north; absent, south), (4) the frequency of lava types of western zone volcanics (abundant rhyolites, north; abundant basalts, south), (5) the general distribution and intensity of deformation within the western zone (minor to moderate, north; 20 km wide fold and thrust belt, south), and (6) the character of deformation associated with the ancestral Agua Blanca fault (truncation, north; deflection into subparallelism, south).

We propose a model that specifically incorporates these along-strike variations. During Late Triassic through Jurassic, the central zone north of the ancestral Agua

Blanca fault was the site of sedimentation of continentally derived turbidite sequences that were ultimately incorporated and deformed within an accretionary prism setting. We propose that all of the Late Triassic through Jurassic strata of similar lithology present within the central zone north of the Agua Blanca fault should be included within a single stratigraphic group; here termed the Bedford Canyon Complex. By the Early Cretaceous, the Bedford Canyon Complex was uplifted and exposed to subaerial erosion prior to the unconformable deposition of the Santiago Peak Volcanics. South of the ancestral Agua Blanca fault the central zone was generally not submerged as it was to the north, and thus deposits of Late Triassic through Jurassic age are only preserved locally in this part of the batholith. The outboard trench and accretionary prism (i.e. Bedford Canyon Complex correlative strata) presumably existed west of the present day central zone. During the latest Jurassic through Early Cretaceous the central zone south of the ancestral Agua Blanca fault became submerged below sea level and filled with shallow to deep water sediments overlain by subaqueously deposited volcanics that grade upward into a subaerial volcanics. Contemporaneous with Early Cretaceous basin sedimentation in the central zone, the Alisitos arc initiated on oceanic crust not previously associated with the continental margin. The Alisitos arc impinged upon the continental trench between 115 and 108 Ma and during accretion forcing the subduction of the associated accretionary prism. While some uplift and exhumation of the central zone adjacent to the Alisitos arc may be attributed with the accretion of that arc the majority of this central zone event is most likely caused by increased coupling between the continent and the subducting slab.

CHAPTER 4: THE ANCESTRAL AGUA BLANCA FAULT: THE NORTHERN TERMINATION TO THE ALISITOS ARC SEGMENT, WESTERN PENINSULAR RANGES, BAJA CALIFORNIA, MEXICO

Introduction

The Phanerozoic western continental margin of North America was characterized by a substantial component of tectonic accretion during much of the late Paleozoic and throughout the Mesozoic. The new continental growth that resulted from this general process is necessarily complicated. This complication arises, not only from post-accretion tectonic disruption (e.g., Suppe, 1970; Hall, 1991), but also from fundamental differences in the amount and type of material impinging upon, and ultimately becoming attached to, the continental margin along the strike of the paleotrench. Examples of added tectonic elements includes slices of oceanic crust (e.g., Coast Ranges Ophiolite), island arcs (e.g., Seven Devils Terrane), and the sediments/volcanics deposited on the ocean floor at varying distances from spreading centers, ocean islands, and continents (e.g., Western Metamorphic Belt of the Sierra Nevada foothills). Between each of these tectonic elements must exist faults of variable type that accommodated the differential displacements between each element and ultimately juxtaposed them. These combining structures can have deformational histories associated with them that are comparable in scale and magnitude to the structures juxtaposing the accreted elements themselves with the continental margin but, are often less-well defined geologically.

While structures juxtaposing various accreted tectonic elements may have been identified, the transitions between these accreted tectonic elements are not as easily

distinguished using techniques such as pluton/volcanic geochemical surveys and regional scale studies of stratigraphy. This follows from the fact that since the majority of the material accreted onto continental margins originated within the oceanic realm, they tend to have shared common magmatic events that fundamentally define their chemical compositions. For example, oceanic lithosphere (ophiolites), including the basements of island arcs, have undergone a major melting event producing the typical MORB (Mid-Ocean Ridge Basalt) type chemical signatures. Subsequent magmas generated within these terranes, therefore, will bear a heavy imprint of this prior magmatic event, thus making tectonically significant chemical differences are difficult to recognize. Similarly, since many of the accreted blocks appear to be island arc complexes identification of tectonically significant transitions difficult to identify because lateral variations in the volcanogenic stratigraphy of a single arc are typical.

As a result of these difficulties in identifying tectonic boundaries between accreted terranes some over correlation of terranes has occurred. This appears to be the case in western and southwestern Mexico where numerous tectonic reconstructions have combined volcanic terranes from the Guerrero in mainland Mexico, with the western Peninsular Ranges of southern and Baja California (e.g., Campa and Coney, 1981; Dickinson and Lawton, 2001). In all of these areas Jurassic(?) and Cretaceous arc volcanics, largely deposited subaqueously, and associated intrusives possess primitive "island arc"-like chemical signatures and were deformed penecontemporaneously (~120-100 Ma). However, the details of a number of different data sets do not support the grouping of the rocks in all of these areas into one tectonic element that evolved as a single block (e.g., Wetmore et al., 2002, in press). Rather, those data sets seem to suggest

that these volcano-plutonic terrains are composed of at least three terranes each having experienced distinct origins and tectonic evolutions (Wetmore et al., 2003; see chapter 3). In chapter 3 I argue that the Santiago Peak segment developed as a continental margin arc built on an accretionary prism previously formed on the North American continental margin, the Alisitos arc developed on oceanic lithosphere not previously associated with a continental margin, and the Guerrero segment may in itself be a composite of multiple arcs (oceanic?-continental?) whose relationships to continental lithosphere are not clear (Tardy et al., 1994). The boundaries between each of these segments have not been studied previously, though the presence of a break between the Santiago Peak and Alisitos near the trace of the active Agua Blanca fault (ABF) has been alluded to previously (Gastil et al., 1975; 1981; Armijo and Suarez-Vidal, 1981). This paper presents the results of a detailed study of the tectonic boundary between the Santiago Peak and Alisitos segments of the western Peninsular Ranges of southern and Baja California (Fig. 4.1), identified as the ancestral Agua Blanca fault (aABF) by Wetmore et al. (2002). For a more complete description of the working tectonic model the reader is referred to Chapters two and three.

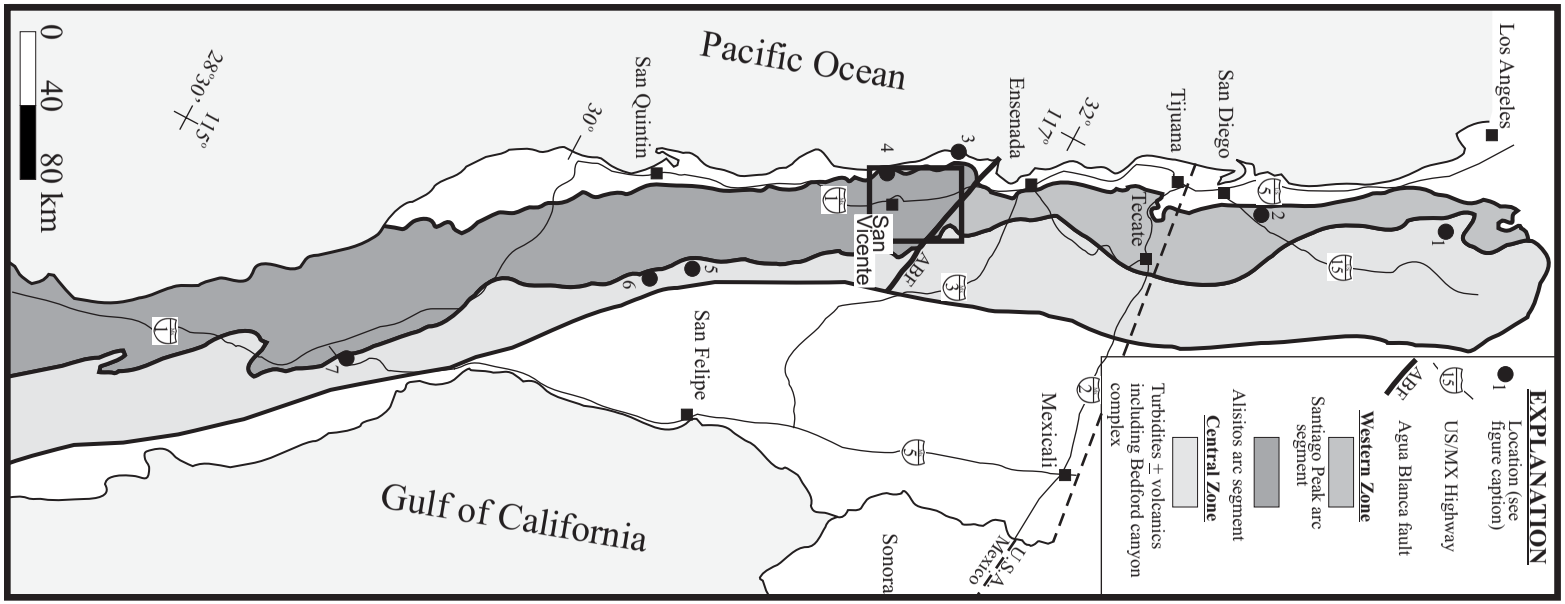

Figure 4.1. Regional map of the Peninsular Ranges of southern and Baja California showing distribution various stratigraphic units and locations discussed in the text. Numbered locations correspond to 1) Santa Ana Mountains, 2) Lusardi Canyon, 3) Punta China, 4) Eréndira, 5) northern Sierra San Pedro Mártir (study area for Johnson et al., 1999a,b, and 2003; Tate et al., 1999; Tate and Johnson, 2000), 6) southern Sierra San Pedro Mártir (study area for Schmidt, 2000; Schmidt and Paterson, 2003), and 7) Sierra Calamajue. Figure is modified after Gastil (1993).

Geology across the ancestral Agua Blanca fault

The area mapped in this study is located approximately 80 km south of Ensenada, Mexico (Fig. 4.1). Detailed mapping of this region was completed at a 1:10,000 scale for an area of ~135 km^2. Reconnaissance mapping (1:50,000 scale), assisted by air and satellite photos, was used to broaden the map incorporating areas adjacent to the main transect (Fig. 4.2). The map area can be divided into two segments along the aABF with the Santiago Peak to the north and the Alisitos to the south. Discussion of the geology of the aABF region below proceeds from stratigraphic analyses, to structural geology, and then to geochemistry and geochronology with a brief account of similar data sets for each topic collected from other parts of the western Peninsular Ranges and then the data collected from the study area.

Stratigraphy, Depositional Environment, and Provenance: Santiago Peak Volcanics

The Santiago Peak Volcanics, exposed from the Santa Ana Mountains of southern California to the aABF (Fig. 4.2), represent the Early Cretaceous stratigraphy of the Santiago Peak arc segment. The volcanics exhibit a compositional range from rhyolites to basalts with andesites and dacites being the most common (Schroeder, 1967; Adams, 1979; Buesch, 1984; Gorzolla, 1988; Herzig, 1991; Reed, 1992; Meeth, 1993). Studies of the Santiago Peak Volcanics typically conclude that they were deposited subarially (Adams, 1979; Herzig, 1991; Carrasco et al., 1994) based on the lack of laterally extensive sedimentary sequences interbedded with the volcanics and the numerous ash fall units that contain accretionary lapilli (Carrasco et al., 1993). Previous correlations of

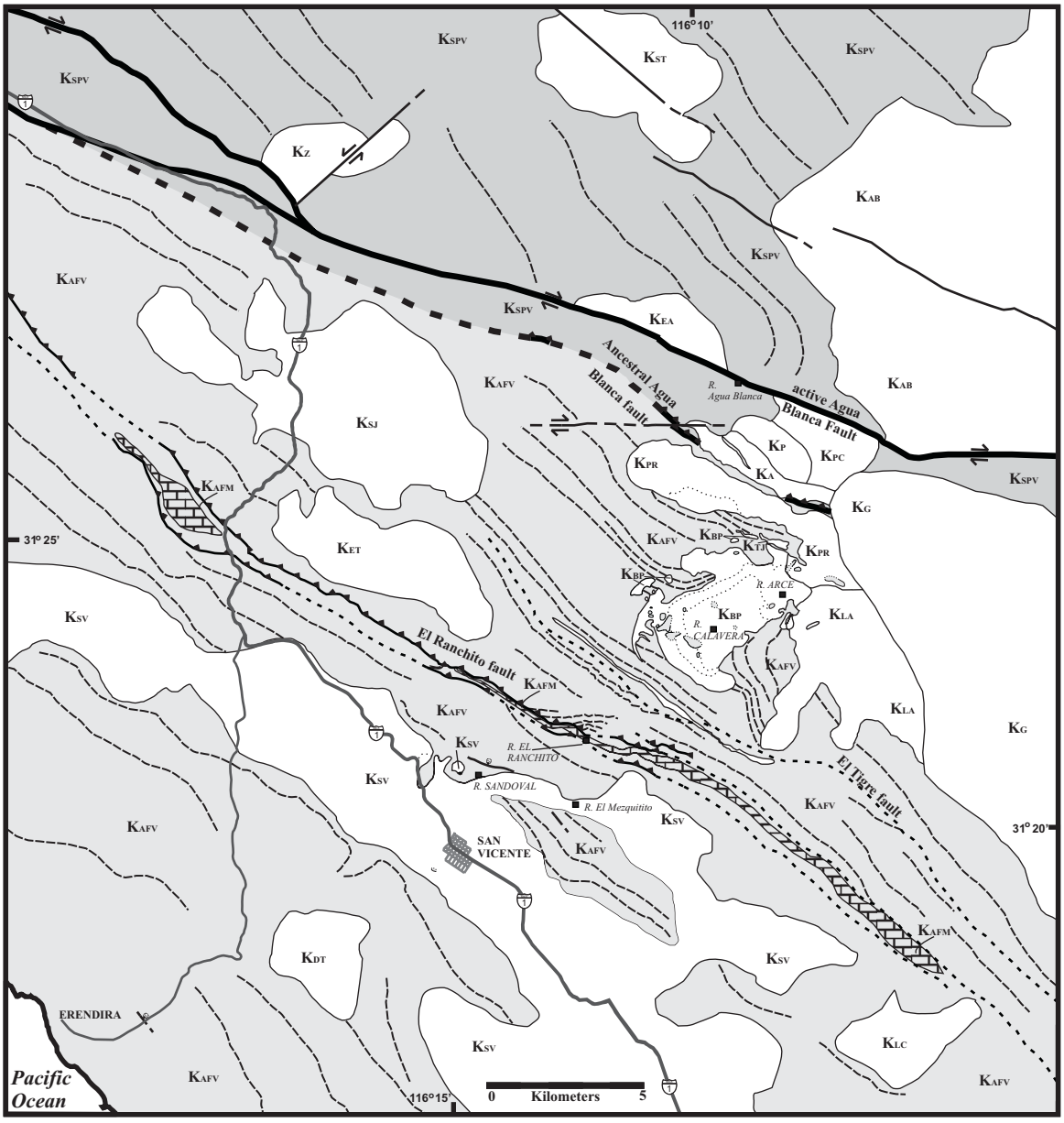

Figure 4.2. Geologic map of the ancestral Agua Blanca fault region.

Late Jurassic volcaniclastics interbedded with marine shales in Lusardi Canyon of San Diego County (Fig. 4.1) with the Santiago Peak Volcanics (Fife et al., 1967) have been interpreted as untenable due to considerations of depositional age (Anderson, 1991) and structural relationships between the marine strata and overlying volcanics more typical of the Early Cretaceous Santiago Peak Volcanics (Wetmore et al., In press; Chapter 3).

The small area of the Santiago Peak arc mapped in this study allows for only a limited description of the Santiago Peak Volcanics at the southern extreme of the arc segment. Notwithstanding, the Santiago Peak Volcanic stratigraphy exposed within the study area do exhibit the characteristics commonly observed in the section elsewhere. Here, compositions of volcanic units typically range between andesite and dacite with a few rare lava flows with compositions of basalt or basaltic andesite. Rhyolites were not observed within this study area. Coarse-grained volcaniclastic sandstones were observed, although they were thin (<~10 cm) and very limited in number relative to the primary volcanic units. Accretionary lapilli were only observed in two localities in the study area, one just north of the aABF. Exposures of the Bedford Canyon Complex, the unit that presumably underlies the Santiago Peak Volcanics (discussed above), are not exposed in any part of the study area.

Stratigraphy, Depositional Environment, and Provenance: Alisitos Formation

The Early Cretaceous Alisitos Formation, exposed from the aABF to just north of the state boundary between Baja California Norte and Sur (Fig. 4.1), is the principle stratigraphic unit representing the Alisitos arc segment. The formation is composed of a heterogeneous mix of primary volcanics (lavas and ash flows/falls) that exhibit the same

compositional range as the Santiago Peak Volcanics, ubiquitous reworked (epiclastic) volcaniclastics, and numerous limestone (now marble) units (Allison 1955, 1974; Leedom, 1967; Reed, 1967; Beggs, 1984; Suarez-Vidal, 1986, 1993; Fackler-Adams and Busby, 1998; Johnson et al., 1999a). A marine environment of deposition is indicated, not only by the lithology of the Alisitos Formation but also by the presence of marine fossils such as rudistids (Allison, 1955), which have been reported from nearly all areas mapped within the Alisitos arc segment.

In a recent study of the Alisitos arc segment near the northern Sierra San Pedro Martír (Fig. 4.1) Johnson et al., (1999a) subdivided the Alisitos Formation into a western volcanics-dominated belt and an eastern volcaniclastics-dominated belt. Suarez-Vidal (1986, 1993) similarly delineated an Aptian-Albian sedimentary basin (dominated by volcanic detritus) present along the northeastern margin of the arc segment south of the aABF. Johnson (University of Maine, personal communication, 2003) observed that the eastern belt, which is bound by two large southwest vergent thrust faults in his area, fines towards the top of the section suggesting a rapid deepening of the basin into which the sediments were deposited. Similar observations (Robert Douglas, University of Southern California, personal communication, 2003) were recently made in the potential northern continuation of this basin along the Pacific coast near Punta China (Fig. 4.1). Johnson et al. (1999a) argued that the strata in this eastern (and presumably northeastern) belt were deposited into an interarc basin trapped between the Alisitos arc and the North American continental margin as the former arc approached the trench that was consuming the plate upon which the Alisitos arc had developed. However, it should be noted here that study of this basin from a sedimentological standpoint is very limited at present and such

interpretations of tectonic setting for this basin should be viewed with caution. In contrast to the Santiago Peak Volcanics, the stratigraphy of the Alisitos Formation have been studied in some detail in areas south of the aABF. Figure 4.3 is a structural stratigraphic section constructed from observations made of the Alisitos Formation during mapping of the region between the aABF and the San Vicente pluton (K_{SV}, Fig. 4.2). Strata of the Alisitos Formation between the San Vicente pluton and the Pacific coast at Eréndira have been omitted from this section due to limited knowledge of the stratigraphy in that part of the study area.

Similar to other studies of the Alisitos Formation, the strata here are composed of a heterogeneous mix of lithologies with abundant evidence for subaqueous deposition throughout. However, several ash fall units do contain accretionary lapilli, volcanic features often considered indicative of subarial eruptions and deposition (e.g., Carrasco et al., 1993). Such an interpretation is somewhat difficult to apply unilaterally in this instance due to the observation that, in at least one case, the accretionary lapilli-bearing ash fall unit is bound on both sides by fine-grained shale layers and is stratigraphically within a few meters of a thin (<0.5 m) limestone unit.

The stratigraphy represented in Figure 4.3 includes 6 km of section contained within three fault blocks (note that the aABF truncates the top of the section and the San Vicente pluton intrudes the bottom of the section). The component stratigraphy of each fault-bound section exhibits several features that distinguish it from the others. For example, the structurally lowest section contains a very thick (~0.5 km) succession of densely welded, dacitic ash flow tuffs that characterized columnar jointing, followed by a sequence (~1 km thick) of alternating ash flows/falls bound by similarly proportioned

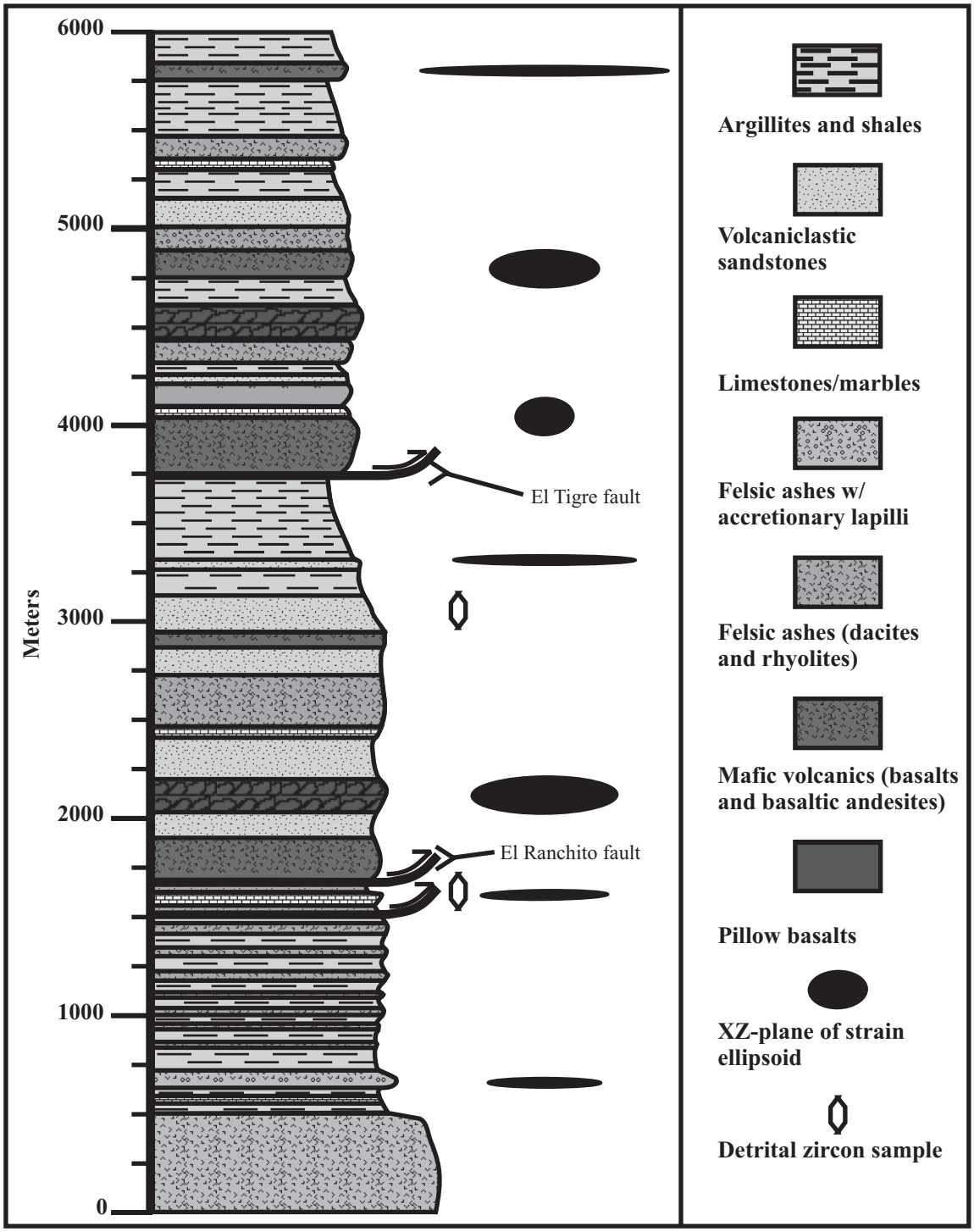

Figure 4.3. Stratigraphic column for the Alisitos Formation in the central part of the ancestral Agua Blanca fault study area.

shale layers with rare interbedded limestones. At the top of this lowest section of the column are a series of coarse-grained volcaniclastic sandstone units and a thick (50-100 m) limestone (marble) unit all between the El Ranchito and an unnamed fault. These units are included with the lowest section due to the small inferred offset on the lower, unnamed fault. The limestone unit in this part of the section is part of a relatively large, regionally extensive unit that can be traced from Punta China to the northern Sierra San Pedro Mártir area (Silver et al., 1963). The lower 2/3 of the middle section of the column is comprised of mafic primary volcanics (lava/ash flows, and ash fall deposits) interbedded with coarse-grained volcaniclastic sandstones. The upper third of the middle section is dominated by fine grained argillites and lesser volcaniclastic sandstones. While the lower half of the uppermost section of the column is also composed of numerous primary volcanics, including a basaltic unit, volcaniclastic sandstones are relatively rare while fine grained argillites are more commonly intercalated with the volcanics. The top half of the uppermost section is dominated by thick successions of fine grain argillites similar to the upper part of the middle section of the column.

U-Pb analysis of detrital zircon populations was conducted on two samples of coarse-grained sandstone collected from the top of the lower-most section (sample 6/6/00-F), and from ~800 m below the top of the middle section (sample 5/19/00-A; Figs. 4.3 and 4.4). Twenty-two and 53 zircons, respectively, were analyzed by George Gehrels using a LA-MC-ICPMS at the University of Arizona (see Appendix A for description of analytical procedures). The $^{206}Pb/^{238}U$ ages for the zircons analyzed range from 102.9 ± 3.3 to 1550.1 ± 61.7 Ma for sample 6/6/00-F and from 100 ± 2.8 to 2758 ± 16.9 Ma for

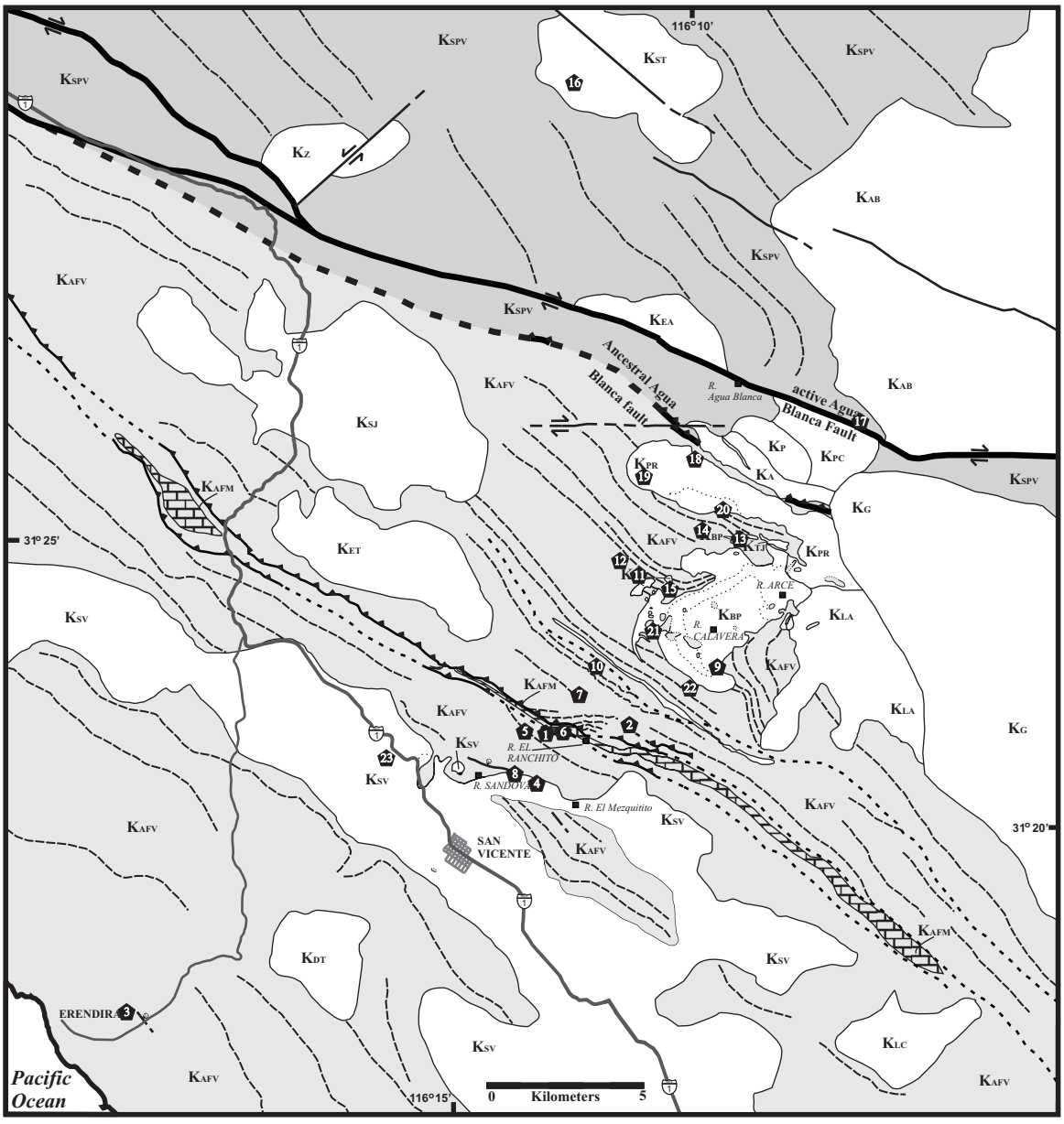

Figure 4.4. Geologic map of the ancestral Agua Blanca fault study area showing sample locations. Table 4.1 relates the sample number shown on map to sample name.

sample 5/19/00-A (Fig. 4.5; Appendix A, Table A.1). Nearly all of the zircons analyzed from sample 6/6/00-F (20/22) yield latest Late Jurassic through latest Early Cretaceous ages. Conversely, less than half of the zircons from sample 5/19/00-A yield ages within this range with a much greater percentage (~40%) of Paleozoic and Precambrian grains, including two that yield Archean ages.

Table 4.1. List of samples collected and analyzed from the ancestral Agua Blanca fault study area. Location number corresponds to the map in Figure 4.4.

PHW Sample	Loc. Number	Strain	Geochron	Geochem
6/6/00-F	1		x	
5/19/00-A	2		x	
2/24/01-A	3	X		
2/24/01-B1	3	X		
2/24/01-B2	3	X		
2/24/01-B3	3	X		
2/24/01-B4	3	X		
2/24/01-B6	3	X		
2/24/01-C	3	X		
2/24/01-C1	3	X		
5/21/00-C	4	X		
5/26/00-C	5	X		
6/9/00-D	6	X		
6/9/00-I	6	X		
6/13/00-E	7	X		
6/13/00-F	7	X		
6/22/00-B	4	X		
6/22/00-M	8	X		
5/7/01-J	9	X		
5/17/01-P	10	X		
6/5/01-A	9	X		
6/6/01-H	11	X		
6/6/01-N	12	X		
6/24/01-J	13	X		
6/25/01-G	14	X		
6/25/01-H	14	X		
7/6/01-T	15	X		
5/29/01-B	16		X	X
1/8/03-H	17		X	X
7/3/01-J	18			X
7/1/01-F	19			X
7/6/01-S	20		X	
6/9/01-B	21		X	X
6/9/01-F	22		X	X
1/12/03-A	23		X	X

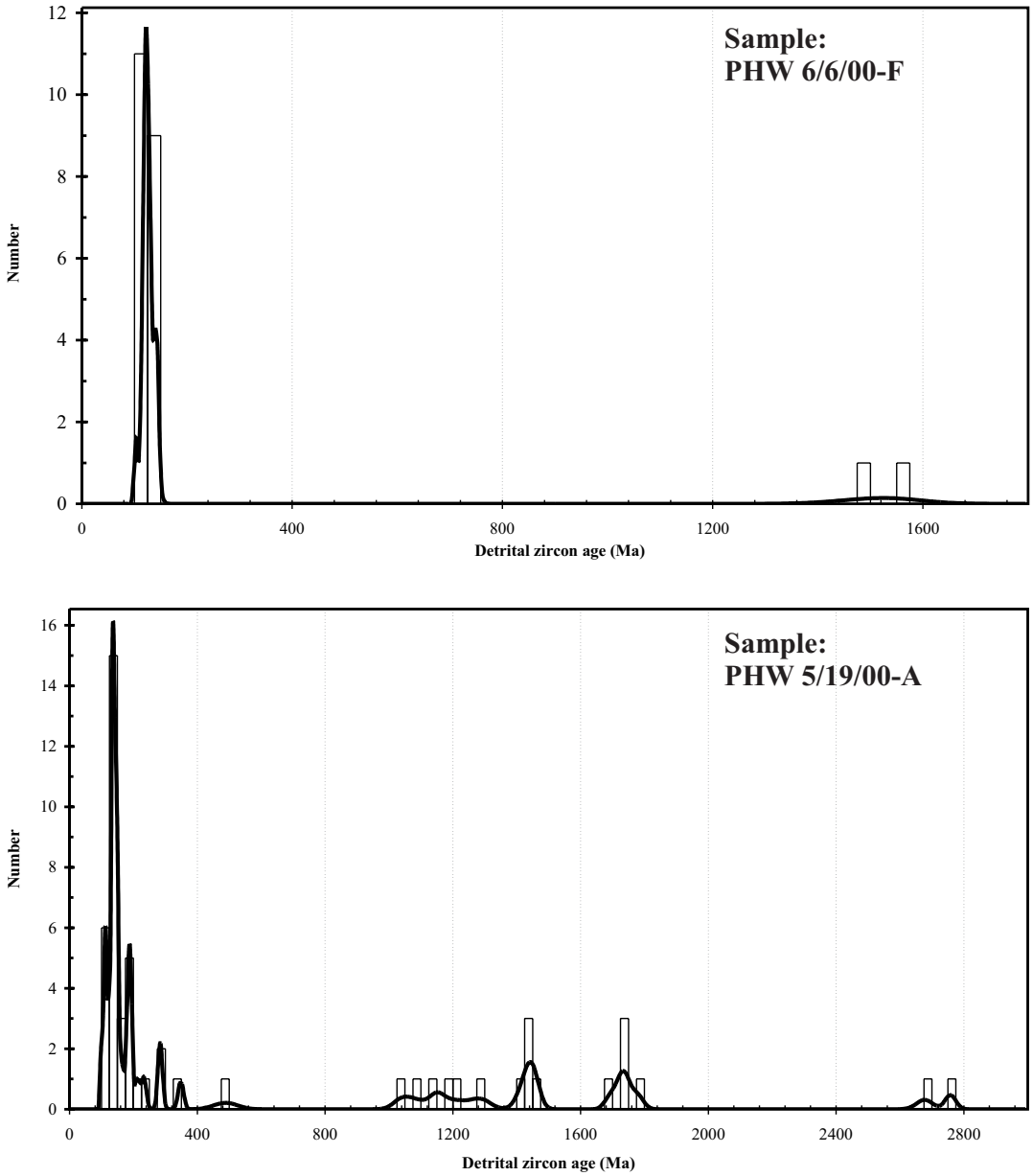

Figure 4.5. Probability density distribution plot of U/Pb ages of detrital zircons for samples collected from the Alisitos Formation.

Structural Geology: Santiago Peak arc segment

The total amount of structural data collected from the Santiago Peak arc segment is small as it is largely derived as a by product of studies that were focused on the stratigraphy and petrology/geochemistry of the Santiago Peak Volcanics (e.g., Adams, 1979). The general impression these data provide is that the Santiago Peak Volcanics are not intensely deformed except within local structural aureoles of plutons. This view gained support recently from the results of a study that concluded that the contact between the Santiago Peak Volcanics and the underlying Bedford Canyon Complex was an unconformity with little deformation occurring subsequent to the deposition of the overlying volcanics (Sutherland et al., 2002).

In contrast to most of the Santiago Peak, the deformation observed from the southern-most part of the arc segment is quite intense and affects, not only the Santiago Peak Volcanics, but also some of the associated intrusive bodies. The intensity of deformation increases towards both plutons in this part of the arc segment as well as the aABF.

Several upright and tight folds have been mapped in the Santiago Peak Volcanics north of the active ABF between the El Alemán pluton (K_{EA}) and the Agua Blanca pluton (K_{AB}; Fig. 4.2). These folds exhibit a variable wavelength between one and three kilometers, decreasing toward the margin of the El Alemán pluton. The traces of fold axes, and the strikes of the beds forming the folds, exhibit an ~90° clockwise rotation (from ~300° to ~030°) as the active ABF is approached from the north. Foliations, typically bedding parallel, exhibit the same deflection as the fold axis traces and bedding but also exhibit an increasing intensity over the same region. This fabric intensity

gradient continues across the active ABF as exposures of the Santiago Peak Volcanics just north of the aABF are characterized by the highest intensity foliation in rocks north of the latter fault. However, unlike the Alisitos Formation to the south of the aABF, the Santiago Peak Volcanics are not mylonitized and in fact, some primary depositional features (e.g., accretionary lapilli) are preserved.

A well-developed stretching lineation plunging steeply in the foliation plane (subparallel to dip) is present in most exposures of the Santiago Peak Volcanics. This lineation is defined by elongate breccia fragments or streaking of mineral aggregates. Asymmetries exhibited by the breccia fragments in foliation perpendicular and lineation parallel planes were used to interpret kinematics. In every instance asymmetries indicated a northeast side up, reverse sense of shear. The clockwise deflection of bedding and foliation observed in the Santiago Peak Volcanics immediately north of the active ABF is a significant exception to overall kinematic interpretation for this region. Here the amount of deflection increases with proximity to the active ABF and the sense of deflection suggests dextral shear, consistent with that observed across the active structure. In exposures <3 km north of the active ABF where bedding/foliation strikes have been rotated the kinematics determined from asymmetries within the Santiago Peak Volcanics are sympathetic with the northeast side up, reverse shear sense once the more recent deflection is restored (e.g., east side up for a due north strike).

Structural Geology: Alisitos arc segment

In contrast to the Santiago Peak arc segment, a few modern structural studies have been completed on the Alisitos arc segment. These studies have typically focused on the

structural transition between the arc segment and the central part of the Peninsular Ranges batholith (e.g., Goetz, 1989; Griffith and Hoobs, 1993; Johnson et al., 1999a; Schmidt and Paterson, 2003). The transition from the arc segment to the central part of the PRb corresponds to the Main Mártir Thrust, a ductile shear zone that is interpreted to represent a non-terminal suture (Johnson et al., 1999a; Schmidt and Paterson, 2003). The general structural geology view of the Alisitos arc segment derived from these previous studies includes a deformation gradient from essentially none on the west up to very intense along the transition to the east. The gradient in deformation is represented by an eastward tightening of folds and dramatic increases in the magnitudes of tectonic strains measured from within the southwest-vergent fold and thrust belt present to the west of the Main Mártir thrust.

The Main Mártir thrust can be traced discontinuously for more than 300 km along the axis of the Baja Peninsula from the approximate latitude of San Vicente south to the Sierra Calamajue (Fig. 4.1). Evidence that this structure played a key role in the tectonic development of this part of the Peninsular Ranges is indicated by a large number of data sets. For example, this boundary is coincident with several major transitions in stratigraphy, pluton geochemistry and Fe-Ti oxide minerals, as well as geophysical characteristics (e.g., Gastil et al., 1975; Taylor and Silver, 1978; Gromet and Silver, 1987; Gastil, 1990, 1993). The Main Mártir thrust is also coincident with a pronounced step in the level of crustal exposure with rocks yielding pressures of ~2 kbars in the Alisitos arc segment juxtaposed with rocks yielding pressures that range from 4 to 6 kbars to the east (Kopf and Whitney, 1999; Schmidt and Paterson, 2002).

The Alisitos Formation, as mentioned above, is subdivided into two parallel belts based on rock type (Johnson et al., 1999a). A volcanics dominated western belt is separated from a volcaniclastics dominated eastern belt by a brittle-ductile southwest vergent reverse fault known as the Rosarito fault. This structure can be traced discontinuously from the northern Sierra San Pedro Mártir study area of Johnson et al. (1999a) south for >50 km where it is cut by the Main Mártir thrust (Schmidt, 2002).

Deformation, in the form of folds and brittle-ductile strain, is observed on both sides of the Rosarito fault (Goetz, 1989; Johnson et al., 1999a,b; Schmidt, 2002). Folds west of the fault range from tight to open to gentle with distance from the fault. The axes of these folds are typically horizontal with axial surfaces nearly vertical or steeply northeast dipping (Schmidt, 2002; Scott E. Johnson, Personal Communication, 2003). Similar to fold tightness, strains decrease from less than 40% shortening in the z-direction to essentially zero away from the Rosarito fault. East of the Rosarito fault, within the volcaniclastics-dominated belt, folds range from tight to isoclinal with increasing proximity to the Main Mártir thrust. Fold axes rotate from nearly horizontal just east of the Rosarito fault to steeply plunging, subparallel to the stretching lineation immediately west of the Main Mártir thrust (Johnson et al., 1999a). Ductile strains exhibit a similar dramatic eastward increase to greater than 65% shortening in the z-direction (Schmidt, 2002).

The deformation associated with the Main Mártir thrust south of the two Sierra San Pedro Mártir study areas (Fig. 4.1) seems to be less broadly distributed and the volcaniclastics dominated basin is either absent or becomes much smaller. Deformation in the Sierra Calamajue, the southern-most known exposure of the Main Mártir thrust, is

no less intense than to the north but, it is concentrated within a zone that is less than about 3 km wide (Griffith and Hoobs, 1993; Alsleben and Paterson, 2003). To the west of the Sierra Calamajue, numerous intrusives and Quaternary valley fill obscure most structural relationships, however deformation appears to be limited to open folds and low strain intensities (<30% shortening in the z-direction; Alsleben and Paterson, 2003). Folds within the Sierra Calamajue, where exposures are typically >80%, are tight to isoclinal with very steep east dipping axial surfaces (Griffith and Hoobs, 1993). Strain intensities here range from 60 to 90% shortening in the z-direction.

Kinematic indicators from both Sierra San Pedro Mártir study areas (fig. 4.1), as well as the Sierra Calamajue suggest a strong component of east over west reverse shear. However, along the Main Mártir thrust in both the Sierra San Pedro Mártir study areas a minor component of sinistral shear (i.e., Alisitos arc segment toward the south relative to the adjacent central part of the PRb) has also been observed (Schmidt, 2002; Scott E. Johnson, Personal Communication with Scott Paterson, 2003).

Structural Geology of the ancestral Agua Blanca fault area.

In the northern Alisitos arc segment the fold and thrust belt is present to the south of the aABF (Figs. 4.2 and 4.6). Here it exhibits an intensity of deformation and width similar to that described for the Sierra San Pedro Mártir study areas. The majority of the fold and thrust belt here is exposed between the aABF and the San Vicente pluton (K_{SV}). It is somewhat complicated here, as with areas further south (e.g., Johnson et al., 1999b; Chavez-Cabello, 1998), by the presence of numerous small (<20 km^2) intrusive bodies that have developed moderately large (~1-2 km) structural aureoles during their emplacement into the Alisitos Formation. However, the distances between each pluton

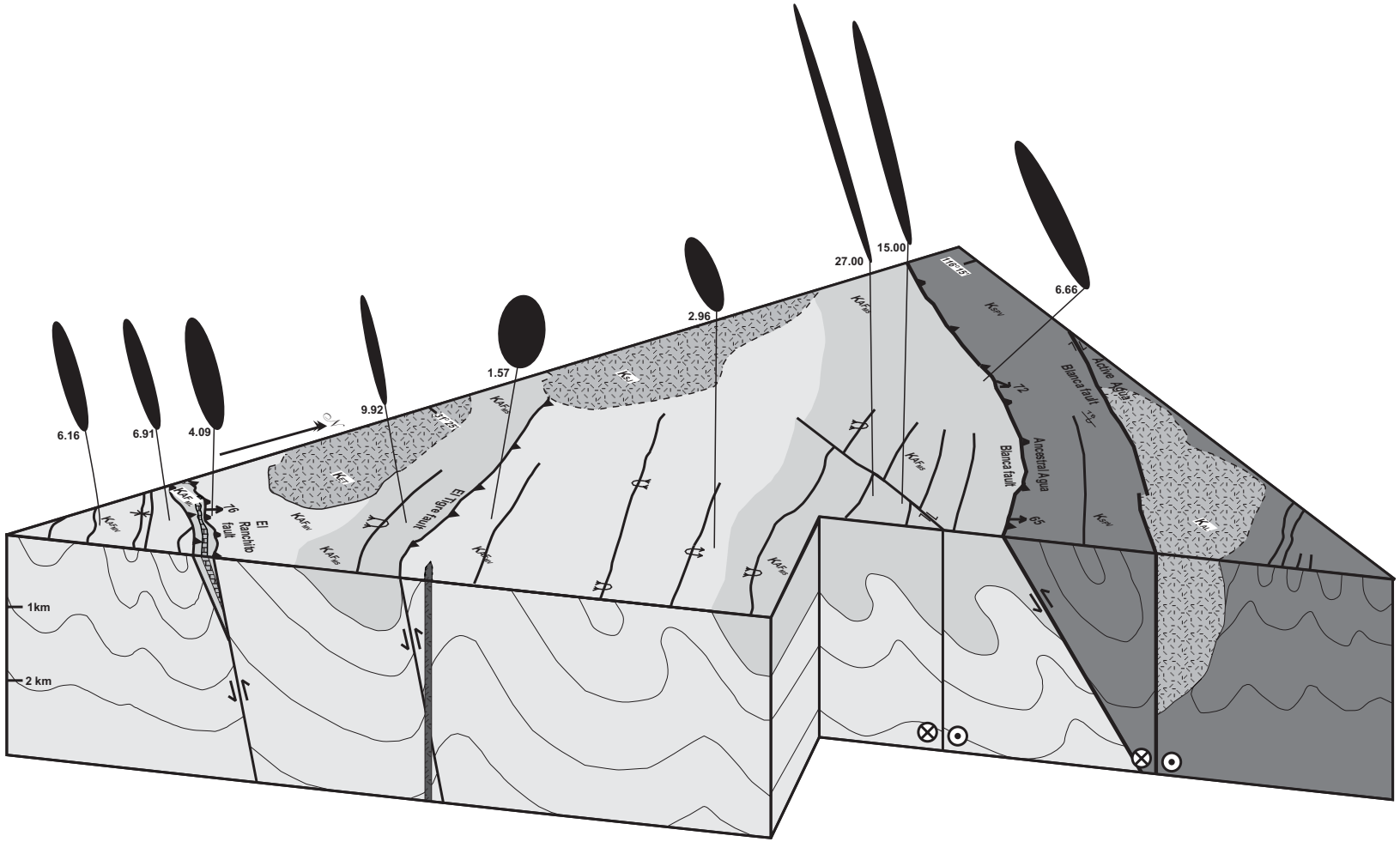

Figure 4.6. Block diagram cross section through the ancestral Agua Blanca fault study area. Black ovals represent the XZ plane of strain ellipses with the numerical ratio shown at the bottom of each ellipse. See Figure 4.2 for key to symbols and unit labels. No vertical exaggeration.

throughout the arc segment are typically large enough that regional deformation can be observed unaffected by emplacement-related deformation. The folds and thrust faults within the study area appear to have accommodated a large amount of shortening in this northern part of the Alisitos arc segment. Folds here are generally tight to isoclinal, with interlimb angles decreasing toward the aABF. They typically have one overturned limb with axial surfaces dipping steeply (>70°) to the northeast. These folds, however, possess hinges that plunge only slightly (<20°), even for examples within a few kilometers of the aABF.

The aABF is a mylonitic shear zone, oriented N72°W 72° NE, and located between two and three kilometers south of the active ABF along the south side of the Valle Agua Blanca. Exposure of the structure is limited to two locations in the study area, immediately northwest of the Arce pluton (K_A), which truncates the shear zone, and another approximately five kilometers further northwest. The shear zone is nearly 100 m wide in the former exposure and at least 50 m wide in the latter. Two well developed foliations are preserved in the shear zone, the older foliation, which is continuous, parallels the strike and dip of the zone and the younger, a spaced crenulation foliation, overprints the former foliation and is oriented N46W dipping 65° NE. Locally, the primary foliation is folded and the crenulation foliation is axial planar to these folds (Fig. 4.7a). Strain within the shear zone is immeasurably large as all original depositional features have been obliterated (Fig. 4.7b).

Figure 4.7. a. Closeup photo of the ancestral Agua Blanca fault showing primary foliation being folded. Photo looking southeast. b. Photomicrograph of a sample from the ancestral Agua Blanca fault shear zone showing both the continuous, primary foliation and the crenulating secondary foliation. c. Photo of the El Ranchito fault from an exposure south of the El Trigo pluton (Fig. 4.2). Photo is looking northwest (taken by K. Burmeister, 2003). d. Photo of a bedding contact along the western margin of the Balbuena pluton. Photo and the strike of bedding are to the northeast.

A number of secondary faults or shear zones also cut the Alisitos Formation, each dips steeply (>65º) towards the northeast, subparallel to the aABF (Fig. 4.2). These faults typically cut the limbs of some of the folds throughout the area (Fig. 4.6). The secondary faults all exhibit brittle and ductile deformation with 5-10 cm thick gauge or meter-scale breccia zones along the fault contact and increasing fabric (strain) intensities with proximity to the faults, particularly the El Ranchito fault. Total offset on any one fault cannot be constrained at this time due to both the lack of piercing points across the faults and definitive correlations of volcanic or sedimentary units between different thrust sheets.

Two of the secondary faults that cut the Alisitos Formation appear to have figured significantly in the structural development of this area. The more northern of the two faults, here called the El Tigre fault, is inferred to exist based on the geometry of folds. It is believed to be located in an area approximately 2-3 km southwest of the Balbuena Pluton (K_{BP}), however direct observation of the structure has not yet been made. The second fault, here called the El Ranchito fault, is located between the San Vicente pluton and the El Tigre fault (Fig. 4.7c). The El Ranchito fault is exposed throughout the study area and is easily identified on aerial photos and satellite images. It is generally located within a few hundred meters of the prominent limestone unit (Figs. 4.2 and 4.3). An additional fault, present just south of the limestone, is considered to be subordinate to the El Ranchito with minimal inferred offsets though it has been identified in the same relative position in multiple locations.

Strain. In order to further characterize the distribution and intensity of deformation within the study area tectonic strains were measured in 26 samples. Sample collection

was focused on polymictic, lithic-rich volcaniclastics to avoid the inadvertent inclusion of measurements of pumice clasts, which tend to exhibit extreme post-depositional compactions (e.g., Chapter 5). The methods for measuring strains are discussed in the introduction to Appendix C. The samples used in this study were collected from a number of different localities within or near the various structures present in the map area. These localities include the hinges and limbs of folds, structural aureoles of intrusive bodies, from both hanging and footwalls of faults, and from areas very distant to any of these structures/deformation. Figure 4.4 shows the distribution of sample localities and Table 4.2 includes, not only the strain data from this study, but also all such data collected from all Peninsular Ranges samples (Griffith and Hoobs, 1993; Chavez-Cabello, 1998; Johnson et al., 1999b; Schmidt, 2000).

The strains measured from samples collected in the aABF area exhibit a range in intensity with the largest gradients associated with large shear zones and pluton aureoles. The intensities range from 0.08 (4.4% shortening in the z-direction) to >1.6 (>80% shortening in the z-direction). In general, the shapes of the strain ellipsoids calculated from these samples exhibit a range from plane strain to oblate with only those with the smallest intensities exhibiting prolate shapes (Fig. 4.8).

While strain intensity does appear to exhibit an overall increase northeast toward the aABF the distribution of high strain intensity is not related solely to that structure. Figure 4.8 is a modified Flinn plot showing all strains calculated from this study area with those from samples collected within the structural aureoles of intrusive bodies differentiated from those collected from localities between these bodies. This plot shows that samples collected from pluton aureoles overlap with those proximal to large shear zones.

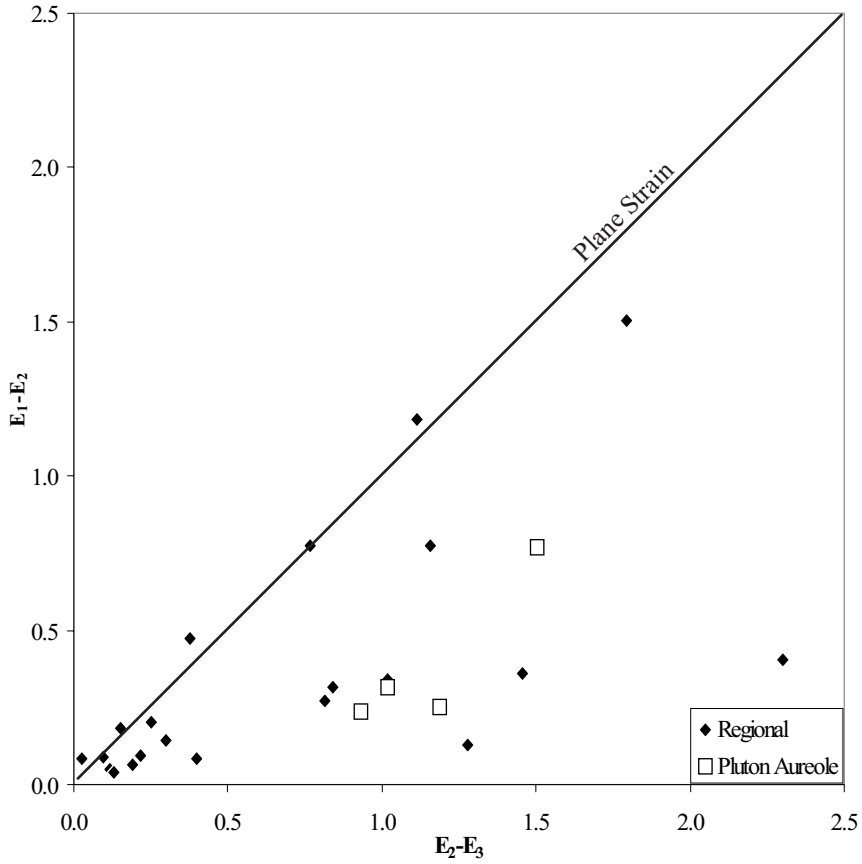

Fig. 4.8. Modified Flinn diagram of ancestral Agua Blanca fault strain data.

Table 4.2. Strain data collected from volcaniclastics throughout the Alisitos arc segment. Elongations are apparent constant volume extensions assume that the final axial ratios (X,Y,Z) formed by constant volume strain of an initially perfectly uniform population of markers with initial axial lengths equal to L_0. Natural strains are the natural logarithms of the ratio for each axial length to the initial length. Strain Magnitude is equal to $1/3[(E_1-E_2)^2 + (E_2-E_3)^2 + (E_3-E_1)^2]^{1/2}$ where E_1, E_2, and E_3 are the principle natural strains. Symmetry is equivalent to the Lodes Parameter where negative numbers = prolate shapes, 0.0 = plane strain, and positive numbers = oblate shapes. PHW samples are from the ancestral Agua Blanca fault study area (Fig. 4.1). PWS samples are from a study area south of the Agua Blanca fault ~40 km to the northwest of the ancestral Agua Blanca fault study area. BC and Chavez samples are from the northern Sierra San Pedro Mártir study area (Johnson et al., 1999b; Chavez, 1998). Griffith are from the Sierra Calamajue (Griffith and Hoobs, 1993). SP samples are from the southern Sierra San Pedro Mártir study area (Schmidt, 2001).

	Lengths				Elongations			Natural Strains			Strain	Lodes
Sample	X	Y	Z	Lo	X	Y	Z	X	Y	Z	Intensity	Parameter
PHW 2/24/01-A	1.29	1.21	1.00	1.16	11.29	4.28	-13.84	0.11	0.04	-0.15	0.19	0.49
PHW 2/24/01-B1	1.12	1.03	1.00	1.05	6.67	-1.94	-4.40	0.06	-0.02	-0.05	0.08	-0.54
PHW 2/24/01-B2	1.21	1.10	1.00	1.10	9.78	0.20	-9.09	0.09	0.00	-0.10	0.13	0.03
PHW 2/24/01-B3	1.62	1.49	1.00	1.34	20.63	11.13	-25.41	0.19	0.11	-0.29	0.36	0.66
PHW 2/24/01-B4	1.39	1.16	1.00	1.17	18.62	-1.01	-14.84	0.17	-0.01	-0.16	0.24	-0.09
PHW 2/24/01-B6	1.19	1.13	1.00	1.10	7.62	2.28	-9.16	0.07	0.02	-0.10	0.12	0.40
PHW 2/24/01-C	1.36	1.24	1.00	1.19	14.33	4.26	-16.10	0.13	0.04	-0.18	0.23	0.40
PHW 2/24/01-C1	1.18	1.14	1.00	1.10	7.01	3.07	-9.33	0.07	0.03	-0.10	0.12	0.55
PHW 5/17/01-P	1.57	1.29	1.00	1.27	24.40	1.71	-20.97	0.22	0.02	-0.24	0.32	0.00
PHW 5/21/00-C	2.30	1.44	1.00	1.49	54.39	-3.59	-32.82	0.43	-0.04	-0.40	0.59	-0.33
PHW 5/26/00-C	6.91	3.18	1.00	2.80	146.68	13.56	-64.30	0.90	0.13	-1.03	1.38	-0.26
PHW 5/7/01-J	3.80	2.77	1.00	2.19	73.39	26.39	-54.37	0.55	0.23	-0.78	0.57	0.26
PHW 5/9/00-C	6.66	4.14	1.00	3.02	120.46	37.05	-66.90	0.79	0.32	-1.11	1.40	0.11
PHW 6/13/00-E	4.68	2.15	1.00	2.16	116.65	-0.31	-53.70	0.77	0.00	-0.77	1.09	-0.37
PHW 6/13/00-F	9.92	3.04	1.00	3.11	218.61	-2.29	-67.88	1.16	-0.02	-1.14	1.62	-0.54
PHW 6/22/00-B	2.34	1.46	1.00	1.50	55.55	-3.25	-33.55	0.44	-0.03	-0.41	0.60	-0.32
PHW 6/22/00-M	6.16	4.30	1.00	2.98	106.68	44.15	-66.44	0.73	0.37	-1.09	1.36	0.28
PHW 6/24/01-J	3.18	2.32	1.00	1.95	63.43	19.09	-48.62	0.49	0.17	-0.67	0.85	0.21
PHW 6/25/01-G	15.00	10.00	1.00	5.31	182.31	88.21	-81.18	1.04	0.63	-1.67	1.19	0.29
PHW 6/25/01-H	27.00	6.00	1.00	5.45	395.29	10.06	-81.66	1.60	0.10	-1.70	1.35	-0.62
PHW 6/5/01-A	4.20	3.27	1.00	2.40	75.31	36.66	-58.26	0.56	0.31	-0.87	1.08	0.42
PHW 6/6/01-H	3.21	2.54	1.00	2.01	59.64	26.04	-50.30	0.47	0.23	-0.70	0.87	0.39
PHW 6/6/01-N	2.96	2.26	1.00	1.88	57.08	19.84	-46.88	0.45	0.18	-0.63	0.80	0.28
PHW 6/7/00-C	4.09	3.59	1.00	2.45	67.05	46.68	-59.19	0.51	0.38	-0.90	1.10	0.68
PHW 6/9/00-D	1.55	1.35	1.00	1.28	21.30	5.34	-21.74	0.19	0.05	-0.25	0.32	0.26
PHW 6/9/00-I	3.88	2.77	1.00	2.21	75.91	25.42	-54.67	0.56	0.23	-0.79	1.00	0.23
PHW 7/6/01-T	9.68	4.49	1.00	3.52	175.30	27.68	-71.55	1.01	0.24	-1.26	1.63	-0.20
PWS 1-9-E	1.31	1.16	1.00	1.15	14.14	0.85	-13.13	0.13	0.01	-0.14	0.19	0.03
PWS 2-24-E	1.54	1.38	1.00	1.29	20.08	7.09	-22.23	0.18	0.07	-0.25	0.32	0.39
PWS 2-24-D	1.56	1.41	1.00	1.30	20.12	8.19	-23.05	0.18	0.08	-0.26	0.33	0.45
PWS 2-24-B	1.65	1.26	1.00	1.28	29.33	-1.41	-21.57	0.26	-0.01	-0.24	0.35	-0.21
PWS 2-23-C	1.63	1.44	1.00	1.33	22.67	8.38	-24.79	0.20	0.08	-0.28	0.36	0.40
PWS 1-10-I	1.14	1.06	1.00	1.06	7.00	-0.52	-6.06	0.07	-0.01	-0.06	0.09	-0.15
PWS 9-23-H	1.54	1.38	1.00	1.29	19.83	7.31	-22.24	0.18	0.07	-0.25	0.32	0.40

Table 4.2 Continued

	Lengths				Elongations			Natural Strains			Strain	Lodes
Sample	**X**	**Y**	**Z**	**Lo**	**X**	**Y**	**Z**	**X**	**Y**	**Z**	**Intensity**	**Parameter**
BC 207	2.19	1.90	1.00	1.61	36.16	18.13	-37.83	0.31	0.17	-0.48	0.59	0.51
BC 208	3.56	2.96	1.00	2.19	62.38	35.01	-54.39	0.48	0.30	-0.78	0.97	0.53
BC 209	7.12	3.53	1.00	2.93	143.07	20.51	-65.86	0.89	0.19	-1.07	1.41	-0.17
BC 220	1.46	1.26	1.00	1.23	19.15	2.83	-18.39	0.18	0.03	-0.20	0.27	0.13
BC 221	1.27	1.12	1.00	1.12	13.03	-0.59	-11.00	0.12	-0.01	-0.12	0.17	-0.13
BC 387	2.33	2.00	1.00	1.67	39.50	19.74	-40.13	0.33	0.18	-0.51	0.64	0.50
BC 413	1.48	1.11	1.00	1.18	25.43	-5.93	-15.25	0.23	-0.06	-0.17	0.29	-0.54
BC 472	6.48	6.33	1.00	3.45	87.90	83.55	-71.00	0.63	0.61	-1.24	1.52	0.95
BC 506A	4.45	2.63	1.00	2.27	96.00	15.84	-55.96	0.67	0.15	-0.82	0.92	-0.06
Chavez PP-1	1.34	1.26	1.00	1.19	12.38	5.89	-15.96	0.12	0.06	-0.17	0.13	0.54
Chavez PP-2	3.77	2.42	1.00	2.09	80.24	15.92	-52.14	0.59	0.15	-0.74	0.55	0.03
Chavez PP-3	4.44	3.79	1.00	2.56	73.38	47.79	-60.97	0.55	0.39	-0.94	0.67	0.62
Chavez SPM-1	14.07	4.61	1.00	4.02	250.24	14.72	-75.11	1.25	0.14	-1.39	1.08	-0.45
Griffith-154	5.24	3.07	1.00	2.52	107.63	21.50	-60.36	0.73	0.19	-0.93	0.69	-0.03
Griffith-158	5.32	2.67	1.00	2.42	119.58	10.29	-58.71	0.79	0.10	-0.88	0.69	-0.23
Griffith-158A	7.08	2.98	1.00	2.76	156.31	7.81	-63.81	0.94	0.08	-1.02	0.80	-0.35
SP 100	6.20	2.81	1.00	2.59	139.15	8.32	-61.40	0.87	0.08	-0.95	1.30	-0.30
SP 137-B	2.12	1.83	1.00	1.57	34.71	16.55	-36.31	0.30	0.15	-0.45	0.02	0.49
SP 548-B	4.51	2.73	1.00	2.31	95.32	18.14	-56.66	0.67	0.17	-0.84	1.01	-0.02
SP 801	6.35	3.75	1.00	2.88	120.60	30.38	-65.23	0.79	0.27	-1.06	1.18	0.03
SP 806	4.29	2.86	1.00	2.31	85.77	24.16	-56.65	0.62	0.22	-0.84	1.02	0.13
SP 828	4.44	3.94	1.00	2.60	70.97	51.82	-61.48	0.54	0.42	-0.95	1.00	0.71
SP 902	2.83	2.02	1.00	1.79	58.52	12.75	-44.05	0.46	0.12	-0.58	0.75	0.11
SP 99	6.87	1.53	1.00	2.19	213.45	-30.07	-54.38	1.14	-0.36	-0.78	1.82	-0.82

Figure 4.9a-c illustrates the heterogeneous character of strain throughout the study area with three different strain parameters (intensity, z-direction shortening, and Lodes parameter) plotted with respect to the sample location relative to the aABF. Also shown on this figure are the approximate locations of the El Tigre and El Ranchito faults. While a gradient in strain intensity/percent shortening, increasing toward the northeast (aABF), is present from ~7 km south of the fault, a second region of elevated strain is also present in both walls of the El Ranchito fault. In contrast, the area surrounding the El Tigre fault is characterized by relatively low strain intensities. Figure 4.9c, a plot of Lodes parameter for each sample relative to the distance from the aABF exhibits no consistent relationship between strain ellipsoid shape and proximity to any of the major faults in the study area.

Plutons. Several plutonic bodies intrude the fold and thrust belt throughout the study area. Structural aureoles, the region within which host rocks are deformed as a result of magma emplacement, generally range form less than a kilometer to no more than two kilometers wide. The largest structural aureole is that of the Balbuena pluton (K_{BP}) where host rock structures (including folds) to the northwest and southeast of the intrusion are deflected by as much as 70° away from regional trends (Figs. 4.2 and 4.7d). Other intrusions in the area exhibit much more discordant relationships to host rock structures, the Piedra Rodada (K_{PR}) and San Vicente (K_{SV}) plutons, for example, truncate structures without significant deflections.

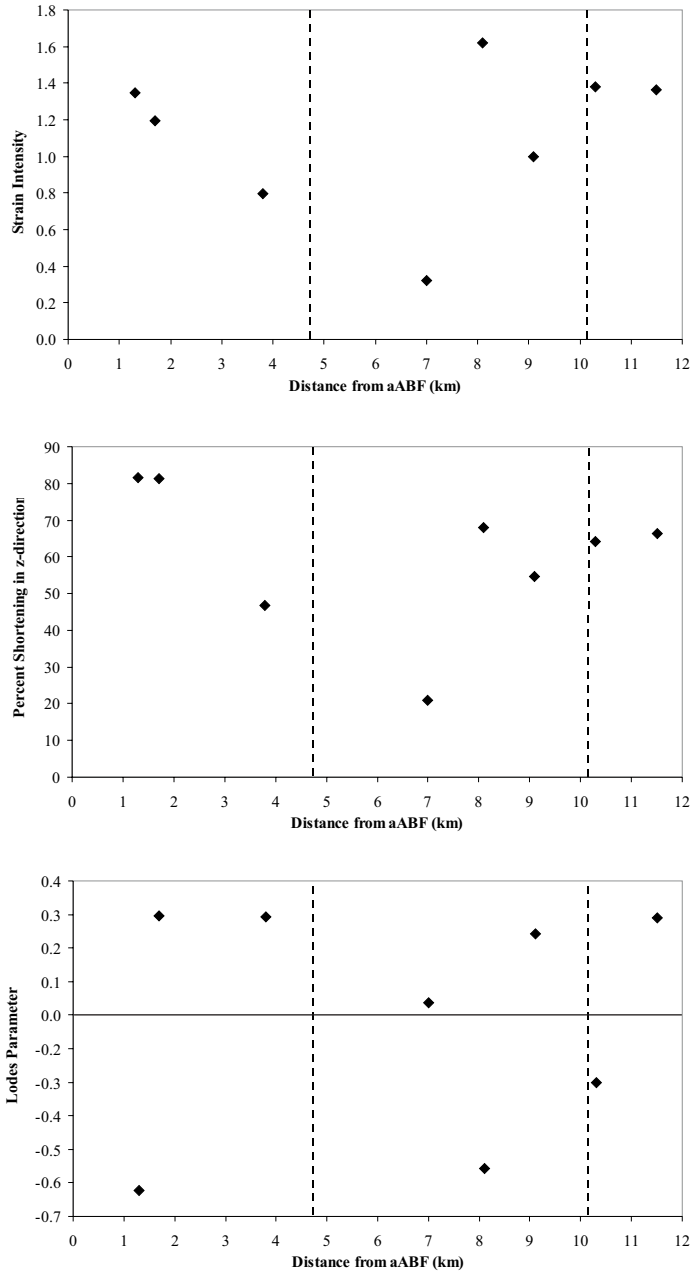

Fig. 4.9. Three plots of different aspects of strain at distances relative to the ancestral Agua Blanca fault.

Most plutons in the region are dominated by magmatic foliations and lineations that are only weakly developed. One exception to this is the Piedra Rodada pluton, the northeastern half of which is involved in aABF-related deformation (Fig. 4.2). The Piedra Rodada pluton exhibits a gradient in fabric type and intensity from moderately strong magmatic foliations and lineations (defined by both modal mineralogy and enclave shapes) along the southwestern margin to strong subsolidus foliations and lineations with a weakly to moderately developed S-C fabric along the northeastern margin (Fig. 4.10a-d).

The Arce pluton (K_A) also possess a close spatial relationship to the aABF but appears to intrude the structure without having been much affected by fault related deformation. The aABF is truncated along the northwest side of the Arce pluton (Fig. 4.10a) and fabrics within the pluton are oblique those in the surrounding host rocks. Furthermore, fabrics within the pluton are typically magmatic with only rare brittle shear fractures present.

Kinematics. A large number of reliable kinematic indicators, nearly all indicating the same sense of shear, are present throughout the field area. These include asymmetric clasts and folds (cm-km scale) in the country rocks, and asymmetric mafic enclaves and S-C fabrics in the subsolidusly deformed Piedra Rodada pluton (K_{PR}; Fig. 4.11a-d). Nearly all shear sense determinations from lineation parallel-foliation perpendicular sections indicated a northeast over southwest, reverse shear sense. Only three exception to this were observed in the study area; (1) within the structural aureole of some of the plutons, (2) along a small fault located just north of Rancho Sandoval (~2 km north of

Figure 4.10 a. Field photo of the Piedra Rodada, and Arce plutons with the ancestral Agua Blanca fault being truncated by the latter intrusion. b. Photomicrograph of a thin section of a sample from the Piedra Rodada pluton near its southwestern margin. Not the relatively large crystals with some slight undulose extinction in the biotite crystal at the center of the image. c. Field photo of a subsolidus fold in the Piedra Rodada pluton. Photo take looking northwest. d. Photomicrograph of a sample from the Piedra Rodada pluton near its northeastern margin. Note the dramatic grain size reduction relative to photo b in this figure.

Figure 4.11. a. Foliation normal-lineation parallel (as it is for all photos in this figure) field photo of a volcaniclastic unit south of the ancestral Agua Blanca fault. Asymmetries suggest northeast side (left) up. Photo is taken looking to the southeast. b. Photomicrograph of a boudinaged plagioclase phenocryst from a sample of the ancestral Agua Blanca fault shear zone. View is to the northwest and shear sense is northeast side up. c. Field photo of an asymmetric enclave within the Piedra Rodada pluton. Photo is taken looking to the northwest and the shear sense is northeast side up. d. Drag folds on the small fault southwest of the El Ranchito fault (Fig. 4.2). Photo taken looking northwest and the sense of shear indicated by the drag is northeast side up.

San Vicente), and (3) on the overturned limbs of some of the folds within ~3 km of the aABF. Shear sense indicators near all three major faults (aABF, El Tigre, and El Ranchito) unambiguously suggest northeast side up-reverse shear.

Asymmetries in clast shapes and folds observed in faces oriented normal to both foliations and lineations were identified in several exposures within ~5 km of the aABF. While these examples are not as well developed as those for lineation parallel sections they do exhibit a consistent sinistral shear sense. At greater distances from the aABF asymmetries in this plane are less commonly observed and do not always exhibit the same shear sense.

Geochemistry and geochronology

The geochemistry of igneous rocks throughout the Peninsular Ranges exhibit well established spatial and less well understood temporal variations. A moderately large geochemical data set for both volcanics and plutonic rocks indicates that the PRb is zoned laterally. Depending upon the level of detail a data set provides, the PRb has been subdivided into western, central, and eastern batholith-parallel zones (e.g., Gromet and Silver, 1987). The geochemical differences between western and eastern zones have commonly been interpreted to indicate that they were oceanic island and continental margin arcs, respectively (Gastil, 1983; Silver and Chappell, 1999). The central zone is transitional between them.

The temporal-spatial distribution of plutons throughout the Peninsular Ranges was once thought to have been explained by the juxtaposition of a static western arc (140-105 Ma) with a migrating eastern arc (105-80 Ma; Silver and Chappell, 1988). However, a

number of recent studies have demonstrated that magmatism was active in both western and eastern zones during the Early Cretaceous (e.g., Johnson et al., 1999a; Schmidt and Paterson, 2003) and that an earlier suite of plutons were emplaced within the central part of the range during the Late Jurassic (~165 Ma). Furthermore, the timing of magmatism within the western zone has been refined to range from ~127 to 103 Ma (Anderson, 1991; Herzig, 1991; Premo et al., 1998; Johnson et al., 1999a, 2003). A minor age discrepancy does appear to exist between the Santiago Peak and Alisitos arc segments as plutons and volcanics of the former segment range from 127 to 116 Ma while those of the latter range from 116 to 103 Ma. This observation, however, is based on a small number of age data and should be viewed with some caution until it is better constrained by more ages.

The interpretation that the western PRb (i.e., Santiago Peak and Alisitos arc segments) originated as an oceanic island arc persists though the petrology and geochemistry of the western zone plutons/volcanics exhibit several differences with those of active island arc systems (e.g., Tate et al., 1999). For example, average petrologic compositions of western zone intrusives and volcanics from both arc segments are commonly more silicic (>60 wt% SiO_2) and are characterized by greater light Rare Earth Element (LREE) enrichments than typical of island arc systems such as the Tonga arc (Bourdon et al., 1999). Tate et al. (1999) and Tate and Johnson (2000) address this issue in their geochemical studies of the intrusive bodies in the northern Sierra San Pedro Mártir which fall into two age groups 114-115 Ma 108 to 103 Ma. Those of the older group intrude the western volcanics-dominated belt, while those of the younger group intrude the eastern volcaniclastics dominated belt. While plutons from both groups exhibit overlapping compositions for most major and many trace elements, there are

substantial differences between the two groups with respect to REE, Sr, and Y abundances. While western belt plutons exhibit La/Lu_{CN} (elements normalized to an average chondrite composition; McDonough and Sun, 1995) and Sr/Y <3, those of eastern belt plutons are greater than 12 and 90, respectively. Figure 4.12 graphically illustrates the differences in REE compositions between the two groups of plutons. The petrogenetic model proposed by Tate and Johnson (2000) to explain these observed differences calls upon the over thickening (>43 km) of an already thick (~28 km, Tate et al., 1999) arc crust as the result of collision of the Alisitos arc segment with the continental margin. By driving the source region for these melts to such depth garnet and amphibole become stable phases often remaining in the residuum after melting. These mineral phases tend to retain HREE relative to LREE thereby producing the strong LREE enrichment exhibited by the eastern belt pluton (Fig. 4.12).

Geochronology of ancestral Agua Blanca fault region. Zircons from six plutonic samples collected in a transect across the ancestral Agua Blanca fault (two from the Santiago Peak and four from the Alisitos) and analyzed to determine U/Pb crystallization ages (Fig. 4.4). The plutons sampled were, from north to south, the Santo Tomás (K_{ST}; sample PHW 5/29/01-B), Agua Blanca (K_{AB}; sample PHW 1/8/03-H), Piedra Rodada (K_{PR}; sample PHW 7/6/01-S), two phases of the Balbuena (K_{BP}: samples PHW 6/9/01-B and PHW 6/9/01-F), and the San Vicente pluton (K_{SV}; sample PHW 1/12/03-A). Between 20 and 25 zircon crystals were analyzed from each sample using an LA-MC-ICPMS at the University of Arizona under the direction of Dr. George Gehrels. Procedures for zircon separation and analyses, as well as the data are presented in Appendix A, Table A2a-f.

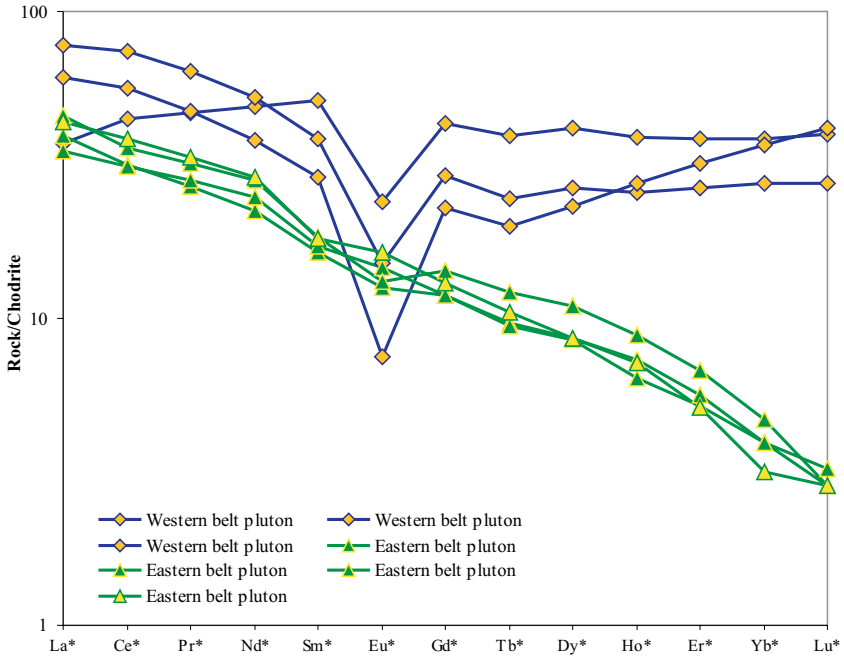

Fig. 4.12. Plot of chondrite normalized rare earth element abundances for plutons from the northern Sierra San Pedro Mártir (data from Tate and Johnson, 2000).

The two plutons intruding the Santiago Peak Volcanics, samples PHW 5/29/01-B and PHW 1/8/03-H, yielded the oldest crystallization ages of the six analyzed at115.0 $\pm$ 3.9 Ma and 116.5 $\pm$ 3.8 Ma, respectively (Fig. 4.13a-b). Those intruding the Alisitos arc segment yield ages ranging from 108.6 $\pm$ 3.96 Ma to 105.0 $\pm$ 3.4 Ma (Fig. 4.13c-f). Interestingly, the ages determined in this study provide further support for an apparent age gap in magmatism between the two arc segments. Only one obviously xenocrystic zircon was analyzed from any of the plutons. This crystal, from sample PHW 5/29/01-B, yielded an age of 148.8 $\pm$ 3.9 Ma.

Reconnaissance geochemistry. In addition to the geochronology, a suite of plutonic samples were analyzed for geochemical compositions. All samples with U/Pb zircon analyses discussed above, were analyzed with the exception of sample PHW 7/6/01-S from the Piedra Rodada pluton. An alternate sample, PHW 7/1/01-F, from the same phase of the same intrusion but from a location approximately two kilometers northwest was analyzed instead (Fig. 4.4). An additional sample from the Arce pluton (K_A; sample PHW 7/3/01-J) was also analyzed. Whole rock, major and trace elemental compositions were determined by Actlabs, a commercial analytical facility, using lithium metaborate/tetraborate fusion ICP. Analysis of the radiogenic isotopic compositions of Rb-Sr, and Sm-Nd were also completed on each of these samples. Mass spectrometric analyses were completed using two VG Sector multicollector instruments (VG54 and VG354) fitted with adjustable 10^{11} Ω Faraday collectors and Daly photomultipliers (Patchett and Ruiz, 1987). Sample preparations and analytical procedures are described in Appendix A.

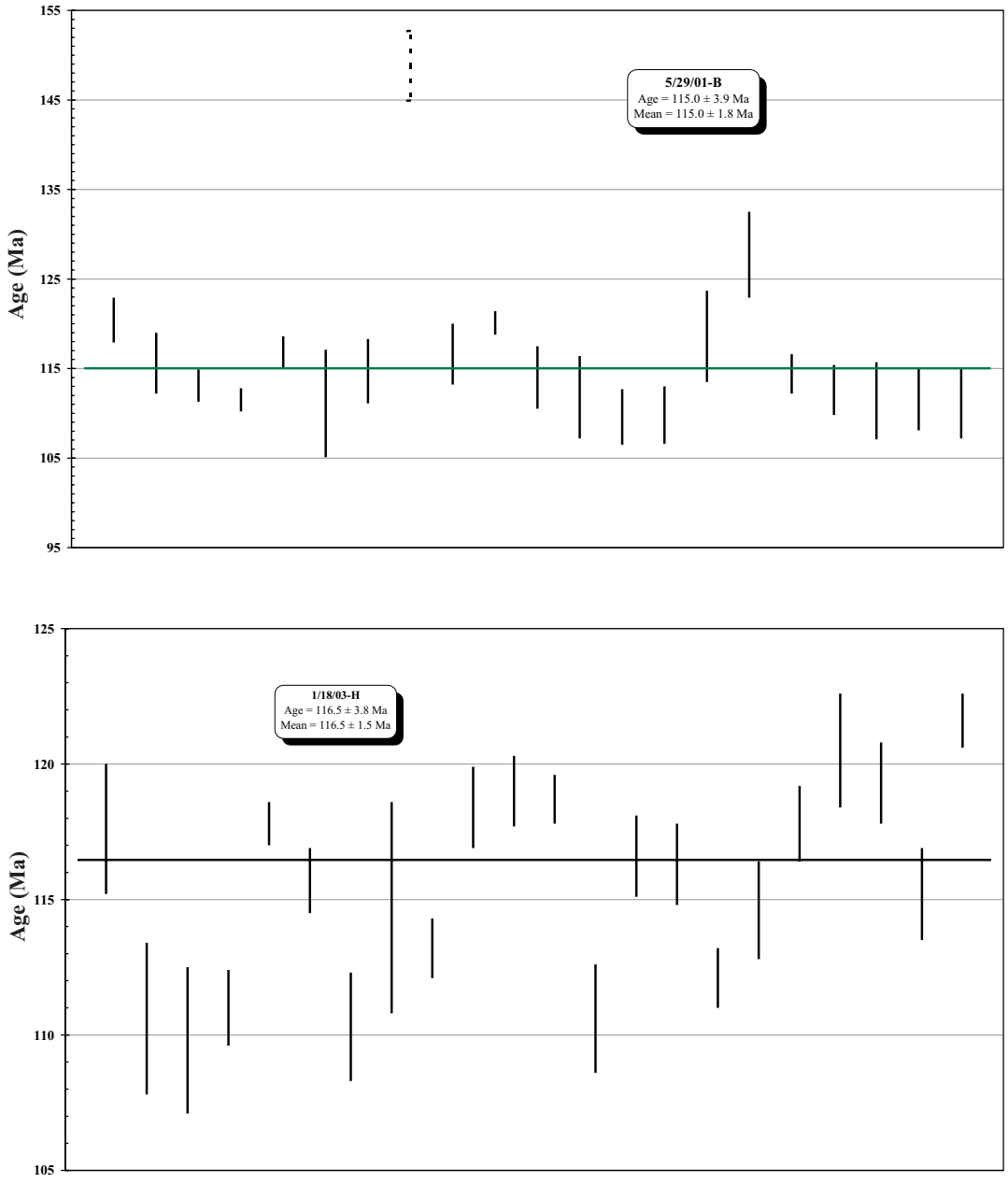

Figure 4.13. Plots of all U/Pb zircon age data collected from the six plutons analyzed in this study.

Figure 4.13. Continued

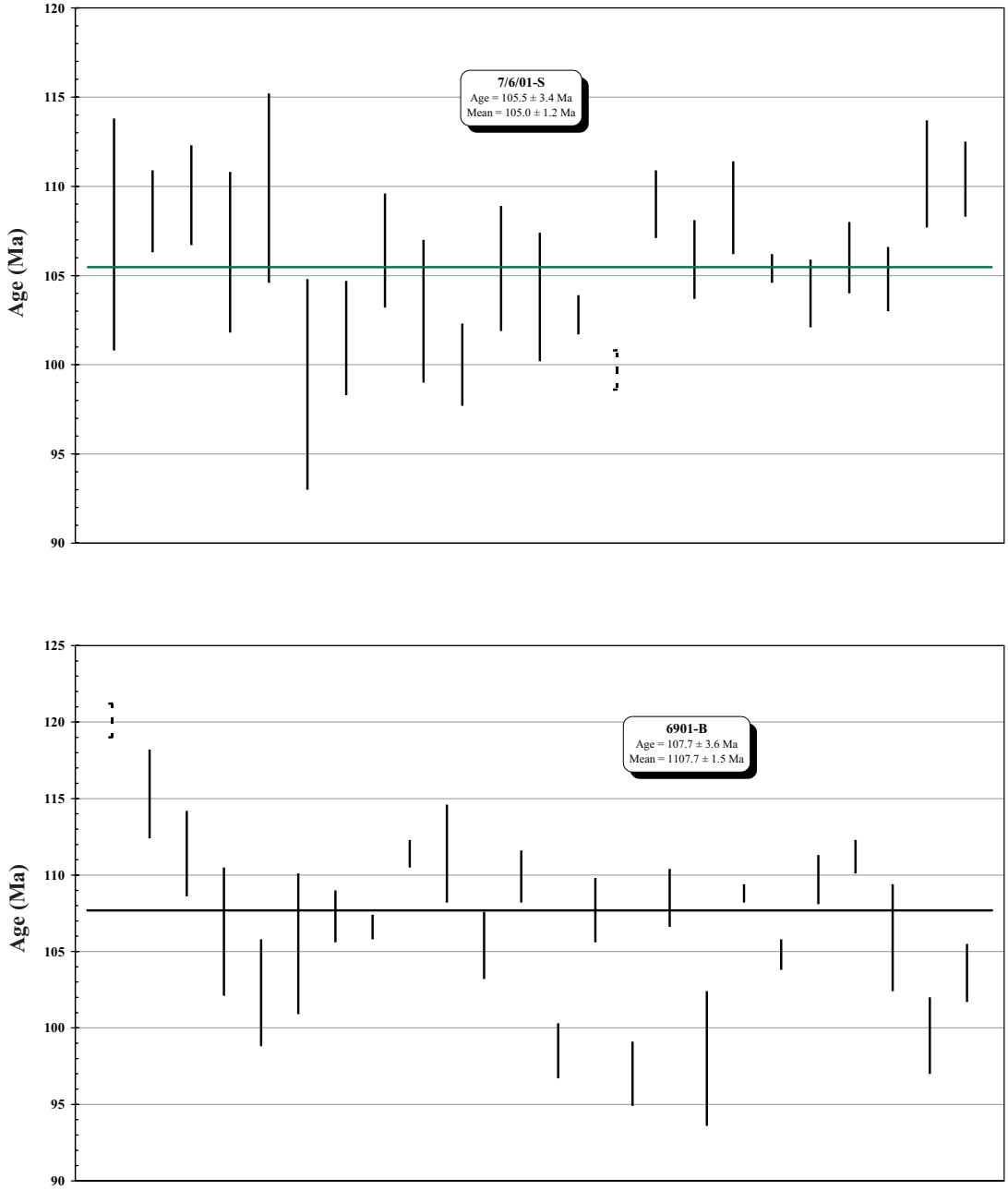

Figure 4.13. Continued

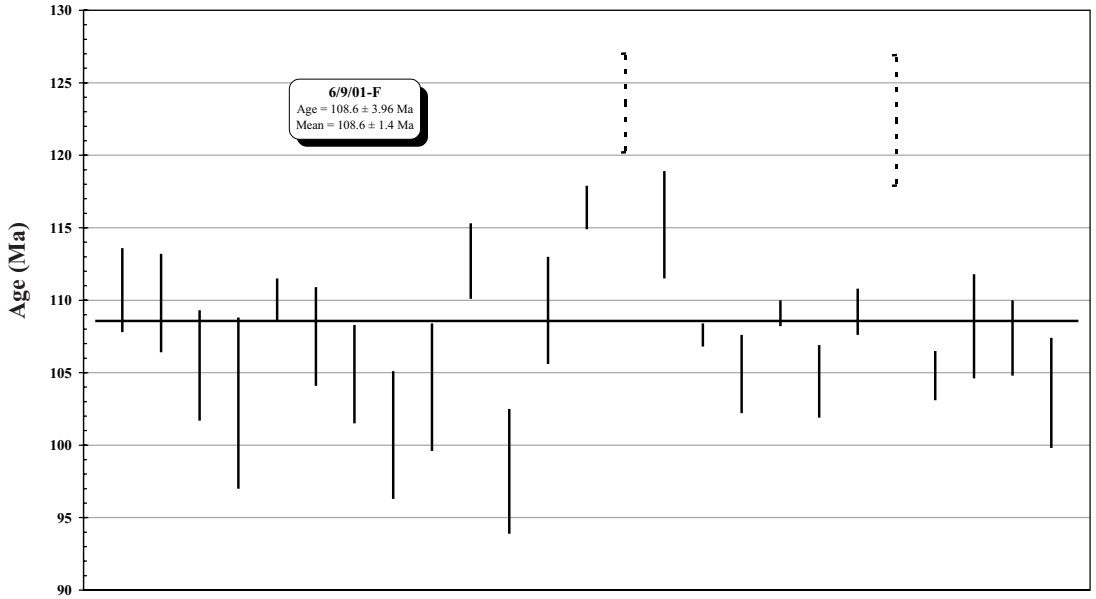

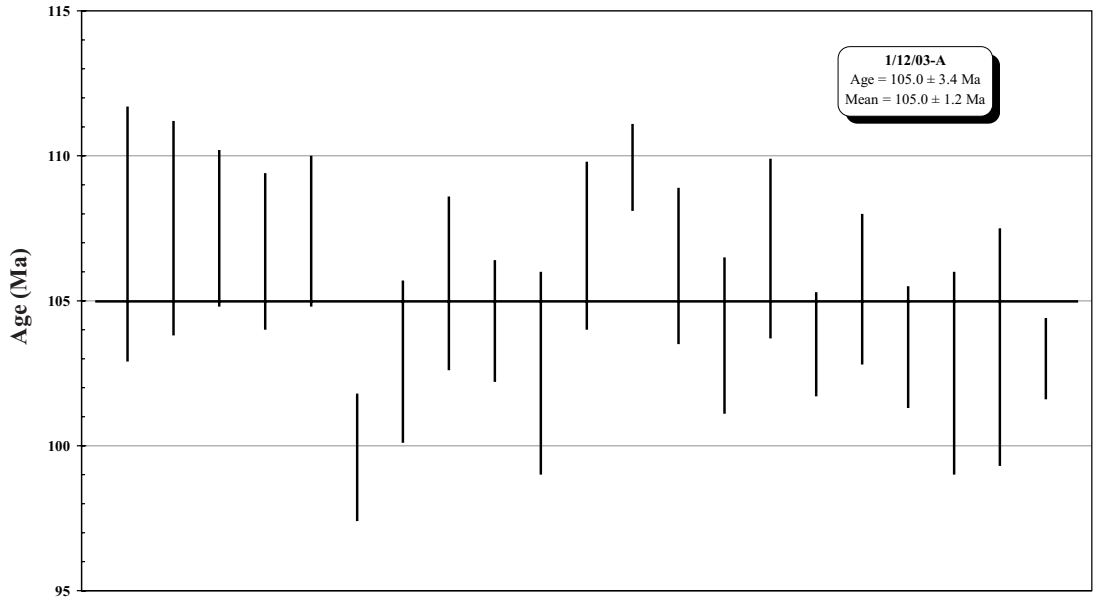

The whole rock and isotopic results of these analyses are given in Tables 4.3 and 4.4, respectively. All plutons analyzed in this study are tonalites with compositions that overlap with those of tonalites intruding the western belt in the Sierra San Pedro Mártir study area (Tate et al., 1999). Silica contents range from 58 to 74 wt% and all samples are strongly peraluminous (A/CNK >1.5). Magnesium numbers (MgO wt%/ MgO + Fe_2O_3 wt%) exhibit a relatively broad range from 0.06 to 0.29 that is inversely correlated with silica contents. Light rare earth elements exhibit a moderate enrichment with La/Lu_{CN} ratios ranging from 1.1 to 4.6 (Fig. 4.14). Similarly, Sr/Y ratios range from 1.0 to 27.2.

Table 4.3. Whole rock geochemical data for plutonic samples collected from the ancestral Agua Blanca fault study area.

Samples	5/29/01-B	1/8/03-H	7/3/01-J	7/1/01-F	6/9/01-B	6/9/01-F	1/12/03-A
Description	Santo Tomas Pluton	Agua Blanca Pluton	Arce Pluton	Piedra Rodado	Balbuena Phase II	Phase III Balbuena	SV Pluton
SiO_2	69.61	74.01	71.55	62.89	72.99	58.16	62.69
TiO_2	0.520	0.215	0.431	0.679	0.317	1.067	0.530
Al_2O_3	13.85	12.48	13.62	15.42	13.85	16.59	16.74
FeO	ND	ND	ND	ND	ND	ND	ND
Fe_2O_3	4.20	2.61	2.69	6.07	2.87	8.39	5.64
MnO	0.064	0.101	0.055	0.110	0.081	0.173	0.112
MgO	0.87	0.17	0.62	2.30	0.52	3.12	2.26
CaO	2.95	0.90	2.56	4.68	2.50	6.13	5.57
Na2O	4.37	4.42	4.17	3.51	4.64	3.60	3.70
K_2O	1.37	2.84	2.64	1.88	1.65	0.72	0.76
P_2O_5	0.13	0.04	0.09	0.14	0.08	0.21	0.13
LOI	0.55	0.97	0.73	1.02	0.72	0.87	1.43
TOTAL	98.50	98.76	99.15	98.70	100.22	99.02	99.55
Trace Elements (ppm)							
Ba	426	756	715	503	448	267	278
Rb	34	48	30	57	42	17	18
Sr	209	87	177	209	155	295	327
Y	24	86	52	33	24	29	12
Zr	242	232	274	159	161	114	65
Nb	5	7	9	5	5	5	3
Th	7.8	7.3	7.0	11.7	4.4	2.5	2.0
Pb	11	17	13	7	8	6	7
Ga	17	19	17	17	15	18	19
V	37	25	20	100	18	144	89
Hf	6.6	7.0	8.0	5.2	4.8	3.5	2.2
Cs	1.8	0.5	0.5	1.1	1.7	0.8	0.7
Sc	7	9	15	7	19	9	6
Ta	0.4	0.6	0.8	0.4	0.4	0.3	0.2
U	1.9	2.2	2.3	1.8	1.2	0.8	0.6
Sn	2	3	4	3	6	2	4
Be	1	2	1	2	1	BDL	2
Zn	88	137	80	86	71	93	79
Ge	1	2	2	1	2	BDL	1
Tm	0.41	1.43	0.80	0.56	0.41	0.47	0.20
W	7	17	11	5	6	3	14
Tl	0.3	0.4	0.2	0.3	0.3	0.1	BDL

Table 4.3. Continued

Samples Description	5/29/01-B Santo Tomas Pluton	1/8/03-H Agua Blanca Pluton	7/3/01-J Arce Pluton	7/1/01-F Piedra Rodado	6/9/01-B Balbuena Phase II	6/9/01-F Phase III Balbuena	1/12/03-A SV Pluton
Rare Earth Elements (ppm)							
La	17.9	14.4	17.6	23.9	15.0	15.2	7.4
Ce	36.6	34.1	55.6	48.1	31.2	32.7	15.6
Pr	4.16	5.73	7.01	5.43	3.80	3.97	1.94
Nd	17.1	30.5	28.8	22.2	16.4	17.3	8.4
Sm	3.9	9.7	6.9	5.3	3.8	4.6	2.2
Eu	1.62	1.11	1.50	1.25	1.01	1.54	0.79
Gd	3.8	11.4	7.0	5.2	3.5	4.8	2.1
Tb	0.7	2.2	1.3	1.0	0.7	0.9	0.4
Dy	4.0	13.9	8.2	5.6	4.0	5.2	2.1
Ho	0.8	3.0	1.8	1.2	0.8	1.0	0.4
Er	2.6	9.1	5.3	3.6	2.5	3.1	1.2
Yb	2.9	9.5	5.4	3.6	2.9	3.0	1.3
Lu	0.46	1.41	0.84	0.54	0.45	0.44	0.20

Table 4.4. Radiogenic isotopic data for plutonic samples collected from the ancestral Agua Blanca fault study area.

Samples	5/29/01-B	1/8/03-H	7/3/01-J	7/1/01-F	6/9/01-B	6/9/01-F	1/12/03-A
Description	Santo Tomas Pluton	Agua Blanca Pluton	Arce Pluton	Piedra Rodada	Balbuena Phase II	Phase III Balbuena	SV Pluton
Sm $_{(ppm)}$	2.57	3.05	5.13	3.99	2.91	2.86	1.56
Nd $_{(ppm)}$	11.38	12.35	23.36	18.41	12.45	12.61	6.61
Sm/Nd	0.226	0.228	0.219	0.217	0.233	0.226	0.235
$^{147}Sm/^{144}Nd$	0.1365	0.1387	0.1327	0.1311	0.1412	0.1371	0.1423
$^{143}Nd/^{144}Nd_{(0)}$	0.5129	0.5129	0.5129	0.5129	0.5129	0.5129	0.5129
$\varepsilon_{Nd\ (0)}$	5.26	5.01	4.93	4.5	5.47	5.3	5.31
$^{143}Nd/^{144}Nd_{(100)}$	0.5128	0.5128	0.5128	0.5128	0.5128	0.5128	0.5128
$\varepsilon_{Nd\ (100)}$	6.03	6	5.75	5.34	6.17	6.06	6
Rb $_{(ppm)}$	33.01	45.88	28.37	43.83	16.04	40.93	16.53
Sr $_{(ppm)}$	207.3	82.6	168.1	205.7	278.9	152.3	310.8
87Rb/86Sr	0.4604	1.6062	0.4881	0.6163	0.1664	0.7775	0.1538
$^{87}Sr/^{86}Sr_{(0)}$	0.7040	0.7059	0.7040	0.7046	0.7035	0.7043	0.7036
$^{87}Sr/^{86}Sr_{(100)}$	0.7034	0.7035	0.7033	0.7037	0.7033	0.7032	0.7034
$^{206}Pb/^{238}U_{(age\ Ma)}$	115 $\pm$ 3.9	116 $\pm$ 3.8		105.5 $\pm$ 3.4	107.7 $\pm$ 3.6	108.6 ± 3.96	105.0 ± 3.4

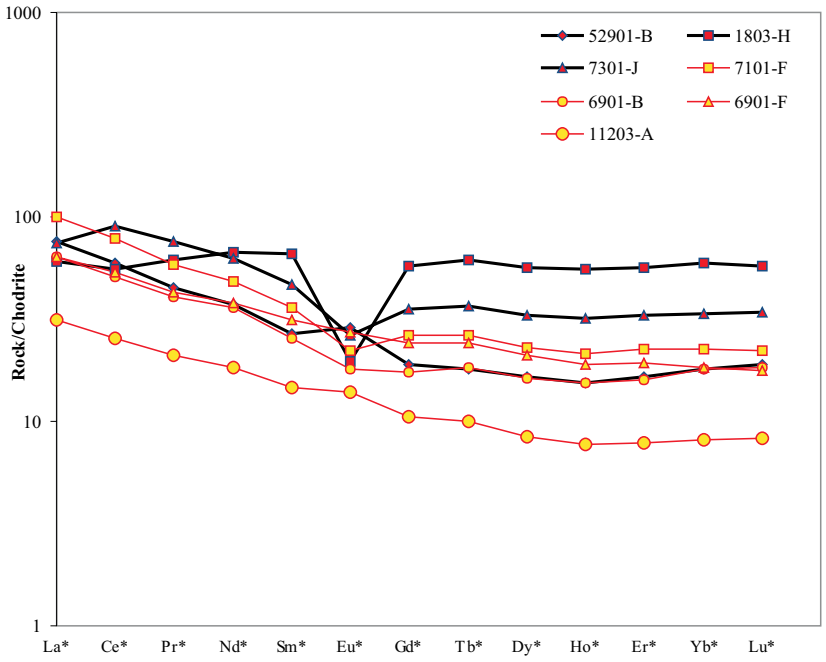

Figure 4.14. Plot of chondrite normalized rare earth element abundances for plutons from the ancestral Agua Blanca fault study area.

Discussion

The observations of the aABF region of the western Peninsular Ranges described above provide significant constraint to the Early Cretaceous depositional, structural, and magmatic evolution of this area, and the western Peninsular Ranges as a whole. In this section the implications for each of the above data sets is discussed. Following, the working tectonic model (i.e., that presented by Wetmore et al., In press) will be revisited.

Is there an interarc basin?

As originally noted by Gastil et al. (1975), the ABF marks a major break in the petrology of the stratigraphy of the western zone. This is certainly consistent with the observations from the study area present here. Immediately south of the aABF the Alisitos Formation is dominated by the shales and volcaniclastic sandstones of the top of the upper section of the stratigraphic column of Figure 4.3. North of the fault the Santiago Peak Volcanics are composed of less than ~1% of similar such rock types supporting the conclusions of many others that these strata were erupted and deposited in a predominantly subarial environment. This implies that the Santiago Peak arc segment to the north was emergent prior to and perhaps during the proposed accretion of the Alisitos arc segment.

The interarc basin corresponding to the volcaniclastics-dominated eastern belt described for the Alisitos arc segment in both the Sierra San Pedro Mártir (Johnson et al., 1999a) and to the south of the near Punta China ABF (Suarez-Vidal, 1986) is less well defined in this study area. This is due to the significant proportion of primary (i.e., not reworked) volcanics throughout the region but specifically for the middle and upper

sections of the stratigraphic column presented in Figure 4.3. In part, this may simply reflect a greater proximity to eruptive centers for this study area relative to that of the other areas in which the basin is more easily identified by stratigraphy. This interpretation seems consistent with the observation that the upper two sections of the strata column do fine upwards into shales. Furthermore, if the correlation of the two uppermost sections in Figure 4.3 with the eastern belt elsewhere in the Alisitos arc segment is valid it stand to reason that the El Ranchito fault may also be the on-strike continuation of the Rosarito fault of the Sierra San Pedro Mártir study areas.

Detrital zircon populations indicate that continentally-derived sediments were being deposited on the Alisitos arc segment very late in its evolution. The crystals with the youngest ages suggest a maximum age of deposition for both samples of ~100 Ma. Given the observations from both the Sierra San Pedro Mártir area (Johnson et al., 1999a; Schmidt and Paterson, 2003) and here (discussed below) that deformation of the Alisitos arc segment predates at least 108 Ma, deposition of these sediments, which are also deformed, must post-date much of the accretion-related deformation. The presence of zircons yielding Paleozoic and Precambrian ages in these samples clearly implies a source other than the arc itself, plutonics and volcanics of which have not produced such ages. Similarly, given the proportion of the older ages in sample PHW 5/19/00-A suggests that the Santiago Peak Volcanics and associated plutons are also unlikely sources. The Bedford Canyon Complex or perhaps North American miogeoclinal/slope basin strata present in the area near San Felipe (Gastil, 1993; Figure 4.1) represent the most likely local sources for these zircons. It should be noted, however, that a single age from a volcaniclastic unit from the eastern belt in the northern Sierra San Pedro Mártir

yielded a U/Pb zircon age of 114.8 ± 1.5 Ma without observed inheritance (Johnson et al., 2003). This seems to indicate that early deposition in the volcaniclastics dominated basin along the eastern side of the Alisitos arc segment was without a continental contribution.

Deformation of the northern Alisitos arc segment.

The fold and thrust belt associated with the northeastern margin of the Alisitos arc segment is dissimilar to perhaps more well know examples such as the Idaho-Wyoming fold and thrust belt (Armstrong and Oriel, 1965) in that the majority of contraction is taken up by folding and not large displacement, low angle thrust faults. Tight and isoclinal folds pervade the study area and the secondary faults do not juxtapose rocks of dramatically different metamorphic grade suggesting their total thrust offset is probably less than a few kilometers. Small offsets on these faults is all consistent with the correlation of the middle and upper sections of the stratigraphic column (Fig. 4.3) juxtaposed by the El Tigre fault.

While a significant amount of shortening within the aABF study area is evident it appears to be somewhat less than that observed in the Sierra San Pedro Mártir and the Sierra Calamajue areas. The fold and thrust belt in this study area is 15 km wide measuring from the aABF to the middle of the San Vicente pluton (the Alisitos Formation dips homoclinally westward southwest of the pluton). Tight and isoclinally folded strata are observed as much as 25 km away from the Main Mártir thrust in the northern Sierra San Pedro Mártir field area (Johnson et al., 1999a). Also, within a few kilometers of the Main Mártir thrust fold hinges rotate into steeply plunging orientations testifying that a substantial amount of shear has occurred across that structure. Similarly,

while strains within the shear zone of the aABF are extremely high, the zone itself is relatively small. Extremely high strains within the Sierra Calamajue occur over a zone greater than a kilometer in width.

Deformation not only appears to be decreasing towards the aABF map area from the southwest it also appears to continue to decrease further to the northwest. In a study area approximately 40 km northwest of the aABF study area (~20 km east of Punta China, Fig. 4.2) the Alisitos Formation deformed into large (>5 km wavelength) open folds in an area less than 5 km south of the active ABF (Wetmore and Schultz, unpublished mapping). Furthermore, strain data collected from this region possess maximum intensities of 0.36 with less than 25% shortening in the z-direction (Table 4.2, PWS samples).

Geochronologic constraints.

U/Pb zircon age determinations for the plutonics in this region provide some useful constraints on the timing of deformation in the Alisitos arc segment. In particular, both the Piedra Rodada and Balbuena plutons exhibit useful cross cutting relationships. The Piedra Rodada pluton, located just south of the aABF (Fig. 4.2), seems to have been strongly affected by shear across that structure as a gradient in the type and intensity of foliation is observed with proximity to the shear zone. Thus, shear across the aABF must have continued at least until 105.5 $\pm$ 3.4 Ma. Two ages were determined for the Balbuena pluton that deflects isoclinal folds within the Alisitos Formation north east of the El Tigre fault (Fig. 4.2). This indicates that a substantial proportion of the contractional deformation must have been completed by 108.6 $\pm$ 3.96 Ma. Furthermore,

since almost no subsolidus fabrics are observed within the Balbuena pluton and the orientations of magmatic foliations within the pluton show no clear relationship to regional fabrics it seems likely that deformation was localized on other, more distant structures.

U/Pb analysis of plutonic zircon populations also serves as an imperfect survey of the stratigraphy present beneath the arc. For example, in the small number of U/Pb ages for both volcanics and plutonics from the Santiago Peak arc segment in southern California the presence of xenocrystic Precambrian zircons were always present (e.g., Anderson, 1991; Herzig, 1991; Premo et al., 1998) betraying the fact that the Bedford Canyon Complex forms the basement to that arc segment. In this study 92 zircons from plutons intruding the Alisitos arc segment were analyzed and all yielded Cretaceous ages. When combined with all published U/Pb data collected from volcanics and plutonics of the Alisitos arc segment (e.g., Carrasco et al., 1995; Johnson et al., 1999a, 2003) no zircons older than Cretaceous have been identified. We tentatively interpret this observation to indicate that continentally derived sediments do not comprise a significant component of the Alisitos arc segment basement. This conclusion is also consistent with recent geochemical studies of plutons of the northern Sierra San Pedro Mártir that argue for no assimilation of siliciclastic strata similar to the Bedford Canyon Complex sediments (Tate et al., 1999; Tate and Johnson, 2000).

Geochemical considerations.

The tectonic and magmatic evolution of the Alisitos arc segment described by Tate and Johnson (2000), for plutons of the northern Sierra San Pedro Mártir study area (Fig.

4.2) indicated that an already thick arc produced adakitic magmas after significant collision related crustal thickening. This scenario, while clearly appropriate to explain the observations from Sierra San Pedro Mártir area plutons, does not seems to apply to those of the aABF study area. The chemical compositions of all of the plutons analyzed in this study overlap with those of the older plutons in the western belt (Table 4.3, Figs. 4.12 and 4.13). This consistency in chemical composition persists in the aABF region even though most of the plutons analyzed here yield crystallization ages within two or three million years for those exhibiting adakitic chemistries (108.5 $\pm$ 1.2 to 102.5 $\pm$ 1.6 Ma; Johnson et al., 1999a). One explanation for the observed geochemical difference between the plutons of these two study areas is that the aABF region did not experience as much contractions/crustal thickening as the Sierra San Pedro Mártir region. However, given the limited number of analyses for the plutons in the aABF region, we view this discrepancy with skepticism until a more thorough data set is available.

Summary and Conclusions

The northern part of the Alisitos arc segment is characterized by a southwest-vergent fold and thrust belt that abuts against the aABF. Moderately sediment rich strata northeast of the El Ranchito fault support the interpretation that an interarc basin existed along the northeastern margin of the Alisitos arc between it and the North American margin. Sediments in this basin were derived from both the active Alisitos arc and the North American continental margin with an apparent increase in sediments derived from the latter source toward the northeast (i.e., toward the continent) and with decreasing age. Contractional deformation in this region was primarily taken up by the numerous folds

developed within the Alisitos Formation. However, the total magnitude of shortening in the aABF region appears to be intermediate between a greater amount to the south and a much small amount further to the northwest. In part this may have result from variation in the geology and geometry of the margin along the length of the paleotrench. The greatest magnitudes of contractional deformation exist in the region of the Sierra San Pedro Mártir where a portion of the Late Proterozoic-Paleozoic Miogeocline protrudes. The shape of the margin along with the orientation of convergence vectors relative to the margin may also account for the observed differential contraction. If the direction of convergence between the Alisitos arc and the continental margin was nearly orthogonal for the Sierra San Pedro Mártir and the Sierra Calamajue areas, then sense of convergence would have been oblique along the aABF. The timing of initial contraction is not constrained in the aABF region but continued until at least ~100 Ma with the majority of fold closure completed by about 108 Ma. The lesser amount of shortening experience by the northern part of the Alisitos arc segment appears to have excluded this region from the generation of adakitic melts which are produced at crustal depths in excess of ~35 km and observed further south west of the Sierra San Pedro Mártir.

CHAPTER 5: PRIMARY GRAIN SHAPES AND PREFFERED ORIENTATION DATA: WHY NO ANALYSIS OF FINITE STRAIN IS COMPLETE WITHOUT THEM

Introduction

The average grain preferred shape and orientation of many populations of markers (e.g., ooids, volcanic lithics) may be represented as an ellipsoid (e.g., Shimamoto and Ikeda, 1976). Such ellipsoids are commonly calculated to assess the total amount of distortional strain in a body of rock. However, the ellipsoid that is commonly calculated in these instances is more appropriately termed a final fabric ellipsoid since it reflects: (1) the shape and orientation of the initial (primary) fabric; (2) post depositional compaction and diagenesis; (3) viscosity contrasts between the population of markers and the enclosing matrix; (4) particle interactions; (5) volume changes of the markers; and (6) tectonic strain(s) applied to the population. While knowledge of the shape and orientation of the primary fabric ellipsoid is necessary to resolve the latter four effects, most researchers make assumptions about primary fabric ellipsoids without quantifying their nature. The most common assumptions are the following: (1) objects were initially spherical; (2) objects were initially non-spherical but had a uniform orientation; (3) object populations initially had a preferred orientation, but that this preferred orientation had a symmetrical relationship to bedding; or (4) that the effects of initial fabrics are recognizable even after imposed tectonic strains. In detail, however, the above assumptions are generally incorrect, even for the most ideal fabric elements used to

measure tectonic strains (Boulter, 1976; Shimamoto and Ikeda, 1976; Tobisch et al., 1977; Pfiffner, 1980; Holst, 1982; Paterson and Yu, 1994; Paterson et al., 1995).

Previous studies of initial grain shapes and orientations are relatively few in number and limited in scope and utility. Most sedimentological studies measure either grain shapes or orientations (e.g., Curtis et al., 1980) but rarely combine both data sets. Similarly, most early primary fabric studies made by structural geologists were collected solely to test various strain analysis methods and thus provide only two dimensional data and commonly only in graphic form (Elliott, 1970; Dunnet and Siddans, 1971; Boulter, 1976; Seymour and Boulter, 1979; Holst, 1982). In order to remove the effects of primary fabrics three-dimensional shape and orientation data is required (e.g., Paterson and Yu, 1994; Paterson et al., 1995). This study builds on the contributions made by Paterson and Yu (1994) and Paterson et al. (1995) by expanding the database on primary fabrics to include volcanics, volcaniclastics, and conglomerates. In this paper we present the primary fabric ellipsoids for competent lithics, pumice, and numerous types of phenocrysts in volcanics, as well as primary fabric ellipsoids for conglomerates, immature sandstones and mudrocks, the latter two from previous studies (Paterson and Yu, 1994; Paterson et al., 1995). We evaluate the relative utility of each of these markers to identify those that are most appropriate for quantifying tectonic strains. We also use approximate marker shapes for each of the volcanic populations to evaluate depositional and post-depositional (e.g., compaction) processes. We then describe methods to remove the effect of primary fabrics from the final fabric ellipsoid to better determination of the true tectonic strain in a rock. Finally, we use the average primary fabrics determined in

this study to illustrate the significant contribution they can make to a final fabrics and how ignoring their contribution can lead to erroneous interpretations.

Volcanics and volcaniclastic rocks are ideally suited for strain studies since they commonly possess a variety of markers that can track the distortional component of deformation. For example, populations of lapilli-sized (2-64 mm) fragments within deformed volcanic and volcaniclastic rocks have long been employed to quantify strains (e.g., Oertel, 1970; Roberts and Siddans, 1971; Coward and James, 1974; Paterson et al, 1989; Johnson et al., 1999a). These fragments can include both lithic and accretionary lapilli, pumice, and various types of phenocrysts. While the utility these markers possess for quantifying strains is clear, very little work has addressed the shapes and orientations of primary fabric ellipsoids in volcanic rocks. One notable exception is Tobisch et al. (1977) who quantified primary fabrics from comparable units within which they measured strains in the Ritter Range of east-central California. In their study fabrics were measured using accretionary lapilli, competent lithics, reduction spots, and pumice.

Sample Descriptions

Primary fabrics were measured in volcanic and volcaniclastic samples from the Basin and Range Province and the western part of the Peninsular Ranges of Baja California. The rocks analyzed represent three distinctive tectonic and/or depositional environments, as well as a wide range of petrologic rock types all discussed below. We also summarize below primary fabrics from conglomerates, immature sandstones, and mudrocks from a variety of depositional environments. The conglomerates were collected from numerous locations throughout southern California. For more complete descriptions of the sample

localities for immature sandstones and mudrocks see Paterson and Yu (1994) and Paterson et al. (1995), respectively.

Samples from the Basin and Range Province

Volcanic samples collected from the Basin and Range Province of Nevada and Arizona range from basaltic andesite lava flows to rhyolite ash flow tuffs. They were erupted between ~11 and ~19 Ma during extensional collapse of that part of the Cordillera (e.g., Gans et al., 1989). Nearly all Basin and Range samples contain both quartz phenocrysts and pumice with many possessing competent lithics. With the exception of some minor tilting associated with range-bounding normal faults, all samples used in this study are undeformed in that they exhibit no observable cleavage or other microstructural signs of tectonic strain.

Samples from the Western Peninsular Ranges

The second group of samples used in this study was collected from the western Peninsular Ranges of Baja California, Mexico. Strata of the western Peninsular Ranges include Early Cretaceous arc volcanics and volcaniclastics deposited in two distinct environments. The Santiago Peak Volcanics, preserved to the north of the ancestral Agua Blanca fault represent subarial deposits of a continental margin arc (Adams, 1979; Herzig, 1991). The Alisitos Formation, preserved to the south ancestral Agua Blanca fault, represents the submarine deposits of an oceanic island arc (Allison, 1955, 1974; Beggs, 1984; Fackler-Adams and Busby, 1998; Wetmore et al., 2002). The Santiago Peak Volcanics and Alisitos Formation exhibit a range of compositions from basalts to

rhyolites. However, samples collected for this study are typically andesites and dacites with abundant lithics and phenocrysts with plagioclase feldspar the most common. Pumice is not typically observed in the Peninsular Range samples analyzed in this study, but does occur occasionally.

Locally, both the Santiago Peak Volcanics and the Alisitos Formation do exhibit extremely intense deformation. Within the Santiago Peak Volcanics this deformation is typically concentrated within the structural aureoles of numerous plutons that intrude the western Peninsular Ranges. The Alisitos Formation exhibits additional intense deformation along the ancestral Agua Blanca fault and other large thrust faults (Wetmore et al., 2002; Johnson et al., 1999b). Samples from both the Santiago Peak Volcanics and Alisitos Formation were collected from localities where deformation due to either pluton emplacement or thrust faulting was absent. Samples of the Santiago Peak Volcanics were collected from coastal exposures and the hills surrounding the city of Ensenada, Mexico. Samples of the Alisitos Formation were collected from roadside exposures outside of the coastal town of Eréndira, Mexico. None of the Peninsular Range samples collected and used in this study exhibit observable cleavage or other microstructural signs of tectonic strain.

Analytical Methods

Populations of markers consisting of approximately ellipsoidal objects (e.g., phenocrysts) with variable shapes and orientations can be represented by an ellipsoid with three principle axes, $X>Y>Z$ (Shimamoto and Ikeda, 1976). Directed fabric ellipsoids (following Oertel, 1981) in which axes are oriented with respect to true

geographic coordinates were calculated for populations of fabric markers in the following manner. Three mutually perpendicular, but otherwise arbitrary, cuts were made of each sample and an XYZ coordinate system established using the intersections of each face. On each face the length of the longest and shortest axes (in a direction perpendicular to that of the long dimension) and the orientation of the long axis relative to the XYZ reference frame was measured for 30 to 100 markers for each population present (Fig. 5.1). Three dimensional fabric ellipsoids were calculated from two-dimensional ellipses using the techniques of Shimamoto and Ikeda (1976) and Miller and Oertel (1979). When geographic orientations and bedding were available the fabric ellipsoids are reoriented to geographic coordinates and the XY plane of the fabric ellipsoid is compared with that of the bedding plane. Paterson et al. (1995) measured fabric ellipsoids in mudrocks using an X-ray goniometer in transmission mode. Sample preparation techniques, data collection, and analysis are discussed in Oertel (1983).

Further evaluation of the grain shapes for each population of markers was accomplished by calculating an approximate grain shape ellipsoid (AGSE). Calculation of the AGSE was accomplished by artificially aligning the long axes of each marker on each face in every sample such that Phi (ϕ) on the XY=90°, YZ=0°, and ZX=90°. The AGSE determined in this manner is approximately, though not precisely, the average marker shape. Since the true grain shape determined in this manner can only be calculated when the cuts of a rock are made exactly parallel to the three axes of the

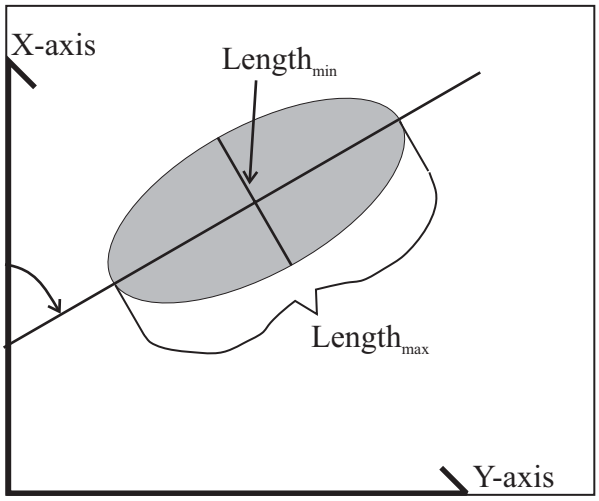

Figure 5.1. Simplified clast illustrating the means by which shape and orientation data are collected.

marker ellipsoid the AGSE reported here is an approximation. As such, the axial lengths, and therefore ratios, of the AGSE reported here are potentially somewhat less than those of the true grain shape of any marker population. Notwithstanding, the calculation of this additional ellipsoid allows for a quantitative assessment of the degree of randomness in orientations exhibited by the fabric markers.

Visual comparison of individual ellipsoids is accomplished by plotting data on modified Flinn diagrams where each ellipsoid may be represented as a single point (Figures 5.2 and 5.3). Data plotted in a modified Flinn diagram derives from the principle axes (X,Y,Z) as the vertical axis of the plot is the natural logarithm of the ratio X/Y and the horizontal is the natural logarithm of Y/Z. Alternatively, this is the same as the difference between the natural strains (cf. Ramsay and Huber, 1983, p. 281) of E_1-E_2 for the vertical axis and E_2-E_3 for the horizontal axis. Figure 5.3 shows plots of both directed fabric ellipsoids and AGSE with tie lines connecting ellipsoids for corresponding samples. These tie lines provide a visual means of qualitatively assessing the degree of randomness exhibited by the long axes of markers in a given sample.

Volcanics and volcaniclastics commonly contain a variety of objects whose shapes can be approximated by ellipsoids, thus making them prime targets for studies seeking to quantify strains. We have analyzed populations of phenocrysts (e.g., quartz, various types of feldspar, biotite, and hornblende), pumice (typically with collapsed or partially collapsed vesiculated structures), and competent lithics (angular volcanic fragments, either from the same magma that produced the ash flow or as an accidental inclusion).

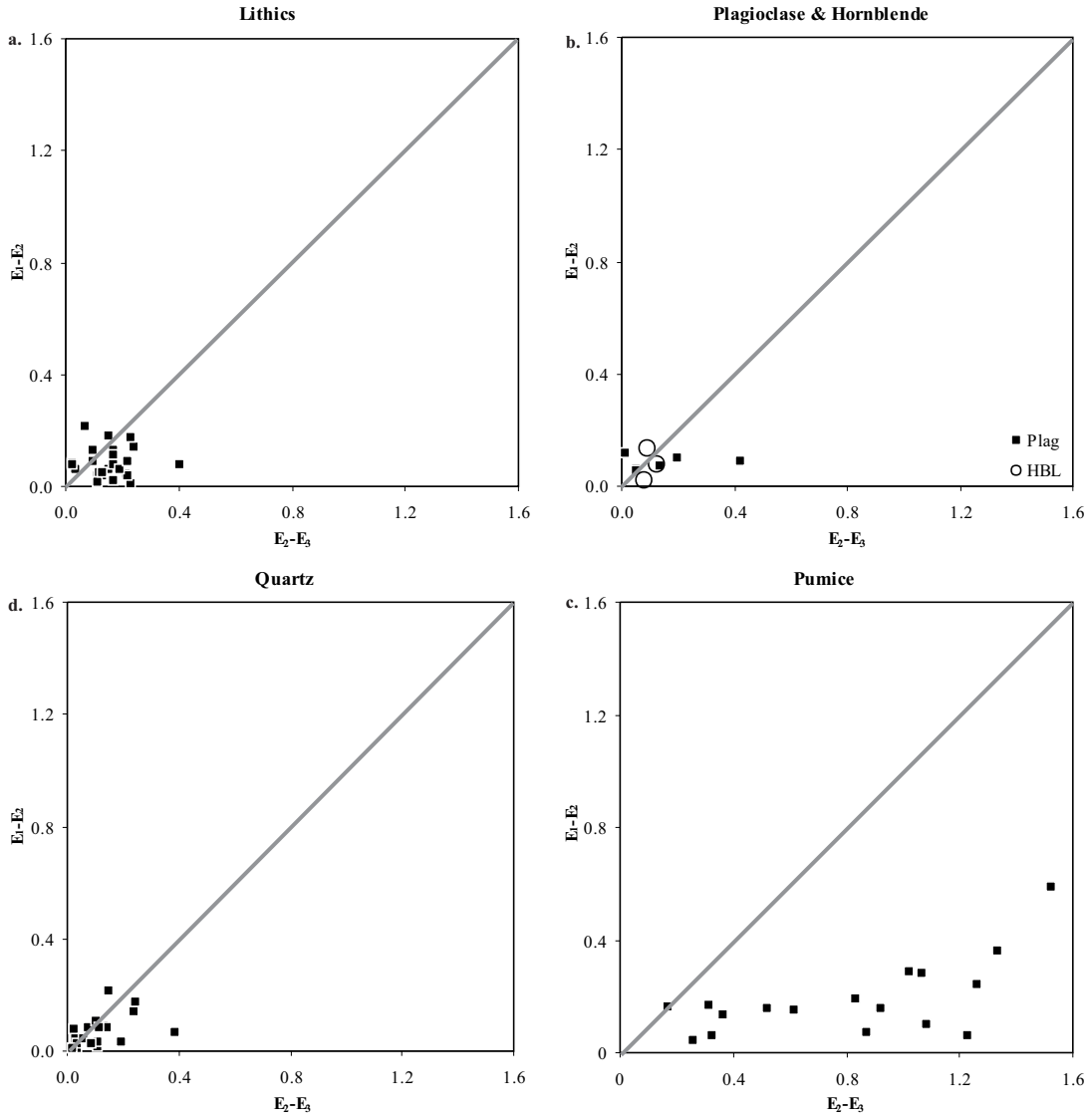

Figure 5.2. Modified Flinn plots showing the calculated directed fabric ellipsoids for a) lithics, b) plagioclase and hornblende phenocrysts, c) quartz phenocrysts, and d) pumice.

Figure 5.2. Continued

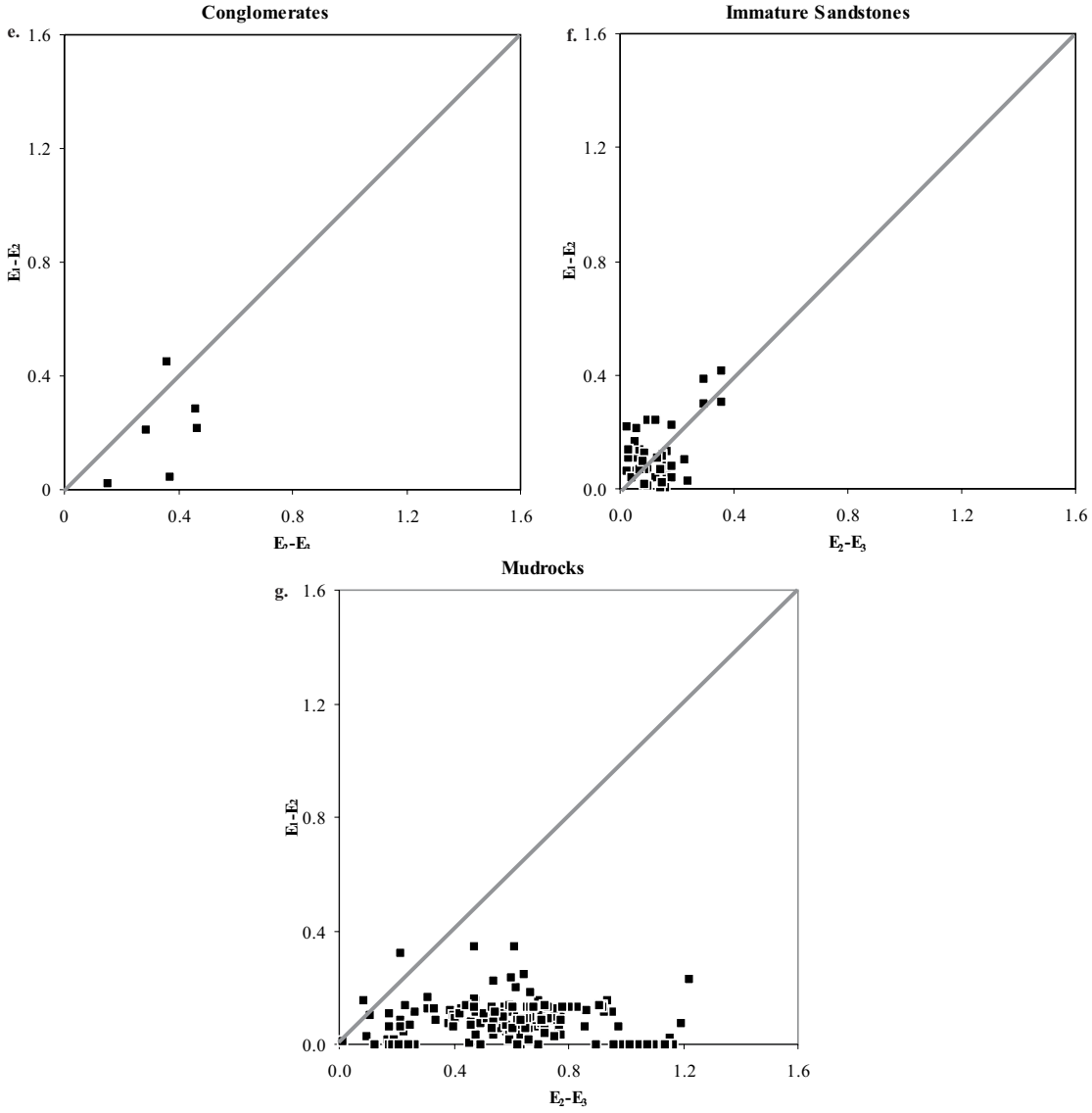

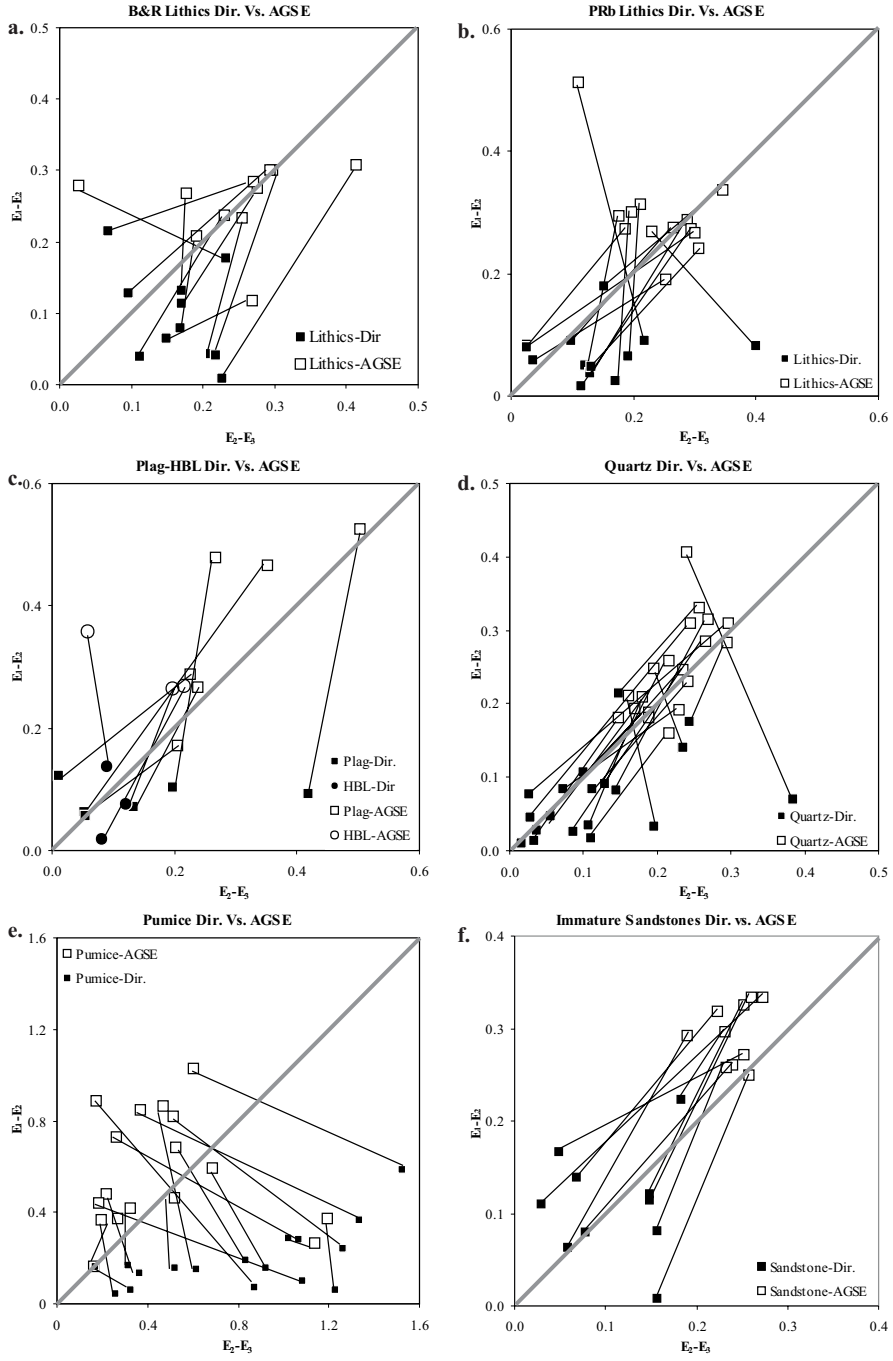

Figure 5.3. Modified Flinn plots showing both the directed and AGSE with tie lines connecting ellipsoids from both sets. Note that the lithics have been split into two different plots to facilitate understanding.

Fabric Results

Thirty-five volcanic and volcaniclastic samples with different populations of markers were analyzed for this study resulting in the calculation of 69 directed and 68 AGSE. Most samples contained multiple types of markers including competent lithics, phenocrysts (plagioclase, hornblende, and quartz), and pumice. The graphical and statistical results of these analyses are given in Figures 5.2 and 5.3, and Appendix C, respectively. Figures 5.2 and 5.3 are modified Flinn diagrams where the differences between the natural strains (apparent in the case of primary fabric ellipsoids) are plotted. The raw data presented in Appendices C Table C.1 (directed fabric ellipsoids) and Table C.2 (AGSE) include: the ellipsoid axial lengths, the apparent constant volume extensions (determined by calculating percentage difference between axial lengths and radius of a sphere of equal volume), apparent strain magnitude (calculated as $1/3[(E_1\text{-}E_2)^2 + (E_2\text{-}E_3)^2 + (E_3\text{-}E_1)^2]^{1/2}$ (Hossack, 1968) where E_1, E_2, and E_3 are the principle natural strains), lodes parameter (a shape parameter also introduced by Hossack, (1968) calculated as $\nu = 2E_2 - E_1\text{-}E_3/E_1\text{-}E_3$), total error, and the angle between XY-plane of the fabric ellipsoid and bedding.

Volcanics and volcaniclastics

Competent lithics. Directed fabric ellipsoids for competent lithics were calculated from 25 samples (Fig. 5.2a). X/Z ratios range from 1.12:1 to 1.62:1 with the average X:Y:Z of 1.27:1.17:1. Ellipsoid shapes for competent lithics exhibit a slight skew toward oblate (i.e., positive Lodes parameters) but exhibit the entire range from oblate to prolate. AGSE (Fig. 5.3a and b) have higher axial ratios than their corresponding directed

ellipsoids. Tie lines between the two types of individual ellipsoids typically parallel the plane strain line or are more steeply sloping, occasionally showing an increase toward constrictional.

Phenocrysts. Directed fabric ellipsoids for plagioclase phenocrysts were calculated from six (6) samples (Fig. 5.2b), four from the western Peninsular Ranges and two from the Basin and Range Province including one sample with sanidine from the Peach Springs Tuff (PST) of western Arizona-eastern California (Glazner et al., 1986). X/Z ratios range 1.12:1 to 1.67:1 with the average X:Y:Z of 1.27:1.17:1. Plagioclase ellipsoids exhibit a strong skew toward oblate shapes with only one prolate sample. AGSE (Fig. 5.3c) all have higher axial ratios than their corresponding directed ellipsoids with tie lines between the two that subparallel or slope more steeply than that of the plane strain line.

Directed fabric ellipsoids for hornblende phenocrysts (Fig. 5.2b) were calculated from only three (3) samples thus, minimizing the significance of observations made here until more volcanic samples can be studied. X/Z ratios range from 1.1:1 to 1.25:1 with the average X:Y:Z of 1.19:1.1:1. The shapes of these ellipsoids are all close to the plane strain line, intermediate between prolate and oblate. AGSE for hornblende (Fig. 5.3d) all have higher axial ratios than their corresponding directed ellipsoids with tie lines between the two subparallel to that of the plane strain line for two samples and nearly vertical for the third.

Directed fabric ellipsoids for quartz phenocrysts (Fig. 5.2c) were calculated from 19 samples, 18 from Basin and Range Province samples and one from the western Peninsular Ranges. X/Z ratios range from 1.07:1 to 1.58:1 with the average X:Y:Z

1.22:1.13:1. While quartz ellipsoid shapes do generally parallel the plane strain line with a few within the prolate field those ellipsoids with the largest axial ratios (i.e., sample 198-Q) all lay within the oblate field. AGSE for quartz (Fig. 5.3d) all have higher axial ratios than their corresponding directed ellipsoids with tie lines between the two subparallel to that of the plane strain line for all but three of the samples including the two yielding the most oblate directed fabric ellipsoids. These samples yield tie lines between the directed ellipsoids and AGSE that have a negative slope but still do not significantly overstep plane strain into prolate shapes.

Pumice. Directed fabric ellipsoids for pumice (Fig. 5.2d) were calculated from 17 samples, 16 from Basin and Range Province samples and one from the western Peninsular Ranges. X/Z ratios range from 1.35:1 to 8.26:1 with the average X:Y:Z 3.09:2.43:1. Ellipsoid shapes for pumice all fall within the oblate field. AGSE for pumice (Fig. 5.3e) all have higher axial ratios than their corresponding directed ellipsoids with tie lines between the two all steep and nearly all have negative slopes. Most non-directed fabric ellipsoids thus lie along the plane strain line or within the prolate field.

Sediments

Conglomerates. Directed fabric ellipsoids for conglomerates (Fig. 5.2e) were calculated from six (6) samples. X/Z ratios range from 1.19:1 to 2.10:1 with the average X:Y:Z 1.73:1.42:1. Ellipsoid shapes for conglomerates range from approximately plane strain to strongly oblate. AGSE have not been calculated for any conglomerate samples.

Immature Sandstones. Paterson and Yu (1994) present directed fabric ellipsoids for 43 immature sandstones samples (Fig. 5.2f). X/Z ratios range from 1.09:1 to 2.17:1 with

the average X:Y:Z 1:31:1.14:1. Ellipsoid shapes exhibit a nearly even distribution between prolate and oblate with those with the highest axial rations characterized by plane strain shapes. AGSE were not calculated for the sandstone samples.

Mudrocks. Paterson et al. (1995) present directed fabric ellipsoids for 173 mudrock samples (Fig. 5.2g). X/Z ratios range from 1.02:1 to 4.27:1 with the average X:Y:Z 2.11:1.93:1. Ellipsoid shapes are nearly all within the oblate field with the exception of a few samples with relatively small axial ratios that plot just into the prolate field. AGSE were not calculated for the mudrock samples.

Fabric ellipsoids and bedding

Directed fabric ellipsoids were reoriented into true geographic orientations for 63 of the 69 ellipsoids calculated from volcanic and volcaniclastic samples in this study. Paterson and Yu (1994) also reoriented 30 of their immature sandstone samples and Paterson et al. (1995) reoriented all 173 of the mudrock samples. Comparing ellipsoid orientation data with bedding orientations a test of the validity of the commonly stated assumption that primary fabrics possess a symmetrical relationship to bedding. Figure 5.4(a-c) shows three plots of the axial ratio XZ compared with the angle between the XY plane of the directed fabric ellipsoid and the bedding plane for different markers. The plots for competent lithics, immature sandstones, and all three phenocryst populations show no obvious correlation between fabric intensity and angle between ellipsoids and bedding. In particular, for lithics, plagioclase, and quartz all possible angles are observed

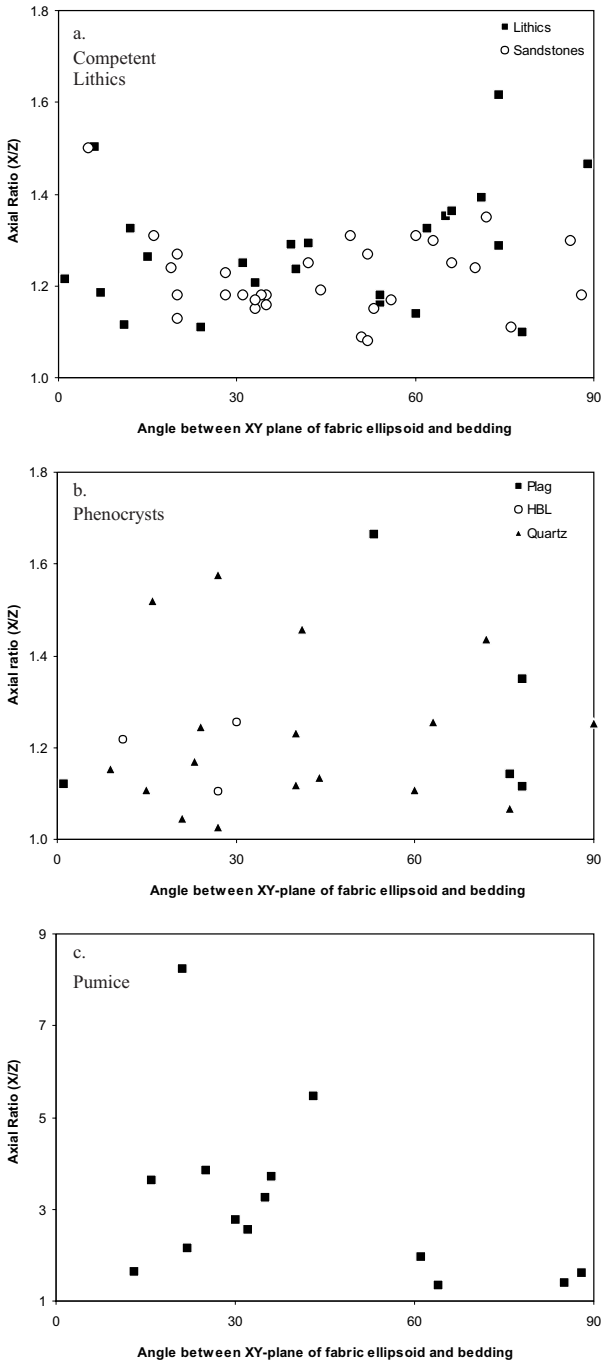

Figure 5.4. Plots of axial ratio (X/Z) versus the angle between the XY plane of the directed fabric ellipsoid and bedding.

for the range of XZ ratios. The plot for pumice (Fig. 5.4c) also exhibits the entire range of possible XY plane-bedding angles but does suggest that at high axial ratios the angle between the XY plane and bedding decreases. Phyllosilicates in mudrocks are consistently flattened parallel to bedding (Paterson et al., 1995).

Discussion

The primary fabric data collected in this study, like those from previous investigations (e.g., Tobisch et al., 1977), clearly invalidate many of the assumptions regarding primary fabrics discussed in the introduction. While some of the populations do have AGSE with very small axial ratios none are truly spheres. Since none of the directed fabric ellipsoids are spherical the markers cannot have uniform orientations. And finally, with the exception of strongly flattened pumice and mudrocks, there is no consistent symmetrical relationship between the fabric ellipsoid and bedding for any population of markers. The fourth assumption is likewise unlikely to be valid given the wide range of primary fabric ellipsoid shapes and orientations.

Based on the modified Flinn plots in Figure 5.2, it is clear that not all fabric elements are equally useful for quantifying tectonic strains. An ideal marker population for quantifying tectonic strains is one with a primary fabric ellipsoid that closely approximates a sphere or one that exhibits only minor variations in initial shapes. On this basis competent lithics and quartz phenocrysts are the most useful fabric markers examined in this study. In contrast, pumice and mudrocks require the most caution when attempting to quantify strain, because of the large average primary fabric ellipsoid and the extreme variation in initial shape. Hence, it is difficult to know uniquely, the precise

shape and orientation of the primary fabric ellipsoid for pumice or mudrocks prior to initiation of tectonic deformation.

Comparison of the approximate marker shapes (AGSE), the primary fabric (directed fabric ellipsoids), and the relationship of the latter to bedding allows for interpretations regarding the origin of primary fabrics. The AGSE of most markers are of plane strain to slightly prolate. The shift towards the origin and into the oblate field on the modified Flinn diagrams (Fig. 5.3) for corresponding directed fabric ellipsoids suggests that there is some degree of uniformity in the distribution of clast orientations. Alternatively, when fabric marker orientations are not uniform, the long axes lie in the same approximate plane thus yielding an oblate ellipsoid. No correlation exists between fabric ellipsoid eccentricity and bedding (Fig. 5.4) for most of the fabric elements as each marker exhibits the entire range of angles (0-90°) and an average angle between the two at ~45°. Thus, we suggest that the primary fabrics exhibited by most markers likely results from initial grain settling and deposition onto variably shaped and oriented existing grains and is not significantly affected by later compaction that would tend to reduce the angle between bedding and the XY plane of the primary fabric ellipsoid. The exact opposite appears to be true of pumice and phyllosilicate grains in mudrocks. While the AGSE of pumice is prolate, directed ellipsoids are nearly all oblate and those with the largest axial ratios correspond to the ellipsoids with the smallest angles between the XY plane and bedding. Therefore, in the case of pumice and phyllosilicates in mudrocks compaction appears to modify primary depositional fabrics.

Primary Fabric Corrections

Corrections to remove the primary fabric effect on finite fabric ellipsoids can proceed by one of several methods depending upon the desired level of accuracy and the level of information available on ellipsoid orientation. In the absence of information on the orientation of the primary fabric ellipsoid, or in the situation where the ellipsoid does not exhibit a consistent relationship to bedding and/or flow direction, then the coaxial combination of the finite fabric ellipsoid and the inverse of the mean primary fabric ellipsoid is the most appropriate means of making this correction. This is accomplished by multiplying these two ellipsoids for each of the six possible coaxial combinations:

X_FX_P: Y_FY_P: Z_FZ_P $\quad$ X_FY_P: Y_FZ_P: Z_FX_P

X_FX_P: Y_FZ_P: Z_FY_P $\quad$ X_FY_P: Y_FX_P: Z_FZ_P

X_FZ_P: Y_FX_P: Z_FY_P $\quad$ X_FZ_P: Y_FY_P: Z_FX_P

where X_F, Y_F, and Z_F are the three axes of the finite fabric ellipsoid and X_P, Y_P, and Z_P are those of the inverse of the primary fabric ellipsoid (Ramsay, 1967). The result of removing the primary fabric effect in this manner is six (6) separate ellipsoids that define an area of approximately triangular shape on a modified Flinn plot. The true tectonic strain is thus bracketed within this area. It follows, therefore, that as the primary fabric ellipsoid approaches a sphere the size of the area within which the possible strain ellipsoid exists decreases towards a single point.

Since a relatively broad range of shapes and sizes characterize some populations of markers, using a single (average) ellipsoid may not produce a result that is altogether

accurate. Therefore, a more accurate correction can be made following this same method described above but using the most extreme primary fabric ellipsoids in the range for a specific population of markers. The result of correcting for the primary fabric effect in this manner is to produce multiple triangular shaped regions on a modified Flinn diagram that together bracket the tectonic strain.

In some situations orientations of primary fabric ellipsoids relative to an external reference frame (e.g., bedding) may be known and employed in the primary fabric correction. For example, the primary fabric ellipsoid for mudrocks and some pumice samples do exhibit symmetry with bedding. The corrections for the primary fabric contribution can proceed by multiplying the finite fabric ellipsoid by the inverse primary fabric ellipsoid with the X and Y-axes parallel to the bedding plane. This will need to done with the X-axis of the primary fabric ellipsoid oriented both parallel to and perpendicular to that of the finite fabric ellipsoid. The results of correcting for the primary fabric effect in this manner are two fabric ellipsoids that may be connected by a single line. Tectonic strain, therefore, most exist on that line.

The primary fabric ellipsoids described above serve, not only as a guide for deciding between potential fabric markers but, also to illustrate potential errors if primary fabrics are ignored when assessing tectonic strains. These errors are potentially significant given that strain is multiplicative. Thus, even the primary fabric of a population of markers with a small deviation from a sphere can have a large effect on the finite fabric exhibited by those markers after straining. Below are two general examples where ignoring primary fabrics during strain assessments can/have produced misleading results.

A long-standing problem in structural geology has been the observation that many thrust fault systems are characterized by flattening strains (e.g., Hossack, 1968). While studies have sought to resolve the apparent space problem created by flattening in this setting (e.g., Huddleston, 1999) at least part of the problem can be resolved by accounting for primary fabrics. In the original study by Hossack (1968) he used pebbles from the Bygdin Conglomerate, Norway to determine strain. Although Hossack (1968) did recognize the potential errors inherent in assuming initially spherical pebbles he did not correct the data for the contribution of primary fabrics. In this case the observed flattening strains may be misleading given that t primary fabric ellipsoids for conglomerates (Table 5.1; Fig. 5.2e) may be well within the flattening field indicating that if the resultant applied tectonic strains were of plane strain or slightly oblate then the final ellipsoid shape would remain in the flattening field (Fig. 5.5) without implying a space problem. Given that most populations of markers reported in Table 1 yield average ellipsoids that plot within the oblate field the specific example above is not likely to be an isolated occurrence.

Table 5.1. Mean fabric ellipsoids for all primary fabric data collected and presented in appendix 1. App. C.V. Extension: Apparent constant volume extension as departed from a sphere.

	Length normalized ratio			Apparent constant volume extension			Apparent strain	Lodes
Sample	X	Y	Z	X	Y	Z	magnitude	parameter
Competent Lithics	1.28	1.17	1	11.46	2.41	-12.13	0.17	0.26
Plagioclase	1.27	1.17	1	11.18	2.07	-11.31	0.17	0.04
Hornblende	1.19	1.10	1	8.88	0.63	-8.65	0.13	0.20
Quartz	1.22	1.13	1	9.42	1.56	-9.61	0.14	0.20
Pumice	3.09	2.43	1	51.82	23.51	-42.62	0.75	0.59
Conglomerates	1.73	1.42	1	27.27	5.75	-25.02	0.38	0.39
Mud Rocks	2.11	3.35	1	30.71	20.23	-34.76	0.76	0.73
Sandstones	1.31	1.37	1	13.82	0.17	-11.69	0.18	0.06

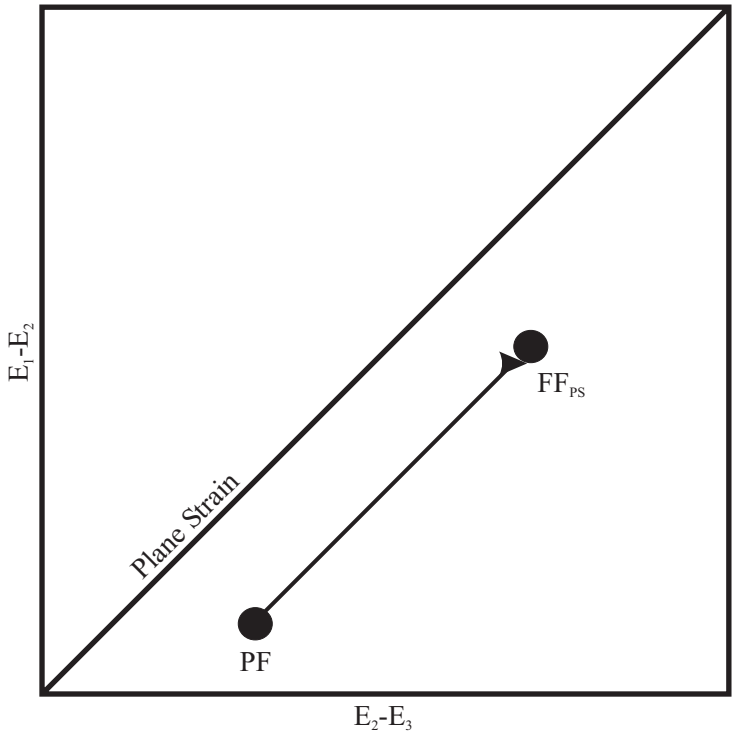

Figure 5.5. Modified Flinn diagram illustrating the net result (FF) of applying a plane strain to a population of markers with a flattening primary fabric (PF).

Similar issues arise in studies attempting to resolve the emplacement mechanisms of intrusive bodies using strain data collected from within plutons and their enveloping host rocks. Space making models such as ballooning or diapirism commonly requires substantial amounts of ductile flow of the host rock around the intruding magma. Typically flattening strains are predicted to occur both within the pluton, in the outer-most phases, and within the surrounding host. Thus, when oblate shaped final fabric ellipsoids are calculated from enclaves within the pluton or other markers in the host the conclusion is that the space was made by ballooning or inflation of a central magma chamber (e.g., Molyneux and Hutton, 2000). However, while this overly simplified example may seem somewhat cliché, it illustrates two very important points repeated several time in this paper. First, substantial miscalculations are likely to occur when primary fabrics are not accounted for while attempting to determine tectonic strains. Since most populations of fabric markers yield primary fabric ellipsoids that plot within the oblate field the identification of a final fabric ellipsoid that plots within the oblate field does not uniquely require that the population experienced a flattening strain. Secondly, not all fabric elements are created equal (Fig. 5.6). Fabric elements that are good for assessing tectonic strain should have similar histories throughout the population, with a relatively precise primary fabric ellipsoid.

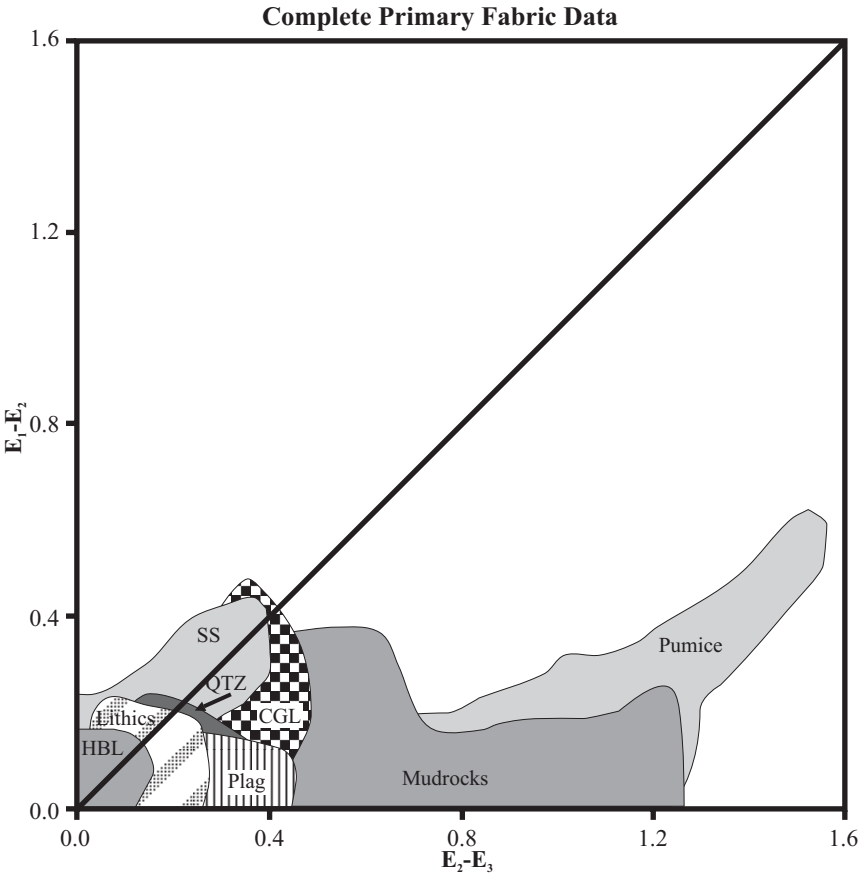

Figure 5.6. Modified Flinn diagram showing regions within which all populations of fabric markers analyzed in this and previous studies (Paterson and Yu, 1994; Paterson et al., 1995)

Conclusions

The above evaluation of primary fabrics illustrate that even the most ideal marker populations possess a grain preferred shape and orientation. However, some of these are more significant than others as illustrated by differences between quartz phenocrysts and pumice clasts. Furthermore, based on the primary fabric data above it is clear that many of the long-held assumptions regarding the nature of such fabrics are incorrect. That is: (1) the initial shapes of all fabric elements analyzed here were not spherical; (2) they do not possess random or uniform orientations; and (3) the fabrics identified and described for these markers do not exhibit a symmetrical relationship to bedding.

Given that these commonly held assumptions regarding primary fabrics are incorrect it follows that additional care must be taken to include information on these prestrain fabrics when attempting to quantify tectonic strains. This applies even for those marker populations that exhibit small ellipsoidal shapes due to the fact that strains are multiplicative thereby magnifying rather than removing the primary fabric effect. Ideally, therefore, we believe that the best approach to constraining the contributions made by primary fabrics is to study them in undeformed examples of the rocks in which strain is being evaluated as was done by Tobisch et al. (1977).

Because the orientations of the primary fabric ellipsoids reported here rarely exhibit consistent relationships to bedding directed removal of the primary fabric contribution is not generally possible. Thus, the most appropriate means of correcting for the contribution of a primary fabric is to multiply the finite fabric ellipsoid by the reciprocal of the mean primary fabric ellipsoid coaxially. This process, therefore, brackets the range of possible tectonic strain.

The primary fabric data described above represents a small portion of the different types of markers commonly employed to constrain tectonic strains. Future investigations of primary fabrics should seek to expand this data set to include information on some of the most commonly used populations including ooids, accretionary lapilli, and expanded data on different types of conglomerates. Such information will not only serve to improve the accuracy of studies seeking to assess the magnitude and type of strains effecting a region of rock but can also lead to improved understanding of the strain path.

REFERNCES

Adams, M. A., 1979, Stratigraphy and petrology of the Santiago Peak Volcanics east of Rancho Santa Fe, California: M.S. thesis, San Diego State University, San Diego, CA, 123 p.

Allen, C., L. Silver, and F. Stehil, 1960, Agua Blanca fault--a major transverse structure of northern Baja California, Mexico: Geological Society of America Bulletin, v. 71, p. 457-482.

Allison, E. C., 1955, Middle Cretaceous Gastropoda from Punta China, Baja California, Mexico: Journal of Paleontology, v. 29, p. 400-432.

Allison, E. C., 1974, The type Alisitos Formation (Cretaceous, Aptian-Albian) of Baja California and its bivalve fauna, *in* G. Gastil, and J. Lillegraven, eds., Geology of peninsular California, American Association of Petroleum Geologists, Pacific Section, p. 20-59.

Alsleben, H., and S. R. Paterson, 2003, Unraveling displacement fields in arcs: An example from the Peninsular Ranges batholith: Geological Society of America Abstracts with Programs, v. 35, p. 73.

Anderson, C. L., 1991, Zircon uranium-lead isotopic ages of the Santiago Peak Volcanics and spatially-related plutons of the Peninsular Ranges batholith, southern California: M.S. Thesis, San Diego State University, San Diego, California, 111 p.

Armijo, R., and F. Suarez-Vidal, 1981, Neotectonics of northern Baja California: Geological Society of America Abstracts with Programs, v. 13, p. 42.

Armstrong, F. C., and S. S. Oriel, 1965, Tectonic development of Idaho-Wyoming thrust belt: American Association of Petroleum Geologists Bulletin, v. 49, p. 1,847-1,866.

Atwater, T., 1970, Implications of plate tectonics for the Cenozoic tectonic evolution of western North America: Geological Society of America Bulletin, v. 81, p. 3513-3536.

Balch, D. C., S. H. Barlting, and P. L. Abbott, 1984, Volcaniclastic strata of the Upper Jurassic Santiago Peak Volcanics, San Diego, California, *in* J. K. Crouch, and S. B. Bachman, eds., Tectonics and sedimentation along the California margin, Los Angeles, California, Society of Economic Paleontologist and Mineralogists, Pacific Section, p. 157-170.

Beggs, J. M., 1984, Volcaniclastic rocks of the Alisitos Group, Baja California, Mexico, *in* V. Frizzell, Jr., ed., Geology of the Baja California Peninsula, Society of Economic Paleontologists and Mineralogists, Pacific Section, p. 43-52.

Boles, J. R., and C. A. Landis, 1984, Jurassic sedimentary mélange and associated facies, Baja California, Mexico: Geological Society of America Bulletin, v. 95, p. 513-521.

Boulter, C. A., 1976, sedimentary fabrics and their relation to strain-analysis methods: Geology, v. 4, p. 141-146.

Bourdon, B., S. P. Turner, and C. J. Allegre, 1999, Melting dynamics between the Tonga-Kermadec island arc inferred from 231Pa-235U systematics: Science, v. 286, p. 2491-2493.

Brandon, M. T., M. K. Roden-Tice, and J. I. Garver, 1998, Late Cenozoic exhumation of the Cascadia accretionary wedge in the Olympic Mountains, northwest Washington state: Geological Society of America Bulletin, v. 110, p. 985-1009.

Buch, I. P., and M. P. Delattre, 1993, Permian and Lower Triassic stratigraphy along the 30th parallel, eastern Baja California Norte, Mexico, *in* R. G. Gastil, and R. H. Miller, eds., The pre-batholithic stratigraphy of peninsular California, p. 77-90.

Busby, C., D. Smith, W. Morris, and B. Fackler-Adams, 1998, Evolutionary model for convergent margins facing large ocean basins: Mesozoic Baja California, Mexico: Geology, v. 26, p. 227-230.

Bushee, J., J. Holden, B. Geyer, and R. G. Gastil, 1963, Lead-alpha dates for some basement rocks of southwestern California: Geological Society of America Bulletin, v. 74, p. 803-806.

Campa, M. F., and P. J. Coney, 1981, Tectono-stratigraphic terranes and mineral resource distributions in Mexico: Canadian Journal of Earth Sciences, v. 20, p. 1040-1051.

Campbell, M., and J. Crocker, 1993, Geology west of the Canal de Las Ballenas, Baja California, Mexico, *in* R. G. Gastil, and R. H. Miller, eds., The pre-batholithic stratigraphy of peninsular California, p. 61-76.

Carrasco, A. P., D. L. Kimbrough, and C. T. Herzig, 1994, Facies analysis of the Early Cretaceous Santiago Peak Volcanics in eastern San Diego, California: Geological Society of America Abstracts with Programs, v. 26, p. 43.

Carrasco, A. P., D. L. Kimbrough, and C. T. Herzig, 1995, Cretaceous arc-volcanic strata of the western Peninsular Ranges: comparison of the Santiago Peak Volcanics and Alisitos Group: Abstracts of Peninsular Geological Society International Meeting on Geology of the Baja California Peninsula, v. III, p. 19.

Carrasco, A. P., D. L. Kimbrough, C. T. Herzig, and G. L. Meeth, 1993, Discovery of accretionary lapilli in the Santiago Peak Volcanics of southern and Baja California, *in* P. L. Abbott, E. M. Sangines, and M. A. Rendina, eds., Geologic investigations in Baja California, Santa Ana, California, South Coast Geological Society, p. 145-150.

Carrollo, G. F., and M. J. Walawender, 1993, Geochemistry and petrography of leucogranite plutons from the western zone of the Peninsular Ranges batholith, San Diego, California, *in* P. L. Abbott, E. M. Sangines, and M. A. Rendina, eds., Geologic investigations in Baja California, Santa Ana, California, South Coast Geological Society, p. 151-162.

Chadwick, B., 1987, The geology, petrography, geochemistry, and geochronology of the Tres Hermanos-Santa Clara region, Baja California, Mexico: M.S. Thesis, San Diego State University, San Diego, California, 601 p.

Chavez-Cabello, G., 1998, Ascent mechanisms, emplacement and magmatic evolution of several plutons located on the western side fo the Sierra San Pedro Martir, Baja California, Mexico: M.S. Thesis, CICESE, Ensenada, Baja California, Mexico, 165 p.

Coward, M. P., and P. R. James, 1974, The deformation patterns of two Archaean greenstone belts in Rhodesia and Botswana: Precambrian Research, v. 1, p. 235-258.

Criscione, J. L., T. E. Davis, and P. Ehlig, 1978, The age of sedimentation/diagenesis for the Bedford Canyon Formation and Santa Monica Formation in southern California - A Rb/Sr evaluation, *in* D. G. Howell, and K. A. McDougall, eds., Mesozoic paleogeography of the western United States, Society of Economic Paleontologists and Mineralogists, Pacific Section, p. 385-396.

Curtis, C. D., S. R. Lipshie, G. Oerel, and M. J. Pearson, 1980, Clay orientation in some Upper Carboniferous mudrocks, its relationship to quartz content and some inferences about fissility, porosity and compaction: Sedimentology, v. 27, p. 333-339.

Damon, P. E., M. Shafiqullah, and K. F. Clark, 1983, Geochronology of hte porphyry copper deposits and related mineralization of Mexico: Canadian Journal of Earth Sciences, v. 20, p. 1052-1071.

Davis, T. E., and R. G. Gastil, 1993, Whole-rock Rb/Sr isochrons of fine-grained clastic rocks in peninsular California, *in* R. G. Gastil, and R. H. Miller, eds., The prebatholithic stratigraphy of peninsular California, Boulder, Colorado, Geological Society of America, p. 157-158.

DePaolo, D. J., 1981, A neodymium and strontium isotopic study of the Mesozoic calc-alkaline granitic batholiths of the Sierra Nevada and Peninsular Ranges, California: Journal of Geophysical Research, v. 86, p. 10,470-10,488.

Dewey, J. F., 1977, Suture zone complexities: a review: Tectonophysics, v. 40, p. 53-67.

Dickinson, W. R., and T. F. Lawton, 2001, Carboniferous to Cretaceous assembly and fragmentation of Mexico: Geological Society of America Bulletin, v. 113, p. 1,142-1,160.

Ducea, M., 2001, The California arc: Thick granitic batholiths, eclogite residues, lithospheric-scale thrusting, and magmatic flare-ups: GSA Today, v. 11, p. 4-10.

Dunnet, D., and A. W. B. Siddans, 1971, Non-random sedimentary fabrics and their modification by strain: Tectonophysics, v. 12, p. 307-325.

Elliott, D., 1970, Determination of finite strain and initial shape from deformed elliptical objects: Geological Society of America Bulletin, v. 81, p. 2221-2236.

Engebretson, D. C., Cox, A., and Gordon, R.G., 1985, Relative motions between oceanic and continental plates in the Pacific basin: Geological Society of America Special Paper, v. 206, p. 1-59.

Fackler-Adams, B., 1997, Volcanic and sedimentary facies, processes, and tectonics of intra-arc basins: Jurassic continental arc of California and Cretaceous oceanic arc of Baja California: Ph.D. thesis, University of California at Santa Barbara, Santa Barbara, California, 248 p.

Fackler-Adams, B. N., and C. J. Busby, 1998, Structural and stratigraphic evolution of extensional oceanic arcs: Geology, v. 26, p. 735-738.

Fife, D. L., J. A. Minch, and P. J. Crampton, 1967, Late Jurassic age of the Santiago Peak Volcanics, California: Geological Society of America Bulletin, v. 78, p. 229-304.

Gans, P. B., G. A. Mahood, and E. R. Schermer, 1989, Synextensional magmatism in the Basin and Range province; a case study from the eastern Great Basin: Boulder, Colorado, Geological Society of America Special Paper 233, 60 p.

Gastil, R. G., 1983, Mesozoic and Cenozoic granitic rocks of southern California and western Mexico, *in* R. J.A., ed., Mesozoic and Cenozoic granitic rocks of southern California and western Mexico, p. 265-275.

Gastil, R. G., 1993, Prebatholithic history of Peninsular California, *in* R. G. Gastil, and R. H. Miller, eds., The Prebatholithic Stratigraphy of Peninsular California, p. 145-156.

Gastil, R. G., C. K. Diamond, M. J. Walawender, M. Marshal, C. Boyles, and B. Chadwick, 1990, The problem of the magnetite/ilmenite boundary in southern and Baja California, *in* J. L. Anderson, ed., The Nature and Origin of Cordilleran Magmatism, Boulder, CO, Geological Society of America, p. 19-32.

Gastil, R. G., and M. S. Girty, 1993, A reconnaissance U-Pb study of detrital zircon in sandstones of peninsular California and adjacent areas, *in* R. G. Gastil, and R. H. Miller, eds., The Prebatholithic Stratigraphy of Peninsular California, p. 135-144.

Gastil, R. G., and R. H. Miller, 1983, Prebatholithic paleogeography of peninsular California and adjacent Mexico, *in* V. A. Grizzel, ed., Geology of the Baja California Peninsula, Society of Economic Paleontologists and Mineralogists, Pacific Section, p. 9-16.

Gastil, R. G., G. J. Morgan, and D. Krummenacher, 1981, The tectonic history of peninsular California and adjacent Mexico, *in* W. G. Ernst, ed., The geotectonic development of California, Englewood Cliffs, New Jersey, Prentice-Hall, p. 284-306.

Gastil, R. G., R. Phillips, and E. Allison, 1975, Reconnaissance geology of the State of Baja California: Geological Society America Memoir 140, p. 170.

Gehrels, G. E., J. H. Stewart, and K. B. Ketner, 2002, Cordilleran-margin quartzites in Baja California -- Implications for tectonic transport: Earth and Planetary Science Letters, v. 199, p. 201-210.

Germinario, M., 1993, The early Mesozoic Julian Schist, Julian, California, *in* R. G. Gastil, and R. H. Miller, eds., The prebatholithic stratigraphy of Peninsular California, Boulder, Colorado, Geological Society of America, p. 107-118.

Girty, G. H., C. N. Thomson, M. S. Girty, J. Miller, and K. Bracchi, 1993, The Cuyamaca-Laguna Mountains shear zone, Late Jurassic plutonic rocks and Early Cretaceous extension, Peninsular Ranges, southern California, *in* P. L. Abbott, E. M. Sangines, and M. A. Rendina, eds., Geologic Investigations in Baja California, Mexico, South Coast Geological Society, p. 173-181.

Glazner, A. F., J. E. Nielson, K. A. Howard, and D. M. Miller, 1986, Correlation of the Peach Spring Tuff; a large-volume Miocene-ignimbrite-sheet in California and Arizona: Geology, v. 14, p. 840-843.

Goetz, C. W., 1989, Geology of the Rancho El Rosarito area, Baja California Mexico: Evidence for latest Albian Compression along a terrane boundary in the Peninsular Ranges: M.S. thesis, San Diego State University, San Diego, CA, 134 p.

Gorzolla, Y., 1988, Geochemistry and petrography of the Santiago Peak Volcanics, Santa Margarita and Santa Ana Mountains, southern California: M.S. Thesis, San Diego State University, San Diego, California, 145 p.

Gradstein, F. M., F. P. Agterberg, J. G. Ogg, J. Hardenbol, P. van Veen, J. Thierry, and Z. Huang, 1994, A Mesozoic time scale: Journal of Geophysical Research, v. 99, p. 24,051-24,074.

Griffith, R., and J. Hoobs, 1993, Geology of the southern Sierra Calamajue, Baja California Norte, Mexico, *in* R. G. Gastil, and R. H. Miller, eds., The Prebatholithic Stratigraphy of Peninsular California, p. 43-60.

Gromet, L. P., and L. T. Silver, 1987, REE variations across the Peninsular Ranges batholith: Implications for batholithic petrogenesis and crustal growth in magmatic arcs: Journal of Petrology, v. 28, p. 75-125.

Hall, C. A., 1991, Geology of the Point Sur-Lopez Point region, Coast Ranges, California: A part of the Southern California allochthon: Geological Society of America Special Paper, v. 266, p. 40 p.

Hanna, M. A., 1926, Geology of the La Jolla quadrangle, California: University of California Department of Geological Sciences Bulletin, v. 16, p. 187-246.

Hawkins, J. W., 1970, Metamorphosed Late Jurassic andesites and dacites of the Tijuana-Tecate area, California, Pacific slope geology of northern Baja California and adjacent alta California, Pacific section, American Association of Petroleum Geologists/Society of Economic Paleontologists and Mineralogists/ Society of Exploration Geophysicist, p. 25-29.

Herzig, C. T., 1991, Petrogenetic and tectonic development of the Santiago Peak Volcanics, northern Santa Ana Mountains, California: Ph.D. thesis, U.C. Riverside, Riverside, California, 376 p.

Holst, T. B., 1982, The role of initial fabric on strain determination from deformed ellipsoidal objects: Tectonophysics, v. 82, p. 329-350.

Hossack, J. R., 1968, Pebble deformation and thrusting in the Bygdin area (southern Norway): Tectonophysics, v. 5, p. 315-339.

Hudleston, P., 1999, Strain compatibility and shear zones: is there a problem?: Journal of Structural Geology, v. 21, p. 923-932.

Imlay, R. W., 1963, Jurassic fossils from southern California: Journal of Paleontology, v. 38, p. 97-107.

Imlay, R. W., 1964, Middle Jurassic and Upper Jurassic fossils from southern California: Journal of Paleontology, v. 38, p. 505-509.

Irving, E., P. J. Wynne, D. J. Thorkelson, and P. Schiarizza, 1996, Large (1000 to 4000 km) northward movements of tectonic domains in the northern Cordillera, 83 to 45 Ma: Journal of Geophysical Research, v. 101, p. 17901-17916.

Johnson, S. E., J. M. Fletcher, C. M. Fanning, S. R. Paterson, R. H. Vernon, and M. C. Tate, 2003, Structure and emplacement of the San Jose tonalite pluton, Peninsular Ranges batholith, Baja California, Mexico: Journal of Structural Geology, v. 25.

Johnson, S. E., S. R. Paterson, and C. M. Tate, 1999b, Structure and emplacement history of a multiple-center, cone-sheet-bearing ring complex: The Zarza intrusive complex, Baja California, Mexico: Geological Society of America Bulletin, v. 111, p. 607-619.

Johnson, S. E., M. C. Tate, and C. M. Fanning, 1999a, New geologic mapping and SHRIMP U-Pb data in the Peninsular Ranges batholith, Baja California, Mexico: Evidence of a suture?: Geology, v. 27, p. 743-746.

Kimbrough, D. L., R. G. Gastil, P. K. Garrow, M. Grove, J. Aranda-Gomez, and J. A. Perez-Venzor, 2002, A potential correlation of plutonic suites from the Los Cabos Block and Peninsular Ranges batholith: VI International Meeting on Geology of the Baja California Peninsula, p. 9.

Kimbrough, D. L., and C. T. Herzig, 1994, Late Jurassic/Early Cretaceous deformation in the prebatholithic basement of the Cretaceous Peninsular Ranges batholith magmatic arc- an expression of the J-2 cusp?: Geological Society of America Abstracts with Programs, v. 26, p. 63.

Kimbrough, D. L., D. P. Smith, J. B. Mahoney, T. E. Moore, M. Grove, R. G. Gastil, A. Ortega-Rivera, and C. M. Fanning, 2001, Forearc-basin sedimentary response to rapid Late Cretaceous batholith emplacement in the Peninsular Ranges of southern and Baja California: Geology, v. 29, p. 491-494.

Klinger, M., J. B. Mahoney, and D. L. Kimbrough, 2000, Whole rock geochemistry of conglomerate clasts from Valle Group Cretaceous forearc basin strata, Baja California: Geological Society of America Abstracts with Programs, v. 32, p. 22.

Kopf, C. F., and D. L. Whitney, 1999, Variation in metamorphic grade across a possible inter-arc convergent boundary, Peninsular Ranges, Mexico: Geological Society of America Abstracts with Programs, v. 31, p. 294.

Lamb, T. N., 1970, Fossiliferous Triassic metasedimentary rocks near Sun City, Riverside County, California: Geological Society of America Abstracts with Programs, v. 2, p. 110-111.

Larsen, E. S., 1948, Batholith and associated rocks of Corona, Elsinore, and San Luis Rey quadrangles, southern California: Geological Society of America, v. Memoir 29, p. 182.

Lash, G. G., 1985, Accretion-related deformation of an ancient (early Paleozoic) trench-fill deposit, central Appalachian orogen: Geological Society of America Bulletin, v. 96, p. 1167-1178.

Leedom, S., 1967, A stratigraphic study of the Alisitos Formation near San Vicente, Baja California, Mexico: Senior Thesis, San Diego State University, San Diego, California, 21 p.

Leeson, R. T., 1989, Fabric analysis of the Cuyamaca-Laguna Mountains shear zone: M.S. Thesis, San Diego State University, San Diego, CA, 136 p.

Legg, M. R., O. V. Wong, and F. Suarez-Vidal, 1991, Geologic structure and tectonics of the inner continental borderland of northern Baja California, *in* J. P. E. Dauphin, and B. R. T. Simoneit, eds., The Gulf and Peninsular Province of the Californias, Tulsa, OK, p. 145-177.

Lothringer, C. J., 1993, Allochthonous Ordovician strata of Rancho San Marcos, Baja California Norte, Mexico, *in* R. G. Gastil, and R. H. Miller, eds., The prebatholithic stratigraphy of peninsular California, Boulder, Colorado, Geological Society of America, p. 11-22.

Lovera, O. M., M. Grove, D. L. Kimbrough, and P. L. Abbott, 1999, A method for evaluating basement exhumation histories from closure age distributions of detrital minerals: Journal of Geophysical Research, v. 104, p. 29,419-29,438.

Ludwig, K. R., 2001, Isoplot/Ex, rev. 2.49: Berkely Geochronology Center, Special Publication, v. 1A: Berkeley, CA, 56 p.

Lund, K., and L. W. Snee, 1988, Metamorphism, structural development, and age of the continent: island arc juncture in west-central Idaho, *in* W. G. Ernst, ed., Metamorphism and crustal evolution of the western United States, Englewood Cliffs, New Jersey, Prentice-Hall, p. 296-331.

Marsh, B. D., 1979, Island-arc volcanism: American Scientist, v. 67, p. 161-172.

McCaffrey, R., P. C. Zwick, Y. Bock, L. Prawirodirdjo, J. F. Genrich, C. W. Stevens, S. O. Puntodewo, and C. Subarya, 2000, Strain partitioning during oblique plate convergence in northern Sumatra: Geodetic and seismologic constraints and numerical modeling: Journal of Geophysical Research, v. 105, p. 28,363-28,276.

McDonough, W. F., and S. S. Sun, 1995, The Composition of the Earth: Chemical Geology, v. 120, p. 223-253.

Meeth, G., 1993, Stratigraphy and petrology of the Santiago Peak Volcanics east of La Mision, Baja California: B.S. thesis, San Diego State University, San Diego, CA, 16 p.

Miller, D. M., and G. Oertel, 1979, Strain determination from the measurement of pebble shapes: a modification: Tectonophysics, v. 55, p. T11-T13.

Molyneux, S. J., and D. H. W. Hutton, 2000, Evidence for significant granite space creation by the ballooning mechanism: The example of the Ardara pluton, Ireland: Geological Society of America Bulletin, v. 112, p. 1543-1558.

Moran, A. I., 1976, Allochthonous carbonate debris in Mesozoic flysch deposits in Santa Ana Mountains, California: American Association of Petroleum Geologists Bulletin, v. 60, p. 2038-1043.

Moscoso, B. A., 1967, A thick section of "flysch" in the Santa Ana Mountains, southern California: M.S. Thesis, San Diego State University, San Diego, CA, 106 p.

Nicholls, I. A., and A. E. Ringwood, 1973, Effect of water on olivine stability in tholeiites and the production of silica saturated magmas in the island arc environment: Journal of Geology, v. 81, p. 285-300.

Oertel, G., 1970, Deformation of a slaty, lapillar tuff in the Lake District, England: Geological Society of America Bulletin, v. 81, p. 1173-1188.

Oertel, G., 1981, Strain estimation from scattered observation in an inhomogeneously deformed domain of rocks: Tectonophysics, v. 77, p. 133-150.

Oertel, G., 1983, The relationship of strain and preferred orientation of phyllosilicate grains in rocks - a review: Tectonophysics, v. 100, p. 413-447.

Paterson, R. S., and H. Yu, 1994, Primary fabric ellipsoids in sandstones: implications for depositional processes and strain analysis: Journal of Structural Geology, v. 16, p. 505-517.

Paterson, S. R., H. Yu, and G. Oertel, 1995, Primary and tectonic fabric intensities in mudrocks: Tectonophysics, v. 247, p. 105-119.

Peterson, G. L., 1967, Structure of the late Mesozoic pre-batholithic rocks north of San Diego, California, v. Special Paper 115: Boulder, Colorado, Geological Society of America, 347 p.

Pfiffner, O. A., 1980, Strain analysis in folds (Infrahelvetic complex, central Alps): Tectonophysics, v. 61, p. 337-362.

Phillips, J. R., 1993, Stratigraphy and structural setting of the mid-Cretaceous Olvidada Formation, Baja California Norte, Mexico, *in* R. G. Gastil, and R. H. Miller, eds., The Prebatholithic Stratigraphy of Peninsular California, p. 97-106.

Premo, W. R., D. M. Morton, L. W. Snee, C. M. Fanning, and N. D. Naeser, 1998, Isotopic ages, cooling histories, and magmatic origins for Mesozoic tonalitic plutons from the northern Peninsular Ranges batholith, southern California: Geological Society of America Abstracts with Program, v. 30, p. 59-60.

Ramsay, J. G., 1967, Folding and fracturing of rocks: New York, NY, McGraw-Hill, 568 p.

Reed, B. C., 1992, Petrology and eruptive setting of the Santiago Peak Volcanics, in the Mission Gorge-San Diego area San Diego, California: M.S. Thesis, San Diego State University, San Diego, California.

Reed, J., 1993, Rancho Vallecitos Formation, Baja California Norte, Mexico, *in* R. G. Gastil, and R. H. Miller, eds., The Prebatholithic Stratigraphy of Peninsular California, p. 119-134.

Reed, R. G., 1967, Stratigraphy and structure of the Alisitos Formation near El Rosario, Baja California, Mexico: M.S. thesis, San Diego State University, San Diego, CA, 118 p.

Roberts, B., and A. W. B. Siddans, 1971, Fabric studies in the Llwyd Mawr ignimbrite, Caernarvonshire, North Wales: Tectonophysics, v. 12, p. 283-306.

Rockwell, T. K., D. R. Muhs, G. L. Kennedy, M. E. Hatch, S. H. Wilson, and R. E. Klinger, 1989, uranium-series ages, faunal correlations and tectonic deformation of marine terraces within the Agua Blanca Fault zone at Punta Banda, northern Baja California, Mexico, *in* P. L. Abbott, ed., Geologic studies in Baja California, Los Angeles, Ca, S.E.P.M., Pacific Section, p. 1-16.

Sample, J. C., and D. M. Fisher, 1986, Duplex accretion and underplating in an ancient accretionary complex, Kodiak Islands, Alaska: Geology, v. 14, p. 160-163.

Sample, J. C., and J. C. Moore, 1987, Structural style and kinematics of an underplated slate belt, Kodiak and adjacent islands, Alaska: Geological Society of America Bulletin, v. 99, p. 7-20.

Schaaf, P., D. Moran-Zenteno, and M. D. S. Hernandez-Bernal, 1995, Paleogene continental margin truncation in southwestern Mexico: Geochronological evidence: Tectonics, v. 14, p. 1,339-1,350.

Schmidt, K. L., 2000, Investigations of arc processes: relationships among deformation magmatism, mountain building, and the role of crustal anisotropy in the evolution of the Peninsular Ranges batholith, Baja California: Ph.D. thesis, University of Southern California, Los Angeles, CA, 324 p.

Schmidt, K. L., and S. R. Paterson, 2003, A doubly vergent fan structure in the Peninsular Ranges batholith: Transpression or local complex flow around a continental margin buttress?: Tectonics, v. 21, p. 14-1-14-19.

Schoellhamer, J. E., J. G. Vedder, R. F. Yerkes, and D. M. Kinney, 1981, Geology of the northern Santa Ana Mountains, U.S. Geological Survey, p. 109.

Schroeder, J. E., 1967, Geology of a portion of the Ensenada Quadrangle Baja California, Mexico: M.S. thesis, San Diego State University, San Diego, CA, 65 p.

Schwartz, H. P., 1960, Geology of the Winchester-Hemet area, Riverside County, California: Ph.D. Dissertation thesis, California Institute of Technology, Pasadena, California, 317 p.

Sedlock, R. L., and Y. Isozaki, 1990, Lithology and biostratigraphy of Franciscan-like chert adn associated rocks in west-central Baja California, Mexico: Geological Society of America Bulletin, v. 102, p. 852-864.

Sedlock, R. L., F. Ortega-Gutierrez, and R. C. Speed, 1993, Tectonostratigraphic Terranes and Tectonic Evolution of Mexico, v. Special Paper 278: Boulder, Colorado, The Geological Society of America, 153 p.

Seymour, D. B., and C. A. Boulter, 1979, Tests of computerized strain analysis methods by the analysis of simulated deformation of natural unstrained sedimentary fabrics: Tectonophysics, v. 58, p. 221-236.

Shimamoto, T., and Y. Ikeda, 1976, A simple algebraic method for strain estimation from deformed ellipsoidal objects. 1. basic theory: Tectonophysics, v. 36, p. 315-337.

Silberling, N. J., J. E. Schoellhamer, C. H. Gray, and R. W. Imlay, 1961, Upper Jurassic fossil from the Bedford Canyon Formation, southern California: Amerinca Association of Petroleum Geologists Bulletin, v. 4745, p. 1,746-1,765.

Silver, L. T., and B. W. Chappell, 1988, The Peninsular Ranges Batholith: an insight into the evolution of the Cordilleran batholiths of southwestern North America: Transactions of the Royal Society of Edinburgh, v. 79, p. 105-121.

Silver, L. T., G. G. Stehli, and C. R. Allen, 1963, lower Cretaceous pre-batholithic rocks of northern Baja California, Mexico: Bulletin of the American Association of Petroleum Geologists, v. 47, p. 2054-2059.

Silver, L. T., H. P. J. Taylor, and B. W. Chappell, 1979, Some petrological, geochemical, and geochronological observations of the Peninsular Ranges batholith near the international border of the U.S.A. and Mexico, *in* P. L. Abbott, and V. R. Todd, eds., Mesozoic Crystalline Rocks: Peninsular Ranges Batholith and Pegmatites, Point Sal Ophialite, p. 83-110.

Stacey, J. S., and J. D. Kramers, 1975, Approximation of terrestrial lead isotpe evolution by a two-stage model: Earth and Planetary Science Letters, v. 26, p. 207-221.

Suarez-Vidal, F., 1986, Alisitos Formation calcareous facies: Early Cretaceous episode of tectonic calm: American Associates of Petroleum Geologists Bulletin, v. 70, p. 480.

Suarez-Vidal, F., 1993, The Aptian-Albian on the west coast of hte state of Baja California, a mixture of marine environments, *in* P. L. Abbott, E. M. Sangines, and M. A. Rendina, eds., Geologic investigations in Baja California, Santa Ana, California, South Coast Geological Society, p. 125-138.

Suarez-Vidal, F., R. Armijo, G. Morgan, P. Bodin, and R. G. Gastil, 1991, Framework of recent and active faulting in northern Baja California, *in* J. P. E. Dauphin, and B. R. T. Simoneit, eds., The Gulf and Peninsular Province of the Californias, Tulsa, OK, p. 285-300.

Suppe, J., 1970, Offset of late Mesozoic basement terrains by the San Andreas fault system: Geological Society of America Bulletin, v. 81, p. 3,253-3,258.

Sutherland, M., P. H. Wetmore, C. Herzig, and S. R. Paterson, 2002, The Early Cretaceous Santiago Peak arc: A continental margin arc built on the North American Triassic-Jurassic accretionary prism of southern and Baja California: Geological Society of America Abstracts with Programs, v. 34, p. 43.

Tanaka, H., T. E. Smith, and C. H. Huang, 1984, The Santiago Peak volcanic rocks of the Peninsular Ranges batholith, southern California; volcanic rocks associated with coeval gabbros: Bulletin Volcanologique, v. 47, p. 153-171.

Tardy, M., H. Lapierre, C. Freydier, C. Coulon, J. B. Gill, B. Mercier de Lepinay, C. Beck, J. Martinez, O. Talavera, E. Ortiz, G. Stein, J. L. Bourdier, and M. Yta, 1994, The Guerrero suspect terrane (western Mexico) and coeval arc terranes (the Greater Antilles and the Western Cordillera of Colombia): a late Mesozoic intra-oceanic arc accreted to cratonal America during the Cretaceous: Tectonophysics, v. 230, p. 49-73.

Tate, M. C., and S. E. Johnson, 2000, Subvolcanic and deep-crustal tonalite genesis beneath the Mexican Peninsular Ranges: Journal of Geology, v. 108, p. 720-728.

Tate, M. C., M. D. Norman, S. E. Johnson, C. M. Fanning, and J. L. Anderson, 1999, Generation of tonalite and trondhjemite by subvolcanic fractionation and partial melting in the Zarza Intrusive Complex, western Peninsular Ranges batholith, northwestern Mexico: Journal of Petrology, v. 40, p. 983-1,010.

Taylor, H. P. J., and L. T. Silver, 1978, Oxygen isotope relationships in plutonic igneous rocks of the Peninsular Ranges batholith, southern and Baja California, *in* R. E. Zzartman, ed., Short papers of the fourth international conferences on geochronology, p. 423-426.

Thomson, C. N., 1994, Tectonic implications of Jurassic magmatism and Early Cretaceous mylonitic deformation, Cuyamaca-Laguna Mountains shear zone, southern California: M.S. thesis, San Diego State University, San Diego, CA, 85 p.

Thomson, C. N., and G. H. Girty, 1994, Early Cretaceous intra-arc ductile strain in Triassic-Jurassic and Cretaceous continental margin arc rocks, Peninsular Ranges, California: Tectonics, v. 13, p. 1,108-1,119.

Tobisch, O. T., R. S. Fiske, S. Sacks, and D. Taniguchi, 1977, Strain in metamorphosed volcaniclastic rocks and its bearing on the evolution of orogenic belts: Geological Society of America Bulletin, v. 88, p. 23-40.

Todd, V. R., B. G. Erskine, and D. M. Morton, 1988, Metamorphic and tectonic evolution of the northern Peninsular Ranges batholith, *in* W. G. Ernst, ed., metamorphism and Crustal Evolution of the Western United States, Prentice-Hall Inc., p. 894-937.

Walawender, M. J., G. H. Girty, M. R. Lombardi, D. Kimbrough, M. S. Girty, and C. Anderson, 1991, A synthesis of recent work in the Peninsular Ranges batholith, *in* M. J. Walawender, and B. B. Hanan, eds., Geological Excursions in southern California and Mexico, p. 297-318.

Wetmore, P. H., K. L. Schmidt, S. R. Paterson, and C. Herzig, 2002, Tectonic implications for the along-strike variation of the Peninsular Ranges batholith, southern and Baja California: Geology, v. 30, p. 247-250.

APPENDIX A: ANALYTICAL PROCEEDURES

Sample preparations

A small suite of plutonic and sedimentary samples were collected for a reconnaissance geochemical and geochronologic study. Zircons were separated from eight (8) samples including two sandstone samples that were sent to Dr. George Gehrels at the University of Arizona, two plutonic samples that were sent to Apatite to Zircon, Inc. in Viola, Idaho, and four additional plutonic samples that were processed by Wetmore at the University of Arizona. In each case, samples were crushed using traditional metal jaw crushers and heavy grains were separated through the use of a Wilfley table. After samples were dried they were immersed in heavy liquid (MeI, density 3.3 g/cm^3) and only the heaviest (i.e., that which sank) portion was extracted. The remaining sample was then passed through a Frantz magnetic separator multiple times and only the least magnetic split was collected. Each sample was then inspected under a microscope to assess purity and all were found to be greater than ninety percent zircon. To further ensure purity, individual zircon crystals were picked for analysis.

Geochemical analyses were completed on seven (7) samples, all plutonics. For each sample thin sections were cut and inspected for signs of alteration and weathering. The selected samples lack obvious signs of alteration. All samples were crushed using a small steel chipmonk and powdered in an agate shatterbox at the University of Southern California.

Major and trace element analysis of whole rock samples

Whole rock analysis for major and trace elemental compositions was completed by Actlabs at their facilities in Ontario, Canada. There, a 1 g sample was digested with aqua regia and diluted to 250 ml volumetrically. Samples and standards were analyzed on a Thermo Jarrell Ash Enviro II simultaneous and sequential ICP.

Radiogenic isotopic analysis of whole rock samples

Sample powders were spiked with ^{87}Rb, ^{84}Sr, and mixed ^{147}Sm-^{150}Nd tracers. Dissolution of the spiked samples for isotopic analyses was performed in screw-cap Teflon beakers using HF-HNO_3 (on hot plates) and HF-$HClO_3$ mixtures (in open beakers at room temperature). A few garnet separates were subjected to several, up to 5 dissolution steps before becoming residue-free. The samples were taken in 1 N HCl and any undissolved residue was attacked in the same way. Separation of the Rb, Sr, and the bulk of the REE was achieved via HCl elution in cation columns. Separation of Sm and Nd was carried out using a LNSpec® resin. The highest procedural blanks measured during the course of this study were: 11 pg Rb, 180 pg Sr, 5 pg Sm, and 18 pg Nd.

Isotopic analyses for Sr and Nd, as well as isotope dilution analyses of Rb, Sr, Sm, and Nd were performed at Caltech using a VG multiple collector mass spectrometer. The isotopic compositions of Sr and Nd were determined on the same spiked samples. The filament loading and mass spectrometric analysis procedures were similar to the ones previously described by Pickett and Saleeby (1994). The Sr isotopic ratios were normalized to $^{86}Sr/^{88}Sr = 0.1194$, whereas the Nd isotopic ratios were normalized to $^{146}Nd/^{144}Nd = 0.7219$. Estimated analytical $\pm 2\sigma$ uncertainties are: $^{87}Rb/^{86}Sr = 0.55\%$,

$^{87}Sr/^{86}Sr$= 0.0015%, $^{147}Sm/^{144}Nd$= 0.8%, and $^{143}Nd/^{144}Nd$= 0.002%. External reproducibility, based on the range of multiple runs of standard NBS987 (for Sr) and LaJolla Nd (for Nd) are estimated to be ±0.000014 for Sr, and ± 0.00001 for Nd. Replicate analyses of two samples analyzed in this study (G36WR and BC207 WR) indicate similar reproducibility. The grand means of isotopic ratios were corrected by an off-line manipulation program, which adjusts for the spike contributions to both the fractionation correction and each ratio, and performs isotope dilution calculations.

U-Pb geochronologic analyses of zircon

U-Pb geochronology of zircons was conducted by laser ablation multicollector inductively coupled plasma mass spectrometry (LA-MC-ICPMS). The analyses involve ablation of zircon with a New Wave DUV193 Excimer laser (operating at a wavelength of 193 nm) using a spot diameter of 25 to 50 microns. The ablated material is carried in argon gas into the plasma source of a Micromass Isoprobe, which is equipped with a flight tube of sufficient width that U, Th, and Pb isotopes are measured simultaneously. All measurements are made in static mode, using Faraday detectors for ^{238}U, ^{232}Th, $^{208-206}Pb$, and an ion-counting channel for ^{204}Pb. Ion yields are ~1 mv per ppm. Each analysis consists of one 20-second integration on peaks with the laser off (for backgrounds), 20 one-second integrations with the laser firing, and a 30 second delay to purge the previous sample and prepare for the next analysis. The ablation pit is ~20 microns in depth, with vertical walls and a nearly flat floor.

For each analysis, the errors in determining $^{206}Pb/^{238}U$ and $^{206}Pb/^{204}Pb$ result in a measurement error of ~1-2% (at 2-sigma level) in the $^{206}Pb/^{238}U$ age. The errors in

measurement of $^{206}Pb/^{207}Pb$ are much larger due to the low intensity of the ^{207}Pb signal. Age interpretations in this study are accordingly based entirely on $^{206}Pb/^{238}U$ ages.

Common Pb correction is made by using the measured ^{204}Pb and assuming an initial Pb composition from Stacey and Kramers (1975) (with uncertainties of 1.0 for $^{206}Pb/^{204}Pb$ and 0.3 for $^{207}Pb/^{204}Pb$). Our measurement of ^{204}Pb is unaffected by the presence of ^{204}Hg because backgrounds are measured on peaks (thereby subtracting any background ^{204}Hg and ^{204}Pb), and because very little Hg is present in the argon gas.

Inter-element fractionation of Pb/U is generally <20%, whereas fractionation of Pb isotopes is generally <5%. In-run analysis of fragments of a large zircon crystal (generally every fifth measurement) with known age of 564 ± 4 Ma (2-sigma error) (G. Gehrels, unpublished data) is used to correct for this fractionation. The uncertainty resulting from the calibration correction (together with the uncertainty from decay constants and common Pb composition) is generally 3% (2-sigma) for the $^{206}Pb/^{238}U$ ages. Fractionation also increases with depth into the laser pit. The accepted isotope ratios are accordingly determined by least-squares projection through the measured values back to the initial determination.

For each sample, the $^{206}Pb/^{238}U$ ages are plotted with 1-sigma error bars (Fig. 4.13 that reflect only the error in determining $^{206}Pb/^{238}U$ and $^{206}Pb/^{204}Pb$. These ages and their errors are reported in Tables B.1 and B.2 in Appendix B. The weighted mean of the individual analyses is calculated according to Ludwig (2001), which is reported for each sample. The age of each sample, however, has additional uncertainty from the calibration correction, decay constants, and composition of common Pb. These systematic errors are

added quadratically to the measurement errors to yield the larger uncertainty for the age of each sample (Figs. 4.13).

APPENDIX B: LA-MC-ICPMS U/Pb zircon data

Tables B.1 and B.2 report the individual results of LA-MC-ICPMS U/Pb analysis on zircon crystals from sandstone samples and plutonic samples respectively. In each case NA refers to negative age value, all errors at given at the 1-sigma level, and U concentration has an uncertainty of ~25%. The decay constant for ^{235}U is $9.8485x10^{-10}$, and 137.88 for $^{238}U/^{235}U$. Isotope ratios are corrected fro Pb/U fractionation by comparison with standard zircon with an age of 564 $\pm$ 4 Ma. Initial Pb compositions interpreted from Stacey and Kramers (1975), with uncertainties of 1.0 for $^{206}Pb/^{204}Pb$, 0.3 for $^{207}Pb/^{204}Pb$, and 2.0 for $^{206}Pb/^{208}Pb$. Reported errors include systematic and random.

Table B.1. Detrital Zircon samples

		Isotopic Ratios								Apparent ages					
Crystal	(ppm)	$^{206}Pb/^{204}Pb$	$^{206}Pb/^{238}U$	±(%)	$^{207}Pb/^{235}U$	±(%)	errcorr	$^{207}Pb/^{206}Pb$	±(%)	$^{206}Pb/^{238}U$	±(Ma)	$^{207}Pb/^{235}U$	±(Ma)	$^{207}Pb/^{206}Pb$	±(Ma)
PHW 6/6/00-F															
1	206	35295	3.76825	9.54	0.27183	3.54	0.371	9.946	8.86	1550.1	61.7	1586	311.8	1634.1	82.3
2	300	101475	3.25389	8.29	0.25949	4.13	0.498	10.995	7.19	1487.2	68.6	1470.1	242.4	1445.5	68.5
3	385	13875	0.10052	10.52	0.01862	2.89	0.275	25.538	10.12	118.9	3.5	97.3	10.7	-406	132
4	473	34542	0.12828	8.56	0.02043	2.4	0.281	21.958	8.22	130.4	3.2	122.5	11.1	-27	100
5	39	734	0.09569	20.99	0.01609	3.14	0.15	23.18	20.76	102.9	3.3	92.8	20.2	-160	258
6	241	3281	0.14414	15	0.0192	3.19	0.212	18.365	14.66	122.6	3.9	136.7	21.7	390	165
7	210	12863	0.14237	18.7	0.01955	3.29	0.176	18.929	18.41	124.8	4.1	135.2	26.7	322	209
8	165	12346	0.17138	13.85	0.02218	2.44	0.176	17.842	13.64	141.4	3.5	160.6	23.8	454	151
9	236	14340	0.12456	14.71	0.02198	2.05	0.139	24.33	14.57	140.2	2.9	119.2	18.4	-281	186
10	362	4329	0.13425	13.35	0.01854	2.81	0.211	19.04	13.05	118.4	3.4	127.9	18	308	149
11	147	1513	0.12274	31.45	0.01803	3.37	0.107	20.253	31.27	115.2	3.9	117.5	38.5	166	365
12	117	2292	0.11885	30.97	0.01934	3.28	0.106	22.434	30.8	123.5	4.1	114	36.7	-79	377
13	200	3755	0.16257	14.26	0.02273	2.29	0.161	19.275	14.07	144.9	3.4	152.9	23.3	280	161
14	82	2413	0.15169	25.84	0.01966	2.98	0.115	17.874	25.67	125.5	3.8	143.4	39	450	285
15	147	2537	0.13392	13.45	0.01907	2.92	0.217	19.631	13.13	121.8	3.6	127.6	18.1	238	151
16	229	5903	0.18368	15.05	0.02021	2.98	0.198	15.169	14.76	129	3.9	171.2	27.7	804	155
17	302	4513	0.14698	16.16	0.01939	2.29	0.142	18.191	15.99	123.8	2.9	139.2	23.8	411	179
18	350	22640	0.20428	22.47	0.02081	2.18	0.097	14.044	22.37	132.8	2.9	188.7	45.6	963	228
19	134	6365	0.12093	19.1	0.0183	3.82	0.2	20.868	18.72	116.9	4.5	115.9	23.2	95	222
20	114	5413	0.16056	10.57	0.01981	4.77	0.451	17.011	9.43	126.5	6.1	151.2	17.1	559	103
21	69	6687	0.15824	16.05	0.01875	5.48	0.341	16.335	15.09	119.7	6.6	149.2	25.5	647	162
22	31	824	0.13711	14.44	0.02174	6	0.415	21.857	13.13	138.6	8.4	130.5	19.9	-16	159

Table B.1. Continued

		Isotopic Ratios								Apparent ages					
Crystal	U (ppm)	$^{206}Pb/^{204}Pb$	$^{207}Pb/^{235}U$	±(%)	$^{206}Pb/^{238}U$	±(%)	errcorr	$^{206}Pb/^{207}Pb$	±(%)	$^{206}Pb/^{238}U$ age	±(Ma)	$^{207}Pb/^{235}U$ age	±(Ma)	$^{206}Pb/^{207}Pb$ age	±(Ma)
PHW 5/19/01-A															
1	44	6307	2.71563	3.2	0.21639	2.16	0.676	10.987	2.36	1263	30.1	1332.7	84.5	1447	22.4
2	48	1571	0.11168	11.31	0.01846	2.28	0.202	22.788	11.08	118	2.7	107.5	12.7	-117.3	136.5
3	64	1769	0.13922	13.29	0.02186	2.28	0.172	21.651	13.1	139	3.2	132.3	18.6	7.4	157.6
3b	103	65538	0.80461	3.23	0.0932	2.06	0.636	15.97	2.5	574	12.3	599.4	26.1	695.2	26.6
4	52	1298	0.14127	16.8	0.02149	2.45	0.146	20.978	16.62	137	3.4	134.2	23.8	82.9	197.2
5	146	2839	0.12402	7.85	0.02074	2.72	0.347	23.055	7.36	132	3.6	118.7	9.8	-146.1	91.2
6	57	1596	0.12938	18.97	0.02077	2.65	0.14	22.138	18.78	133	3.5	123.5	24.6	-46.4	228.4
7	58	1193	0.17719	23.77	0.02802	2.1	0.088	21.802	23.67	178	3.8	165.6	41.9	-9.3	285.8
8	62	1281	0.12099	24.5	0.0224	2.66	0.109	25.532	24.35	143	3.8	116	29.7	-405.7	317.9
9	107	1433	0.36447	4.39	0.04479	2.32	0.528	16.946	3.73	283	6.7	315.5	16.1	567.5	40.6
10	57	7595	4.05713	3.28	0.27617	2.4	0.732	9.386	2.24	1572	42.7	1645.7	127	1741.2	20.5
11	45	5757	2.96315	3.73	0.24031	2.95	0.792	11.182	2.28	1388	45.6	1398.2	106.4	1413.4	21.8
12	43	577	0.1234	35.97	0.02315	5.99	0.167	25.872	35.47	148	8.9	118.1	44.1	-440.3	466.3
13	105	1338	0.14222	30.03	0.02236	2.19	0.073	21.678	29.95	143	3.2	135	42.5	4.4	360.6
14	68	892	0.16607	50.35	0.02278	2.21	0.044	18.91	50.3	145	3.2	156	81.5	323.7	571.1
15	37	712	0.08905	29.54	0.02115	2.61	0.088	32.745	29.43	135	3.6	86.6	26.4	-1104.6	446.5
16	157	21737	3.11884	3.79	0.25064	3.2	0.844	11.08	2.03	1442	51.4	1437.3	113.3	1430.8	19.4
17	65	3418	0.31185	7.95	0.04525	2.49	0.314	20.009	7.55	285	7.3	275.6	24.9	194	87.8
18	182	2529	0.10039	8.17	0.02049	2.4	0.294	28.139	7.81	131	3.2	97.1	8.3	-666.4	107.7
19	372	1442	0.12387	4.91	0.01738	2.21	0.45	19.348	4.38	111	2.5	118.6	6.2	271.5	50.2
20	87	2945	0.79287	9.88	0.0788	7.28	0.737	13.704	6.68	489	36.9	592.8	76.6	1013.2	67.7
21	3	71	1.35201	21.34	0.19499	19.27	0.903	19.885	9.17	1148	237.8	868.4	257.4	208.4	106.3
22	311	18278	3.12707	2.85	0.24892	2.03	0.712	10.976	2	1433	32.5	1439.4	86.8	1448.9	19.1
23	246	26917	4.96069	4.33	0.33075	3.82	0.883	9.193	2.03	1842	81	1812.6	197.6	1779.1	18.5
24	19	12936	13.40371	3.03	0.50673	2.22	0.734	5.213	2.06	2643	72.2	2708.5	346	2758	16.9
25	1165	10726	0.14174	5.42	0.01883	4.99	0.92	18.314	2.12	120	6.1	134.6	7.8	396.1	23.8
26	16	743	0.18053	36.71	0.02389	2.73	0.074	18.25	36.61	152	4.2	168.5	65.2	403.9	409.9
27	81	3177	0.17358	15.12	0.02306	2.15	0.142	18.317	14.97	147	3.2	162.5	26.3	395.6	167.8
28	54	1027	0.23895	15.69	0.03048	2.2	0.14	17.588	15.54	194	4.3	217.6	37.4	486	171.5

Table B.1. Continued

		Isotopic Ratios								Apparent ages					
Crystal	U (ppm)	$^{206}Pb/^{204}Pb$	$^{207}Pb/^{235}U$	±(%)	$^{206}Pb/^{238}U$	±(%)	errcorr	$^{206}Pb/^{207}Pb$	±(%)	$^{206}Pb/^{238}U$ age	±(Ma)	$^{207}Pb/^{235}U$ age	±(Ma)	$^{206}Pb/^{207}Pb$ age	±(Ma)
PHW 5/19/01-A															
29	15	2411	2.15669	4.99	0.19537	2.09	0.418	12.49	4.53	1150	26.2	1167.2	103.8	1198.6	44.7
30	161	4587	0.42359	3.93	0.05554	2.39	0.609	18.079	3.12	349	8.5	358.6	16.7	424.9	34.7
31	60	4126	0.11761	8.5	0.01567	2.8	0.329	18.375	8.03	100	2.8	112.9	10.1	388.6	90.1
32	25	612	0.10479	27.5	0.02378	2.32	0.084	31.287	27.4	152	3.6	101.2	28.8	-968.4	403.3
33	23	3812	2.30309	3.96	0.19919	2.55	0.645	11.925	3.02	1171	32.7	1213.2	88.5	1289.3	29.4
34	69	972	0.12383	13.45	0.02123	2.46	0.183	23.642	13.23	135	3.4	118.5	16.8	-208.8	166
35	32	6807	0.19782	21.46	0.03013	2.63	0.122	21	21.3	191	5.1	183.3	42.2	80.3	252.9
36	43	943	0.16188	14.94	0.02928	2.22	0.149	24.938	14.77	186	4.2	152.3	24.3	-344.5	190.5
37	63	1095	0.13477	8.72	0.02082	2.21	0.253	21.302	8.44	133	3	128.4	11.9	46.4	100.8
38	31	524	0.07643	15.71	0.01706	4.33	0.275	30.779	15.1	109	4.8	74.8	12.1	-920.4	220
39	136	17676	4.2316	4.01	0.29541	3.47	0.864	9.626	2.02	1669	65.7	1680.2	159.2	1694.7	18.6
40	152	4527	1.25496	3.77	0.11653	3.06	0.811	12.803	2.21	711	22.9	825.6	46.9	1149.5	21.9
41	74	14331	3.25415	2.98	0.25836	2.16	0.726	10.947	2.05	1481	35.9	1470.2	93.9	1453.9	19.5
42	92	21882	2.07271	5.57	0.19887	4.66	0.835	13.229	3.06	1169	59.4	1139.8	111	1084.3	30.7
43	144	15297	4.08494	4.04	0.27926	3.51	0.867	9.426	2.01	1588	62.8	1651.3	155.2	1733.3	18.5
44	13	1520	1.62168	7.31	0.1459	3.98	0.545	12.405	6.13	878	37.3	978.6	113.7	1212.1	60.3
45	138	1593	0.30081	6.63	0.03679	3.2	0.484	16.865	5.8	233	7.6	267	20	577.9	63
46	140	1434	0.18732	8.52	0.02589	3.52	0.413	19.054	7.76	165	5.9	174.3	16.1	306.5	88.3
47	40	646	0.12928	8.57	0.02312	2.43	0.283	24.662	8.22	147	3.6	123.4	11.2	-315.9	105.4
48	72	26253	12.34651	3.78	0.49027	2.21	0.585	5.475	3.06	2572	69.4	2631.1	388.5	2677	25.3
49	475	716	0.11468	3.5	0.01702	2.37	0.679	20.462	2.56	109	2.6	110.2	4.1	141.7	30.1
50	54	10136	4.48701	4.02	0.30721	3.45	0.859	9.44	2.06	1727	68	1728.6	168.4	1730.5	18.9
51	35	2524	0.20903	89.33	0.03058	30.82	0.345	20.171	83.85	194	60.5	192.7	173.8	175.2	978
51a	0	474	4.09107	68.63	0.29743	54.97	0.801	10.024	41.08	1679	976.2	1652.5	1357.5	1619.6	382.3
52	57	993	0.14756	62.46	0.02934	2.3	0.037	27.416	62.42	186	4.3	139.8	89.5	-595.2	847.5
53	98	1186	0.20442	7.48	0.03345	3.58	0.479	22.565	6.56	212	7.7	188.9	15.4	-93	80.5
54	65	8527	1.56077	3.44	0.15311	2.26	0.657	13.526	2.6	918	22.3	954.8	53.2	1039.6	26.2
55	146	1398	0.14224	7.94	0.02176	2.06	0.259	21.09	7.66	139	2.9	135	11.4	70.3	91.1

Table B.2.

		Isotopic Ratios							Apparent ages					
Crystal	U (ppm)	$^{206}Pb/^{204}Pb$	$^{207}Pb/^{235}U$	±(%)	$^{206}Pb/^{238}U$	±(%)	errcorr	U/Th	$^{206}Pb/^{238}U$ age	±(Ma)	$^{207}Pb/^{235}U$ age	±(Ma)	$^{206}Pb/^{207}Pb$ age	±(Ma)
PHW 6/9/01-F														
1	19	1026	0.06688	30.9	0.01732	2.6	0.09	8	110.7	2.9	66	21	NA	NA
2	11	299	0.20979	98.2	0.01718	3.1	0.03	8	109.8	3.4	193	190	1395	941
3	11	380	0.07378	111.5	0.01650	3.6	0.03	10	105.5	3.8	72	80	NA	NA
4	9	390	1.68281	413.7	0.01609	5.7	0.01	13	102.9	5.9	1002	2107	4846	2956
5	42	1699	0.16193	53.7	0.01721	1.4	0.03	4	110.0	1.5	152	85	876	555
6	12	262	-0.03462	45.0	0.01682	3.2	0.07	10	107.5	3.4	NA	NA	NA	NA
7	15	313	-0.00206	44.7	0.01641	3.2	0.07	7	104.9	3.4	NA	NA	NA	NA
8	14	151	0.06627	26.3	0.01574	4.3	0.17	26	100.7	4.4	65	18	NA	NA
9	10	236	0.05217	26.6	0.01627	4.2	0.16	10	104.0	4.4	52	14	NA	NA
10	37	699	0.08112	16.7	0.01764	2.3	0.14	6	112.7	2.6	79	14	NA	NA
11	10	164	0.56789	211.2	0.01536	4.3	0.02	19	98.2	4.3	457	800	3295	1657
12	14	416	0.31452	104.0	0.01710	3.3	0.03	19	109.3	3.7	278	287	2143	908
13	51	1742	0.13245	22.4	0.01823	1.3	0.06	5	116.4	1.5	126	30	316	255
14	13	662	0.12755	273.8	0.01936	2.7	0.01	18	123.6	3.4	122	304	88	3245
15	11	315	0.02323	90.7	0.01803	3.2	0.04	14	115.2	3.7	23	21	NA	NA
16	90	2742	0.10169	10.1	0.01683	0.7	0.07	4	107.6	0.8	98	10	NA	NA
17	18	391	0.00945	45.8	0.01641	2.6	0.06	14	104.9	2.7	10	4	NA	NA
18	162	2936	0.11507	2.2	0.01707	0.9	0.39	4	109.1	0.9	111	3	142	24
19	17	354	0.07994	273.6	0.01632	2.4	0.01	14	104.4	2.5	78	201	NA	NA
20	23	388	0.07890	18.7	0.01708	1.4	0.08	14	109.2	1.6	77	15	NA	NA
21	13	232	-0.00143	70.5	0.01917	3.7	0.05	11	122.4	4.5	NA	NA	NA	NA
22	24	505	0.05669	40.1	0.01639	1.6	0.04	10	104.8	1.7	56	23	NA	NA
23	14	223	0.03865	31.0	0.01693	3.3	0.11	23	108.2	3.6	39	12	NA	NA
24	19	414	0.01163	32.8	0.01679	2.4	0.07	11	107.4	2.6	12	4	NA	NA
25	10	170	0.20513	81.7	0.01620	3.7	0.05	7	103.6	3.8	190	157	1464	776

Table B.2.Continued

		Isotopic Ratios							Apparent ages					
Crystal	U (ppm)	$^{206}Pb/^{204}Pb$	$^{207}Pb/^{235}U$	±(%)	$^{206}Pb/^{238}U$	±(%)	errcorr	U/Th	$^{206}Pb/^{238}U$ age	±(Ma)	$^{207}Pb/^{235}U$ age	±(Ma)	$^{206}Pb/^{204}Pb$ age	±(Ma)
PHW 6/9/01-B														
1	68	2001	0.11704	10.0	0.01880	0.9	0.09	13	120.1	1.1	112	12	NA	NA
2	14	643	0.33387	361.6	0.01805	2.5	0.01	4	115.3	2.9	293	804	2153	3157
3	22	574	0.11388	14.6	0.01742	2.5	0.17	6	111.4	2.8	110	17	69	171
4	15	518	0.22443	143.2	0.01663	3.9	0.03	6	106.3	4.2	206	283	1584	1338
5	14	227	0.03549	58.4	0.01600	3.4	0.06	6	102.3	3.5	35	21	NA	NA
6	12	747	0.10597	74.4	0.01650	4.4	0.06	6	105.5	4.6	102	77	28	890
7	44	1771	0.10132	17.3	0.01679	1.6	0.09	5	107.3	1.7	98	18	NA	NA
8	86	6265	0.11057	6.7	0.01668	0.8	0.11	4	106.6	0.8	107	8	103	79
9	50	1756	0.06448	24.7	0.01742	0.8	0.03	3	111.4	0.9	63	16	NA	NA
10	15	809	-0.30158	338.6	0.01743	2.8	0.01	6	111.4	3.2	NA	NA	NA	NA
11	21	536	0.04479	37.0	0.01649	2.1	0.06	10	105.4	2.2	45	17	NA	NA
12	50	862	0.10673	15.2	0.01719	1.5	0.10	6	109.9	1.7	103	16	NA	NA
13	20	299	-0.06670	61.4	0.01539	1.9	0.03	5	98.5	1.8	NA	NA	NA	NA
14	28	254	-0.04087	19.0	0.01685	2.0	0.10	7	107.7	2.1	NA	NA	NA	NA
15	15	274	0.28831	181.1	0.01516	2.1	0.01	7	97.0	2.1	257	427	2201	1572
16	29	329	-0.00862	27.3	0.01698	1.7	0.06	6	108.5	1.9	NA	NA	NA	NA
17	14	276	0.22261	90.4	0.01532	4.4	0.05	32	98.0	4.4	204	186	1721	829
18	71	1264	0.07273	13.7	0.01702	0.5	0.04	5	108.8	0.6	71	10	NA	NA
19	47	1240	0.07417	15.4	0.01639	1.0	0.06	7	104.8	1.0	73	12	NA	NA
20	28	540	0.09070	57.0	0.01716	1.5	0.03	6	109.7	1.6	88	51	NA	NA
21	107	1782	0.10764	4.0	0.01741	1.0	0.24	6	111.2	1.1	104	4	NA	NA
22	15	270	0.10539	74.7	0.01657	3.3	0.04	10	105.9	3.5	102	77	5	899
23	28	483	-0.03161	41.4	0.01556	2.5	0.06	9	99.5	2.5	NA	NA	NA	NA
24	30	486	0.02846	37.8	0.01621	1.9	0.05	6	103.6	1.9	29	11	NA	NA

Table B.2.Continued

		Isotopic Ratios							Apparent ages					
Crystal	U (ppm)	$^{206}Pb/^{204}Pb$	$^{207}Pb/^{235}U$	±(%)	$^{206}Pb/^{238}U$	±(%)	errcorr	U/Th	$^{206}Pb/^{238}U$ age	±(Ma)	$^{207}Pb/^{235}U$ age	±(Ma)	$^{206}Pb/^{207}Pb$ age	±(Ma)
PHW 7/6/01-S														
1	15	320	0.04167	36.9	0.01678	6.0	0.16	7	107.3	6.5	42	16	NA	NA
2	24	653	0.06255	54.9	0.01699	2.1	0.04	4	108.6	2.3	62	34	NA	NA
3	22	838	0.14368	22.4	0.01713	2.5	0.11	6	109.5	2.8	136	32	633	240
4	14	640	0.09944	65.4	0.01662	4.2	0.06	5	106.3	4.5	96	64	NA	NA
5	10	596	0.15592	72.4	0.01719	4.8	0.07	11	109.9	5.3	147	109	800	757
6	11	483	0.02933	284.0	0.01545	5.9	0.02	10	98.9	5.9	29	81	NA	NA
7	14	493	0.02286	57.9	0.01587	3.1	0.05	6	101.5	3.2	23	13	NA	NA
8	20	823	0.05730	51.6	0.01665	3.0	0.06	6	106.4	3.2	57	30	NA	NA
9	16	186	-0.09083	59.6	0.01611	3.8	0.06	14	103.0	4.0	NA	NA	NA	NA
10	20	156	0.02122	19.0	0.01563	2.3	0.12	14	100.0	2.3	21	4	NA	NA
11	30	423	0.01864	84.3	0.01649	3.3	0.04	6	105.4	3.5	19	16	NA	NA
12	25	281	-0.01051	19.7	0.01623	3.4	0.18	6	103.8	3.6	NA	NA	NA	NA
13	36	662	0.08962	38.7	0.01608	1.0	0.03	7	102.8	1.1	87	35	NA	NA
14	43	222	0.02868	10.2	0.01558	1.1	0.11	8	99.7	1.1	29	3	NA	NA
15	22	426	0.26915	63.2	0.01705	1.7	0.03	9	109.0	1.9	242	160	1872	570
16	30	731	0.09974	108.1	0.01657	2.0	0.02	9	105.9	2.2	97	104	NA	NA
17	23	414	0.30021	211.5	0.01702	2.3	0.01	7	108.8	2.6	267	499	2070	1864
18	57	251	0.06879	8.0	0.01649	0.7	0.09	67	105.4	0.8	68	6	NA	NA
19	15	248	-0.04033	47.2	0.01626	1.8	0.04	9	104.0	1.9	NA	NA	NA	NA
20	25	630	0.05662	63.6	0.01658	1.9	0.03	8	106.0	2.0	56	36	NA	NA
21	22	521	0.07181	31.3	0.01638	1.7	0.05	8	104.8	1.8	70	23	NA	NA
22	19	623	0.06070	60.6	0.01732	2.7	0.05	7	110.7	3.0	60	37	NA	NA
23	25	419	0.13923	202.2	0.01727	1.9	0.01	7	110.4	2.1	132	252	547	2208

Table B.2.Continued

		Isotopic Ratios							Apparent ages					
Crystal	U (ppm)	$^{206}Pb/^{204}Pb$	$^{207}Pb/^{235}U$	±(%)	$^{206}Pb/^{238}U$	±(%)	errcorr	U/Th	$^{206}Pb/^{238}U$ age	±(Ma)	$^{207}Pb/^{235}U$ age	±(Ma)	$^{206}Pb/^{207}Pb$ age	±(Ma)
PHW 1/12/03-A														
1	13	413	0.03007	37.2	0.01679	4.1	0.11	10	107.3	4.4	30	11	NA	NA
2	14	323	0.07233	68.1	0.01682	3.5	0.05	16	107.5	3.7	71	49	NA	NA
3	20	587	0.08210	23.1	0.01682	2.5	0.11	15	107.5	2.7	80	19	NA	NA
4	20	680	0.13665	275.0	0.01669	2.5	0.01	11	106.7	2.7	130	324	581	2986
5	32	514	0.05336	11.3	0.01680	2.5	0.22	12	107.4	2.6	53	6	NA	NA
6	16	485	0.03810	63.7	0.01557	2.2	0.03	15	99.6	2.2	38	24	NA	NA
7	14	448	0.08321	526.0	0.01609	2.7	0.01	21	102.9	2.8	81	369	NA	NA
8	15	404	0.04965	47.4	0.01652	2.8	0.06	18	105.6	3.0	49	24	NA	NA
9	21	613	0.05649	42.0	0.01632	2.0	0.05	18	104.3	2.1	56	24	NA	NA
10	20	354	-0.00488	26.4	0.01602	3.4	0.13	12	102.5	3.5	NA	NA	NA	NA
11	19	376	0.03685	30.9	0.01672	2.7	0.09	14	106.9	2.9	37	12	NA	NA
12	46	1076	0.09374	13.7	0.01715	1.3	0.10	7	109.6	1.5	91	13	NA	NA
13	17	598	0.03628	71.9	0.01660	2.5	0.04	16	106.2	2.7	36	26	NA	NA
14	27	589	0.07120	20.6	0.01623	2.6	0.13	14	103.8	2.7	70	15	NA	NA
15	29	522	0.56063	261.1	0.01671	2.9	0.01	24	106.8	3.1	452	916	3142	2074
16	19	491	0.03510	17.3	0.01618	1.7	0.10	15	103.5	1.8	35	6	NA	NA
17	20	892	1.09631	536.7	0.01648	2.5	0.01	21	105.4	2.6	752	1959	4189	3967
18	17	316	-0.00350	22.5	0.01618	2.1	0.09	22	103.4	2.1	NA	NA	NA	NA
19	28	406	0.04744	21.3	0.01603	3.4	0.16	12	102.5	3.5	47	10	NA	NA
20	10	119	-0.06448	21.5	0.01616	4.0	0.19	22	103.4	4.1	NA	NA	NA	NA
21	35	104107	0.09547	17.4	0.01610	1.3	0.08	17	103.0	1.4	93	17	NA	NA

Table B.2.Continued

		Isotopic Ratios							Apparent ages					
Crystal	U (ppm)	$^{206}Pb/^{204}Pb$	$^{207}Pb/^{235}U$	±(%)	$^{206}Pb/^{238}U$	±(%)	errcorr	U/Th	$^{206}Pb/^{238}U$ age	±(Ma)	$^{207}Pb/^{235}U$ age	±(Ma)	$^{206}Pb/^{207}Pb$ age	±(Ma)
PHW 1/18/03-H														
1	30	677	0.06655	23.5	0.01841	2.1	0.09	6	117.6	2.4	65	16	NA	NA
2	20	587	0.08448	23.2	0.01731	2.5	0.11	14	110.6	2.8	82	20	NA	NA
3	20	680	0.96463	275.0	0.01718	2.5	0.01	11	109.8	2.7	686	1315	3936	2064
4	35	988	0.14433	21.6	0.01737	1.3	0.06	8	111.0	1.4	137	31	613	233
5	91	586	0.15049	5.8	0.01844	0.6	0.11	21	117.8	0.8	142	9	574	63
6	37	1261	0.10749	22.8	0.01810	1.0	0.04	6	115.7	1.2	104	25	NA	NA
7	21	607	0.08408	55.9	0.01726	1.8	0.03	8	110.3	2.0	82	47	-683	773
8	12	631	0.14773	80.6	0.01796	3.3	0.04	12	114.7	3.9	140	114	591	873
9	37	598	0.04658	18.7	0.01772	1.0	0.05	7	113.2	1.1	46	9	NA	NA
10	31	631	0.09370	30.7	0.01854	1.3	0.04	7	118.4	1.5	91	29	NA	NA
11	50	1277	0.09557	11.1	0.01863	1.1	0.10	7	119.0	1.3	93	11	NA	NA
12	61	1923	0.11734	9.4	0.01859	0.8	0.08	7	118.7	0.9	113	11	NA	NA
13	39	1094	0.12601	18.6	0.01731	1.8	0.10	8	110.6	2.0	121	24	320	210
14	46	1070	0.10488	19.2	0.01825	1.3	0.07	8	116.6	1.5	101	20	NA	NA
15	38	805	0.03748	32.1	0.01821	1.2	0.04	11	116.3	1.5	37	12	NA	NA
16	73	913	0.08142	9.8	0.01754	1.0	0.10	8	112.1	1.1	80	8	NA	NA
17	39	514	0.12067	18.6	0.01794	1.5	0.08	13	114.6	1.8	116	23	137	218
18	40	896	0.11501	14.4	0.01844	1.2	0.09	7	117.8	1.4	111	17	NA	NA
19	33	388	0.10445	8.9	0.01886	1.8	0.20	11	120.5	2.1	101	9	NA	NA
20	30	647	0.06674	37.5	0.01867	1.2	0.03	8	119.3	1.5	66	25	NA	NA
21	44	878	0.06262	14.7	0.01804	1.5	0.10	7	115.2	1.7	62	9	NA	NA
22	65	1910	0.10656	11.7	0.01904	0.9	0.07	7	121.6	1.0	103	13	NA	NA

Table B.2.Continued

		Isotopic Ratios							Apparent ages					
Crystal	U (ppm)	$^{206}Pb/^{204}Pb$	$^{207}Pb/^{235}U$	±(%)	$^{206}Pb/^{238}U$	±(%)	errcorr	U/Th	$^{206}Pb/^{238}U$ age	±(Ma)	$^{207}Pb/^{235}U$ age	±(Ma)	$^{206}Pb/^{207}Pb$ age	±(Ma)
PHW 5/29/01-B														
1	27	380	0.06354	16.0	0.01885	2.0	0.13	6	120.4	2.5	63	10	NA	NA
2	14	10667	0.09648	31.1	0.01809	2.9	0.09	5	115.6	3.4	94	30	NA	NA
3	56	569	0.04126	19.6	0.01770	1.6	0.08	17	113.1	1.8	41	8	NA	NA
4	107	766	0.06678	7.1	0.01745	1.2	0.16	33	111.5	1.3	66	5	NA	NA
5	34	421	0.09922	13.6	0.01828	1.6	0.11	13	116.8	1.8	96	14	NA	NA
6	12	209	0.05758	362.8	0.01739	5.3	0.00	7	111.1	6.0	57	1074	NA	NA
7	35	329	0.04891	15.1	0.01796	3.1	0.20	21	114.7	3.6	49	8	NA	NA
8	41	160	1.00878	29.3	0.02335	2.6	0.09	17	148.8	3.9	708	263	3537	225
9	18	420	0.23374	87.5	0.01825	2.9	0.03	9	116.6	3.4	213	189	1485	828
10	61	3566	0.10539	8.7	0.01880	1.1	0.12	5	120.1	1.3	102	9	NA	NA
11	21	675	0.17328	451.8	0.01784	3.0	0.00	7	114.0	3.5	162	1277	941	1476
12	12	332	0.04325	28.8	0.01749	4.1	0.14	15	111.8	4.6	43	13	NA	NA
13	13	183	0.41867	330.1	0.01715	2.8	0.01	11	109.6	3.1	355	881	2625	2745
14	9	221	-0.01323	24.9	0.01718	2.9	0.12	6	109.8	3.2	NA	NA	NA	NA
15	8	194	0.34291	147.3	0.01857	4.2	0.03	7	118.6	5.1	299	415	2150	1286
16	18	195	0.12068	17.0	0.02000	3.7	0.22	25	127.7	4.8	116	21	NA	NA
17	56	1063	0.07238	16.2	0.01790	1.9	0.12	23	114.4	2.2	71	12	NA	NA
18	11	228	0.11250	38.3	0.01762	2.5	0.07	6	112.6	2.8	108	43	14	459
19	11	308	0.02934	30.4	0.01744	3.8	0.13	13	111.4	4.3	29	9	NA	NA
20	15	287	-0.01351	633.8	0.01747	3.1	0.00	8	111.6	3.5	NA	NA	NA	NA
21	9	204	-0.07208	975.9	0.01739	3.5	0.00	7	111.1	3.9	NA	NA	NA	NA

APPENDIX C: PRIMARY FABRIC DATA

Table C.1. Directed fabric data measured in all samples. L-lithics, Plag-plagioclase, San-sanidine, HBL-hornblende, Q-quartz, and P-pumice. C.V. Ext. are apparent constant volume extensions assume that the final axial ratios (X,Y,Z) formed by constant volume strain of an initially perfectly uniform population of markers. Strain Magnitude is equal to $1/3[(E_1-E_2)^2 + (E_2-E_3)^2 + (E_3-E_1)^2]^{1/2}$ where E_1, E_2, and E_3 are the principle natural strains. Symmetry is equivalent to the Lodes Parameter where negative numbers = prolate shapes, 0.0 = plane strain, and positive numbers = oblate shapes. Total error is a measure of the misfit between the three ellipses measured from the three mutually perpendicular faces when combining to produce a single ellipsoid.

	Length			Apparent constant volume extension			Apparent Strain	Lodes			Total	Angle
Sample	X	Y	Z	X	Y	Z	Magnitude	Paremeter	E_1-E_2	E_2-E_3	Error	XY-Bedding
188-L	1.33	1.07	1	18.1	-4.8	-11.0	0.21	-0.52	0.22	0.07	0.03	12
192-L	1.29	1.23	1	10.4	5.7	-14.3	0.19	0.66	0.04	0.21	0.03	74
193-L	1.27	1.25	1	8.5	7.5	-14.2	0.19	0.92	0.01	0.23	0.05	15
194-L	1.35	1.18	1	15.6	1.2	-14.5	0.21	0.12	0.13	0.17	0.04	65
195-L	1.25	1.10	1	12.5	-1.1	-10.1	0.16	-0.15	0.13	0.10	0.04	31
198-L	1.47	1.27	1	19.2	3.3	-18.8	0.27	0.25	0.14	0.24	0.04	89
200-L	1.16	1.12	1	6.6	2.4	-8.4	0.11	0.47	0.04	0.11	0.03	54
202-L	1.29	1.24	1	10.5	6.0	-14.6	0.20	0.68	0.04	0.22	0.04	42
203-L	1.24	1.16	1	9.7	2.8	-11.4	0.16	0.39	0.07	0.15	0.02	40
218-L	1.33	1.18	1	14.2	1.8	-14.0	0.20	0.19	0.11	0.17	0.04	62
221-L	1.50	1.26	1	21.5	1.8	-19.2	0.29	0.13	0.18	0.23	0.23	6
P-4-L	1.28	1.18	1	11.6	3.0	-12.9	0.18	0.35	0.08	0.17	0.03	ND
PHW-2-24-A-L	1.29	1.21	1	11.3	4.3	-13.8	0.19	0.49	0.07	0.19	0.03	26
PHW-2-24-B1-L	1.12	1.03	1	6.7	-1.9	-4.4	0.08	-0.54	0.08	0.03	0.03	39
PHW-2-24-B2-L	1.21	1.10	1	9.8	0.2	-9.1	0.13	0.03	0.09	0.10	0.03	11
PHW2-24-B3-L	1.62	1.49	1	20.6	11.1	-25.4	0.36	0.66	0.08	0.40	0.07	33
PHW-2-24-B4-L	1.39	1.16	1	18.6	-1.0	-14.8	0.24	-0.09	0.18	0.15	0.04	74
PHW-2-24-B6-L	1.19	1.13	1	7.6	2.3	-9.2	0.12	0.40	0.05	0.12	0.03	71
PHW-2-24-C1-L	1.18	1.14	1	7.0	3.1	-9.3	0.12	0.55	0.04	0.13	0.03	7
PHW-2-24-C-L	1.36	1.24	1	14.3	4.3	-16.1	0.23	0.40	0.09	0.22	0.12	54
PHW-2-25-A1-L	1.14	1.12	1	5.0	3.3	-7.8	0.10	0.76	0.02	0.11	0.03	66
PHW-2-25-A2-L	1.22	1.19	1	7.6	5.0	-11.5	0.15	0.74	0.03	0.17	0.04	60
PHW-2-25-A-L	1.10	1.04	1	5.4	-0.8	-4.3	0.07	-0.25	0.06	0.04	0.04	1
PHW-2-25-C-L	1.11	1.02	1	6.4	-1.9	-4.2	0.08	-0.55	0.08	0.02	0.03	78
PHW-UNKNOWN-L	1.20	1.14	1	7.9	2.7	-9.8	0.13	0.45	0.05	0.13	0.03	N/A
Mean Lithics	**1.28**	**1.17**	**1**	**11.5**	**2.4**	**-12.1**	**0.17**	**0.26**	**0.08**	**0.15**	**0.05**	
218-Plag	1.14	1.01	1	8.9	-3.7	-4.7	0.11	-0.84	0.12	0.01	0.09	76
PHW-2-24-B3-Plag	1.67	1.52	1	22.2	11.4	-26.6	0.38	0.64	0.09	0.42	0.04	53
PHW-2-25-A-PLAG	1.12	1.05	1	6.1	-0.4	-5.4	0.08	-0.10	0.06	0.05	0.04	1
PHW-2-25-C-PLAG	1.12	1.06	1	5.8	-0.2	-5.3	0.08	-0.04	0.06	0.05	0.04	78
PHW-UNKNOWN-PLAG	1.23	1.14	1	9.7	2.0	-10.6	0.15	0.29	0.07	0.13	0.03	N/A
PST-SAN	1.35	1.22	1	14.4	3.2	-15.3	0.22	0.31	0.10	0.20	0.08	78
Mean Plag	**1.27**	**1.17**	**1**	**11.2**	**2.1**	**-11.3**	**0.17**	**0.04**	**0.09**	**0.14**	**0.05**	
212-HBL	1.11	1.08	1	4.1	2.0	-5.9	0.08	0.60	0.02	0.08	0.04	27
240-HBl	1.26	1.09	1	12.9	-1.6	-10.0	0.16	-0.21	0.14	0.09	0.02	30
PHW-2-24-B-HBL	1.22	1.13	1	9.6	1.5	-10.1	0.14	0.22	0.08	0.12	0.04	11
Mean HBL	**1.19**	**1.10**	**1**	**8.9**	**0.6**	**-8.7**	**0.13**	**0.20**	**0.08**	**0.10**	**0.03**	

Appendix C (Table C.1) Continued

	Length			Apparent constant volume extension			Apparent Strain	Lodes			Total	Angle
Sample	X	Y	Z	X	Y	Z	Magnitude	Paremeter	E_1-E_2	E_2-E_3	Error	XY-Bedding
184-Q	1.07	1.03	1	4.0	-0.6	-3.2	0.05	-0.26	0.05	0.03	0.03	ND
186-Q	1.44	1.16	1	21.2	-2.2	-15.7	0.26	-0.18	0.21	0.15	0.04	40
188-Q	1.05	1.03	1	2.0	0.6	-2.6	0.03	0.38	0.01	0.03	0.03	72
189-Q	1.07	1.04	1	3.2	0.2	-3.3	0.05	0.10	0.03	0.04	0.02	21
192-Q	1.46	1.27	1	18.8	3.2	-18.4	0.27	0.25	0.14	0.24	0.03	76
193-Q	1.17	1.08	1	8.4	-0.4	-7.4	0.11	-0.08	0.09	0.07	0.02	41
194-Q	1.23	1.11	1	11.1	-0.2	-9.8	0.15	-0.03	0.11	0.10	0.03	23
195-Q	1.25	1.14	1	11.0	1.2	-11.0	0.16	0.14	0.09	0.13	0.04	40
196-Q	1.25	1.16	1	10.9	2.1	-11.6	0.16	0.27	0.08	0.14	0.03	24
198-Q	1.58	1.47	1	19.2	11.0	-24.4	0.35	0.69	0.07	0.38	0.05	90
200-Q	1.13	1.12	1	4.9	3.1	-7.5	0.10	0.73	0.02	0.11	0.03	27
202-Q	1.26	1.22	1	9.1	5.6	-13.2	0.17	0.71	0.03	0.20	0.03	44
203-Q	1.03	1.02	1	1.2	0.2	-1.4	0.02	0.21	0.01	0.02	0.01	63
220-Q	1.52	1.28	1	22.0	2.3	-19.8	0.30	0.16	0.18	0.24	0.05	27
221-Q	1.11	1.03	1	6.2	-1.8	-4.2	0.08	-0.52	0.08	0.03	0.03	16
229-Q	1.15	1.11	1	6.1	2.4	-8.0	0.11	0.50	0.04	0.11	0.02	15
262-Q	1.11	1.06	1	5.2	0.2	-5.1	0.07	0.06	0.05	0.05	0.03	9
P-4-Q	1.22	1.12	1	9.9	0.9	-9.8	0.14	0.14	0.09	0.11	0.03	ND
PHW-2-25-A2-Q	1.12	1.09	1	4.7	1.9	-6.3	0.08	0.52	0.03	0.09	0.03	60
Mean Quartz	**1.22**	**1.13**	**1**	**9.4**	**1.6**	**-9.6**	**0.14**	**0.20**	**0.07**	**0.12**	**0.03**	
184-P	1.48	1.38	1	16.3	9.1	-21.2	0.30	0.67	0.06	0.33	0.03	ND
186-P	2.79	2.29	1	50.1	23.6	-46.1	0.77	0.62	0.19	0.83	0.09	30
188-P	3.85	2.90	1	72.2	29.7	-55.3	1.01	0.58	0.28	1.06	0.05	25
189-P	2.16	1.85	1	36.0	16.6	-37.0	0.58	0.60	0.15	0.62	0.30	22
192-P	1.39	1.18	1	18.0	0.0	-15.3	0.23	0.00	0.17	0.17	0.05	85
193.P	3.63	3.41	1	57.0	47.4	-56.8	1.03	0.90	0.06	1.23	0.07	16
194-P	3.71	2.78	1	70.5	27.7	-54.1	0.97	0.56	0.29	1.02	0.05	36
195-P	2.58	2.39	1	40.5	30.4	-45.4	0.74	0.84	0.08	0.87	0.06	32
196-P	8.26	4.59	1	145.9	36.6	-70.2	1.54	0.44	0.59	1.52	0.11	21
198-P	1.62	1.37	1	24.1	4.9	-23.2	0.35	0.30	0.17	0.31	0.05	88
200-P	1.96	1.68	1	31.9	12.8	-32.8	0.50	0.54	0.16	0.52	0.05	61
202-P	5.46	3.79	1	98.9	38.1	-63.6	1.26	0.57	0.37	1.33	0.05	43
203-P	3.26	2.95	1	53.3	38.6	-52.9	0.93	0.83	0.10	1.08	0.05	35
212-P	1.35	1.29	1	12.3	7.2	-17.0	0.23	0.69	0.05	0.26	0.06	64
262-P	1.64	1.44	1	23.4	7.9	-24.9	0.36	0.46	0.13	0.36	0.05	13
PHW-UNKNOWN-P	2.95	2.52	1	51.3	28.9	-48.7	0.83	0.70	0.16	0.92	0.05	ND
PST-P	4.50	3.52	1	79.2	40.2	-60.2	1.14	0.67	0.25	1.26	0.17	39
Mean Pumic	**3.09**	**2.43**	**1**	**51.8**	**23.5**	**-42.6**	**0.75**	**0.59**	**0.19**	**0.81**	**0.08**	
CGL-01	1.51	1.45	1	16.5	11.6	-23.1	0.32	0.79	0.04	0.37		ND
BE-7	1.64	1.33	1	26.0	2.6	-23.0	0.35	0.15	23.40	25.60		ND
SS 4a	2.10	1.58	1	41.0	5.9	-33.0	0.53	0.23	35.10	38.90		ND
SS 4b	1.98	1.59	1	35.0	8.5	-32.0	0.49	0.36	26.50	40.50		ND
Iore Fm. 1	1.19	1.16	1	6.8	4.3	-10.3	0.13	0.73	2.49	14.60		ND
Iore Fm. 2	1.94	1.43	1	38.3	1.6	-28.8	0.47	0.07	36.69	30.40		ND
Mean CGL	**1.73**	**1.42**	**1**	**27.3**	**5.7**	**-25.0**	**0.38**	**0.39**	**20.70**	**25.06**		

Appendix C (Table C.1) Continued

	Length			Apparent constant volume extension			Apparent Strain	Lodes			Total	Angle
Sample	X	Y	Z	X	Y	Z	Magnitude	Paremeter	E_1-E_2	E_2-E_3	Error	XY-Bedding
OP1	1.88	1.61	1	30.0	11.3	-30.9	0.47	0.51	0.16	0.48		ND
OP6	1.13	1.10	1	5.1	2.3	-7.0	0.09	0.56	0.03	0.10		ND
OP7	1.02	1.01	1	1.0	0.0	-1.0	0.01	0.00	0.01	0.01		ND
OP10	1.71	1.24	1	33.1	-3.5	-22.2	0.38	-0.20	0.32	0.22		ND
GVS25	1.57	1.46	1	19.1	10.7	-24.2	0.34	0.68	0.07	0.38		ND
GVS27	1.46	1.30	1	17.9	5.0	-19.2	0.27	0.39	0.12	0.26		ND
GVS30	1.61	1.36	1	24.0	4.7	-23.0	0.34	0.29	0.17	0.31		ND
GVS32	1.54	1.36	1	20.4	6.3	-21.8	0.31	0.42	0.12	0.31		ND
GVS34	1.58	1.57	1	16.7	16.0	-26.1	0.37	0.97	0.01	0.45		ND
GVS36	1.31	1.25	1	11.1	6.1	-15.2	0.20	0.65	0.05	0.22		ND
P22	1.74	1.53	1	25.6	10.4	-27.9	0.41	0.54	0.13	0.43		ND
P23	1.45	1.26	1	18.6	3.1	-18.2	0.27	0.24	0.14	0.23		ND
P24	1.58	1.39	1	21.6	6.9	-23.1	0.33	0.44	0.13	0.33		ND
P25	1.66	1.47	1	23.3	9.2	-25.7	0.37	0.52	0.12	0.39		ND
P26	1.20	1.18	1	6.9	5.1	-11.0	0.14	0.82	0.02	0.17		ND
OP6	1.13	1.10	1	5.1	2.3	-7.0	0.09	0.56	0.03	0.10		ND
OP7	1.02	1.01	1	1.0	0.0	-1.0	0.01	0.00	0.01	0.01		ND
P21	1.88	1.60	1	30.0	11.3	-30.9	0.47	0.51	0.16	0.47		ND
ODP 808C-1	1.27	1.19	1	10.5	3.7	-12.7	0.17	0.46	0.07	0.17		ND
ODP 808C-2	1.33	1.19	1	14.4	1.8	-14.1	0.20	0.19	0.11	0.17		ND
ODP 808C-3	1.53	1.40	1	18.8	8.6	-22.5	0.32	0.58	0.09	0.34		ND
ODP 808C-4	1.27	1.09	1	14.3	-2.5	-10.2	0.17	-0.32	0.15	0.09		ND
ODP 808C-5	1.35	1.24	1	13.7	4.6	-15.9	0.22	0.44	0.08	0.22		ND
ODP 808C-6	1.23	1.11	1	10.6	0.2	-9.8	0.14	0.04	0.10	0.10		ND
ODP 808C-7	1.32	1.24	1	12.3	4.9	-15.2	0.21	0.51	0.06	0.22		ND
ODP 808C-8	1.23	1.21	1	7.8	6.1	-12.6	0.17	0.85	0.02	0.19		ND
ODP 808C-9	1.37	1.28	1	13.7	6.2	-17.2	0.24	0.57	0.07	0.25		ND
LT01	3.13	3.11	1	47.0	46.0	-53.0	0.93	0.99	0.01	1.13		ND
LT02	2.92	2.92	1	43.0	43.0	-51.0	0.87	1.00	0.00	1.07		ND
LT03	3.24	3.17	1	49.0	46.0	-54.0	0.95	0.97	0.02	1.15		ND
LT04	3.20	3.20	1	47.0	47.0	-54.0	0.95	1.00	0.00	1.16		ND
LT05	2.98	2.55	1	52.0	30.0	-49.0	0.84	0.71	0.16	0.94		ND
LT06	3.55	3.30	1	56.0	45.0	-56.0	1.00	0.88	0.07	1.19		ND
LT07	2.90	2.59	1	48.0	32.0	-49.0	0.83	0.79	0.11	0.95		ND
LT08	2.33	2.00	1	40.0	20.0	-40.0	0.64	0.64	0.15	0.69		ND
LT09	2.27	2.15	1	34.0	27.0	-41.0	0.65	0.87	0.05	0.77		ND
LT10	2.87	2.50	1	49.0	30.0	-48.0	0.81	0.74	0.14	0.92		ND
LT11	2.41	2.12	1	40.0	23.0	-42.0	0.67	0.71	0.13	0.75		ND
LT12	2.67	2.37	1	44.0	28.0	-46.0	0.76	0.76	0.12	0.86		ND
LT13	2.26	1.85	1	40.0	15.0	-38.0	0.60	0.52	0.20	0.62		ND
LT14	4.27	3.39	1	75.0	39.0	-59.0	1.10	0.68	0.23	1.22		ND
LT15	2.16	2.03	1	32.0	24.0	-39.0	0.61	0.84	0.06	0.71		ND
LT16	2.43	1.90	1	46.0	14.0	-40.0	0.65	0.44	0.25	0.64		ND

Appendix C (Table C.1) Continued

	Length			Apparent constant volume extension			Apparent Strain	Lodes			Total	Angle
Sample	X	Y	Z	X	Y	Z	Magnitude	Paremeter	E_1-E_2	E_2-E_3	Error	XY-Bedding
NYP01	2.02	1.88	1	29.0	20.0	-36.0	0.55	0.79	0.07	0.63		ND
NYP02	2.11	1.98	1	31.0	23.0	-38.0	0.59	0.83	0.06	0.68		ND
NYP03	2.35	1.95	1	41.0	17.0	-40.0	0.64	0.56	0.19	0.67		ND
NYP04	2.16	1.94	1	34.0	20.0	-38.0	0.59	0.71	0.11	0.66		ND
NYP05	1.85	1.71	1	26.0	16.0	-32.0	0.47	0.73	0.08	0.54		ND
NYP06	1.65	1.49	1	22.0	10.0	-26.0	0.37	0.59	0.10	0.40		ND
NYP07	2.00	1.91	1	28.0	22.0	-36.0	0.55	0.86	0.05	0.65		ND
NYP08	1.87	1.79	1	25.0	20.0	-33.0	0.49	0.87	0.04	0.58		ND
NYP09	2.31	2.12	1	36.0	25.0	-41.0	0.65	0.80	0.09	0.75		ND
NYP10	1.64	1.50	1	21.0	11.0	-26.0	37.00	0.65	0.09	0.41		ND
NYP11	2.83	2.52	1	47.0	31.0	-48.0	0.81	0.78	0.12	0.92		ND
NYP12	1.71	1.58	1	23.0	14.0	-28.0	0.41	0.72	0.08	0.46		ND
NYP13	2.60	1.84	1	32.0	18.0	-36.0	0.55	0.69	0.35	0.61		ND
NYP14	1.87	1.81	1	25.0	21.0	-33.0	0.50	0.90	0.03	0.59		ND
NYP15	2.06	1.94	1	30.0	22.0	-37.0	0.57	0.82	0.06	0.66		ND
NYP16	1.93	1.73	1	29.0	16.0	-33.0	0.50	0.68	0.11	0.55		ND
NYP17	2.28	2.03	1	37.0	22.0	-40.0	0.63	0.72	0.12	0.71		ND
NYP18	2.34	2.08	1	38.0	23.0	-41.0	0.65	0.73	0.12	0.73		ND
NYP19	1.97	1.85	1	28.0	20.0	-35.0	0.53	0.81	0.06	0.62		ND
NYP20	1.97	1.85	1	28.0	20.0	-35.0	0.53	0.81	0.06	0.62		ND
NYP21	1.81	1.61	1	27.0	13.0	-30.0	0.45	0.61	0.12	0.48		ND
NYP22	2.62	2.29	1	44.0	26.0	-45.0	0.74	0.72	0.13	0.83		ND
NYP23	2.40	2.16	1	39.0	25.0	-42.0	0.67	0.76	0.11	0.77		ND
NYP24	2.18	2.02	1	33.0	23.0	-39.0	0.61	0.80	0.08	0.70		ND
NYP25	2.02	1.89	1	29.0	21.0	-36.0	0.55	0.82	0.07	0.64		ND
NYP26	1.88	1.88	1	20.0	20.0	-36.0	0.51	1.00	0.00	0.63		ND
NYP27	1.95	1.88	1	27.0	22.0	-35.0	0.53	0.88	0.04	0.63		ND
NYP28	1.67	1.61	1	20.0	16.0	-28.0	0.40	0.58	0.04	0.48		ND
NYP29	1.86	1.86	1	23.0	23.0	-34.0	0.51	1.00	0.00	0.62		ND
NYP30	1.77	1.71	1	22.0	18.0	-31.0	0.45	0.88	0.03	0.54		ND
NYP31	1.70	1.52	1	24.0	11.0	-27.0	0.40	0.58	0.11	0.42		ND
NYP32	1.69	1.58	1	22.0	14.0	-28.0	0.41	0.74	0.07	0.46		ND
NYP33	2.00	2.00	1	26.0	26.0	-37.0	0.57	1.00	0.00	0.69		ND
NYP34	2.06	1.84	1	32.0	18.0	-36.0	0.55	0.69	0.11	0.61		ND
NYP35	2.02	1.80	1	31.0	17.0	-35.0	0.53	0.68	0.12	0.59		ND
NYP36	1.81	1.61	1	27.0	13.0	-30.0	0.45	0.61	0.12	0.48		ND
NYP37	2.26	1.60	1	47.0	4.0	-35.0	0.58	0.15	0.35	0.47		ND
NYP38	2.03	1.78	1	32.0	16.0	-35.0	0.53	0.64	0.13	0.58		ND
NYP39	2.51	2.36	1	38.0	30.0	-45.0	0.73	0.87	0.06	0.86		ND
NYP40	2.82	2.65	1	44.0	35.0	-49.0	0.82	0.88	0.06	0.97		ND
NYP41	1.84	1.81	1	23.0	21.0	-33.0	0.49	0.95	0.02	0.59		ND
NYP42	1.84	1.67	1	27.0	15.0	-31.0	0.46	0.67	0.10	0.51		ND
NYP43	1.84	1.74	1	25.0	18.0	-32.0	0.48	0.81	0.06	0.55		ND
NYP44	2.24	2.17	1	32.0	28.0	-41.0	0.65	0.92	0.03	0.77		ND
NYP45	1.97	1.94	1	26.0	24.0	-36.0	0.55	0.95	0.02	0.66		ND
NYP46	2.26	1.85	1	40.0	15.0	-38.0	0.60	0.52	0.20	0.62		ND
NYP47	1.77	1.64	1	24.0	15.0	-30.0	0.44	0.74	0.08	0.49		ND
NYP48	1.92	1.79	1	27.0	18.0	-34.0	0.51	0.78	0.07	0.58		ND
NYP49	2.19	1.92	1	36.0	19.0	-38.0	0.59	0.66	0.13	0.65		ND
NYP50	1.79	1.56	1	27.0	11.0	-29.0	0.43	0.54	0.14	0.44		ND

Appendix C (Table C.1) Continued

	Length			Apparent constant volume extension			Apparent Strain	Lodes			Total	Angle
Sample	X	Y	Z	X	Y	Z	Magnitude	Paremeter	E_1-E_2	E_2-E_3	Error	XY-Bedding
NYP51	2.25	1.97	1	37.0	20.0	-39.0	0.61	0.67	0.13	0.68		ND
NYP52	1.98	1.77	1	31.0	17.0	-34.0	0.52	0.67	0.11	0.57		ND
NYP53	2.31	1.82	1	43.0	13.0	-38.0	0.61	0.44	0.24	0.60		ND
NYP54	1.84	1.74	1	25.0	18.0	-32.0	0.48	0.81	0.06	0.55		ND
NYP55	2.08	1.81	1	33.0	16.0	-36.0	0.55	0.63	0.14	0.59		ND
NYP56	2.28	2.02	1	37.0	21.0	-40.0	0.63	0.70	0.12	0.70		ND
NYP57	1.59	1.49	1	19.0	12.0	-25.0	0.35	0.74	0.06	0.40		ND
NYP58	2.14	1.71	1	39.0	11.0	-35.0	0.55	0.41	0.22	0.54		ND
NYP59	2.16	2.05	1	32.0	25.0	-39.0	0.61	0.86	0.05	0.72		ND
NYP60	2.32	2.10	1	37.0	24.0	-41.0	0.65	0.76	0.10	0.74		ND
NYP61	2.27	2.07	1	36.0	24.0	-40.0	0.63	0.77	0.09	0.73		ND
NYP62	1.86	1.86	1	23.0	23.0	-34.0	0.51	1.00	0.00	0.62		ND
NYP63	1.83	1.67	1	26.0	15.0	-31.0	0.46	0.70	0.09	0.51		ND
NYP64	1.84	1.65	1	27.0	14.0	-31.0	0.46	0.65	0.11	0.50		ND
NYP65	1.84	1.65	1	27.0	14.0	-31.0	0.46	0.65	0.11	0.50		ND
NYP66	1.64	1.64	1	18.0	18.0	-28.0	0.40	1.00	0.00	0.49		ND
NYP67	2.36	2.17	1	37.0	26.0	-42.0	0.67	0.81	0.08	0.77		ND
NYP68	2.15	1.97	1	33.0	22.0	-38.0	0.59	0.77	0.09	0.68		ND
NYP69	2.18	2.12	1	31.0	27.0	-40.0	0.63	0.92	0.03	0.75		ND
NYP70	1.94	1.77	1	28.0	17.0	-34.0	0.51	0.73	0.09	0.57		ND
NYP71	2.03	1.86	1	30.0	19.0	-36.0	0.55	0.75	0.09	0.62		ND
NYP72	2.15	1.95	1	33.0	21.0	-38.0	0.90	0.75	0.10	0.67		ND
NYP73	2.10	1.92	1	32.0	21.0	-37.0	0.57	0.76	0.09	0.65		ND
NYP74	1.92	1.79	1	27.0	18.0	-34.0	0.51	0.78	0.07	0.58		ND
NYP75	1.87	1.71	1	27.0	16.0	-32.0	0.48	0.71	0.09	0.54		ND
NYP76	1.94	1.70	1	30.0	14.0	-33.0	0.50	0.60	0.13	0.53		ND
NYP77	2.13	2.05	1	30.0	25.0	-39.0	0.60	0.90	0.04	0.72		ND
NYP78	2.02	1.91	1	29.0	22.0	-36.0	0.55	0.84	0.06	0.65		ND
NYP79	1.95	1.77	1	29.0	17.0	-34.0	0.51	0.71	0.10	0.57		ND
NYP80	1.83	1.60	1	28.0	12.0	-30.0	0.45	0.56	0.13	0.47		ND
NYP81	1.94	1.83	1	28.0	21.0	-34.0	0.52	0.83	0.06	0.60		ND
NYP82	1.85	1.71	1	26.0	16.0	-32.0	0.47	0.73	0.08	0.54		ND
NYP83	2.23	1.95	1	36.0	19.0	-39.0	0.61	0.67	0.13	0.67		ND
NYP84	2.85	2.50	1	48.0	30.0	-48.0	0.81	0.75	0.13	0.92		ND
NYP85	2.20	2.02	1	34.0	23.0	-39.0	0.61	0.78	0.09	0.70		ND
NYP86	2.85	2.48	1	48.0	29.0	-48.0	0.80	0.74	0.14	0.91		ND
NYP87	2.55	2.23	1	43.0	25.0	-44.0	0.72	0.71	0.13	0.80		ND
NYP88	2.36	2.05	1	39.0	21.0	-41.0	0.65	0.68	0.14	0.72		ND
NYP89	2.85	2.5	1	48.0	29.0	-48.0	0.80	0.74	0.14	0.91		ND
NYP90	2.20	2.02	1	34.0	23.0	-39.0	0.61	0.78	0.09	0.70		ND
NYP91	2.85	2.48	1	48.0	29.0	-48.0	0.80	0.74	0.14	0.91		ND
NYP92	2.55	2.23	1	43.0	25.0	-44.0	0.82	0.71	0.13	0.80		ND
NYP93	2.36	2.05	1	39.0	21.0	-41.0	0.65	0.68	0.14	0.72		ND
NYP94	2.85	2.48	1	48.0	29.0	-48.0	0.80	0.74	0.14	0.91		ND
NYP95	2.49	2.18	1	42.0	24.0	-43.0	0.70	0.70	0.13	0.78		ND
NYP96	2.08	1.90	1	31.0	20.0	-37.0	0.57	0.76	0.09	0.64		ND
NYP97	2.25	1.97	1	37.0	20.0	-39.0	0.61	0.67	0.13	0.68		ND
NYP98	2.05	1.88	1	31.0	20.0	-36.0	0.55	0.76	0.09	0.63		ND
NYP99	1.93	1.72	1	29.0	15.0	-33.0	0.49	0.65	0.12	0.54		ND
NYP100	2.41	2.12	1	40.0	23.0	-42.0	0.67	0.71	0.13	0.75		ND

Appendix C (Table C.1) Continued

	Length			Apparent constant volume extension			Apparent Strain	Lodes			Total	Angle
Sample	X	Y	Z	X	Y	Z	Magnitude	Paremeter	E_1-E_2	E_2-E_3	Error	XY-Bedding
NYP101	2.09	1.83	1	34.0	17.0	-36.0	0.56	0.63	0.13	0.60		ND
NYP102	1.80	1.70	1	24.0	17.0	-31.0	0.46	0.80	0.06	0.53		ND
NYP103	2.49	2.18	1	42.0	24.0	-43.0	0.70	0.70	0.13	0.78		ND
NYP104	2.36	2.07	1	39.0	22.0	-41.0	0.65	0.70	0.13	0.73		ND
NYP105	2.25	1.97	1	37.0	20.0	-39.0	0.61	0.67	0.13	0.68		ND
NYP106	2.36	2.05	1	39.0	21.0	-41.0	0.65	0.68	0.14	0.72		ND
Y01	2.75	2.75	1	40.0	40.0	-49.0	0.82	1.00	0.00	1.01		ND
Y02	2.67	2.67	1	39.0	39.0	-48.0	0.80	1.00	0.00	0.98		ND
Y03	2.92	2.92	1	43.0	43.0	-51.0	0.87	1.00	0.00	1.07		ND
Y04	2.84	2.84	1	42.0	42.0	-50.0	0.85	1.00	0.00	1.04		ND
Y05	3.13	3.13	1	47.0	47.0	-53.0	0.93	1.00	0.00	1.14		ND
Y06	3.11	3.11	1	46.0	46.0	-53.0	0.93	1.00	0.00	1.13		ND
Y07	3.11	3.11	1	46.0	46.0	-53.0	0.93	1.00	0.00	1.13		ND
Y08	3.10	3.10	1	46.0	46.0	-53.0	0.93	1.00	0.00	1.13		ND
Y09	2.94	2.94	1	44.0	44.0	-51.0	0.88	1.00	0.00	1.08		ND
Y10	3.00	3.00	1	44.0	44.0	-52.0	0.90	1.00	0.00	1.10		ND
Y11	3.00	3.00	1	44.0	44.0	-52.0	0.90	1.00	0.00	1.10		ND
Y12	2.76	2.76	1	41.0	41.0	-49.0	0.83	1.00	0.00	1.02		ND
Y13	2.92	2.92	1	43.0	43.0	-51.0	0.87	1.00	0.00	1.07		ND
72 PS SHALE	3.11	3.11	1	46.0	46.0	-53.0	0.93	1.00	0.00	1.13		ND
YS1	2.45	2.45	1	35.0	35.0	-45.0	0.73	1.00	0.00	0.90		ND
YS2	2.60	2.60	1	38.0	38.0	-47.0	0.78	1.00	0.00	0.96		ND
GR1	1.27	1.27	1	8.0	8.0	-15.0	0.20	1.00	0.00	0.24		ND
GR2	1.22	1.22	1	7.0	7.0	-12.0	0.16	1.00	0.00	0.20		ND
GR3	1.19	1.19	1	6.0	6.0	-11.0	0.14	1.00	0.00	0.17		ND
GR4	1.13	1.13	1	4.0	4.0	-8.0	0.10	1.00	0.00	0.12		ND
GR5	1.20	1.20	1	6.0	6.0	-12.0	0.15	1.00	0.00	0.18		ND
GR6	1.23	1.23	1	7.0	7.0	-13.0	0.17	1.00	0.00	0.21		ND
GR7	1.30	1.30	1	9.0	9.0	-16.0	0.21	1.00	0.00	0.26		ND
GR8	1.27	1.27	1	8.0	8.0	-15.0	0.20	1.00	0.00	0.24		ND
Mean Mud rocks	**2.11**	**1.93**	**1**	**30.7**	**20.2**	**-34.8**	**0.76**	**0.73**	**0.08**	**0.66**		

Appendix C (Table C.1) Continued

	Length			Apparent constant volume extension			Apparent Strain	Lodes			Total	Angle
Sample	X	Y	Z	X	Y	Z	Magnitude	Paremeter	E_1-E_2	E_2-E_3	Error	XY-Bedding
DS1	1.18	11.00	1	7.8	1.3	-8.4	0.12	0.24	2.23	2.40		28
DS4	1.31	1.06	1	17.4	-4.8	-10.5	0.20	-0.54	0.21	0.06		49
DS5	1.19	1.06	1	9.8	-1.6	-7.5	0.12	-0.28	0.12	0.06		44
DS7	1.25	1.18	1	9.5	3.8	-12.0	0.16	0.51	0.06	0.17		66
D8	1.35	1.18	1	15.8	0.7	-14.3	0.21	0.07	0.13	0.17		72
DS10	1.18	1.06	1	9.4	-1.7	-7.0	0.12	-0.32	0.11	0.06		88
DS11	1.25	1.20	1	8.9	5.1	-12.6	0.17	0.67	0.04	0.18		42
PP1	1.50	1.20	1	23.3	-1.4	-17.8	0.29	-0.10	0.22	0.18		5
PP2	1.23	1.07	1	12.2	-2.4	-8.8	0.15	-0.35	0.14	0.07		28
PP3	1.13	1.06	1	6.4	-0.2	-5.8	0.09	-0.05	0.06	0.06		20
PP4	1.17	1.08	1	8.2	-0.1	-7.5	0.11	-0.02	0.08	0.08		56
PP5	1.24	1.05	1	13.6	-3.8	-8.4	0.16	-0.55	0.17	0.05		19
PP6	1.15	1.03	1	8.7	-2.7	-5.5	0.10	-0.58	0.11	0.03		33
PP7	1.18	1.17	1	6.0	5.1	-10.2	0.13	0.90	0.01	0.16		35
PP8	1.31	1.16	1	13.9	0.9	-13.0	0.19	0.10	0.12	0.15		16
PP9	1.30	1.16	1	13.4	1.2	-12.8	0.19	0.33	0.11	0.15		86
PP10	1.27	1.17	1	11.3	2.5	-12.4	0.17	0.31	0.08	0.16		52
GVS1	1.97	1.34	1	42.5	-3.0	-27.6	0.48	-0.14	0.39	0.29		ND
GVS3	2.17	1.43	1	48.8	-2.0	-31.4	0.55	-0.08	0.42	0.36		ND
GVS5	1.27	1.02	1	16.5	-6.4	-8.3	0.19	-0.83	0.22	0.02		ND
GVS7	1.40	1.10	1	21.2	-4.8	-13.4	0.25	-0.43	0.24	0.10		ND
GVS9	1.81	1.34	1	34.7	-0.3	-25.6	0.42	-0.01	0.30	0.29		ND
GVS11	1.44	1.13	1	22.4	-3.9	-15.0	0.26	-0.33	0.24	0.12		ND
GVS13	1.44	1.13	1	22.4	-3.9	-15.0	0.26	-0.33	0.24	0.12		ND
GVS15	1.39	1.25	1	15.6	4.0	-16.8	0.24	0.36	0.11	0.22		ND
GVS20	1.30	1.20	1	12.3	3.2	-13.8	0.19	0.36	0.08	0.18		63
GVS21	1.18	1.10	1	8.4	0.5	-8.2	0.12	0.09	0.07	0.10		20
GVS22	1.18	1.03	1	10.3	-3.2	-6.4	0.12	-0.59	0.14	0.03		34
GVS24	1.09	1.02	1	5.4	-1.8	-3.4	0.07	-0.61	0.07	0.02		51
GVS26	1.27	1.14	1	12.6	0.4	-11.5	0.17	0.05	0.11	0.13		20
GVS28	1.08	1.04	1	3.8	0.1	-3.8	0.05	0.06	0.04	0.04		52
GVS29	1.18	1.13	1	6.9	3.0	-9.2	0.12	0.43	0.04	0.12		31
GVS31	1.23	1.15	1	9.5	2.4	-10.8	0.15	0.35	0.07	0.14		ND
GVS33	1.17	1.09	1	7.4	0.5	-7.7	0.11	0.10	0.07	0.09		33
GVS35	1.16	1.15	1	5.2	4.5	-9.0	0.12	1.09	0.01	0.14		35
AUS	1.11	1.10	1	3.8	2.9	-6.3	0.08	0.82	0.01	0.10		ND
RR1	1.24	1.09	1	12.5	-1.7	-9.6	0.16	-0.24	0.13	0.09		70
RR2	1.11	1.09	1	4.5	2.0	-6.2	0.08	0.56	0.02	0.09		76
RR3	1.31	1.27	1	10.2	7.5	-15.6	0.21	0.81	0.03	0.24		60
RR4	1.15	1.07	1	7.4	-0.2	-6.7	0.10	-0.04	0.07	0.07		53
Io-1	1.19	1.16	1	6.9	4.2	-10.2	0.13	0.71	0.03	0.15		ND
Io-2	1.94	1.43	1	38.1	1.8	-28.8	0.47	0.08	0.31	0.36		ND
BD-1	1.19	1.08	1	9.5	-0.7	-8.0	0.12	-0.12	0.10	0.08		ND
Mean Sandstones	**1.31**	**1.37**	**1**	**13.8**	**0.2**	**-11.7**	**0.18**	**0.06**	**-0.05**	**0.32**		

Table C.2. Apparent grain shape ellipsoid (AGSE) data measured in the volcanic and volcaniclastic samples.

	Length			Apparent constant volume extension			Apparent Strain	Lodes			Total
Sample	X	Y	Z	X	Y	Z	Magnitude	Paremeter	E_1-E_2	E_2-E_3	Error
188-L	1.7	1.3	1	31.6	0.0	-24.0	0.39	0.00	0.28	0.28	0.07
192-L	1.6	1.3	1	27.3	0.7	-22.0	0.35	0.04	0.23	0.26	0.06
193-L	2.1	1.5	1	40.9	3.6	-31.5	0.51	0.15	0.31	0.41	0.07
194-L	1.6	1.2	1	26.9	-3.1	-18.7	0.32	-0.21	0.27	0.18	0.11
195-L	1.7	1.3	1	32.3	-0.5	-24.0	0.39	-0.03	0.29	0.27	0.06
200-L	1.6	1.3	1	26.5	0.0	-20.8	0.33	-0.02	0.24	0.23	0.06
202-L	1.8	1.3	1	34.8	-0.1	-25.7	0.42	-0.01	0.30	0.30	0.07
203-L	1.5	1.3	1	18.3	5.2	-19.6	0.28	0.39	0.12	0.27	0.10
218-L	1.8	1.3	1	34.8	-0.2	-25.6	0.42	-0.01	0.30	0.29	0.08
221-L	1.4	1.0	1	21.5	-8.1	-10.4	0.24	-0.83	0.28	0.03	0.27
P-4-L	1.5	1.2	1	22.4	-0.6	-17.8	0.28	-0.05	0.21	0.19	0.10
PHW-2-24-A-L	1.7	1.2	1	32.1	-3.4	-21.7	0.37	-0.20	0.31	0.21	0.08
PHW-2-24-B1-L	1.6	1.2	1	27.8	-2.9	-19.4	0.33	-0.19	0.27	0.19	0.08
PHW-2-24-B2-L	1.7	1.3	1	31.2	-0.4	-23.5	0.38	-0.02	0.28	0.26	0.06
PHW2-24-B3-L	1.6	1.3	1	29.3	-1.3	-21.6	0.35	-0.08	0.27	0.23	0.17
PHW-2-24-B4-L	2.0	1.4	1	40.5	0.2	-29.0	0.48	0.01	0.34	0.35	0.07
PHW-2-24-B6-L	1.6	1.2	1	29.1	-3.9	-19.4	0.34	-0.25	0.29	0.18	0.07
PHW-2-24-C1-L	1.8	1.3	1	33.3	-0.1	-25.0	0.41	0.00	0.29	0.29	0.09
PHW-2-24-C-L	1.9	1.1	1	46.0	-12.7	-21.7	0.47	-0.65	0.51	0.11	0.11
PHW-2-25-A1-L	1.8	1.3	1	32.6	0.6	-25.0	0.40	0.03	0.27	0.29	0.08
PHW-2-25-A2-L	1.6	1.2	1	30.6	-3.5	-20.7	0.36	-0.21	0.30	0.20	0.11
PHW-2-25-A-L	1.6	1.3	1	23.5	2.0	-20.7	0.31	0.14	0.19	0.25	0.08
PHW-2-25-C-L	1.8	1.4	1	32.2	1.1	-25.1	0.40	0.06	0.27	0.30	0.08
PHW-UNKNOWN-L	1.7	1.4	1	30.1	2.3	-24.8	0.39	0.12	0.24	0.31	0.07
Mean Lithics	**1.7**	**1.3**	**1**	**30.6**	**-1.0**	**-22.4**	**0.37**	**-0.08**	**0.28**	**0.24**	**0.09**
218-Plag	1.7	1.3	1	30.7	-2.1	-21.9	0.37	-0.12	0.29	0.23	0.11
PHW-2-24-B3-Plag	2.8	1.7	1	67.9	-0.7	-40.0	0.73	-0.02	0.53	0.50	0.12
PHW-2-25-A-PLAG	1.5	1.2	1	20.0	1.1	-17.6	0.27	0.09	0.17	0.20	0.06
PHW-2-25-C-PLAG	2.3	1.4	1	53.5	-3.8	-32.3	0.58	-0.14	0.47	0.35	0.08
PHW-UNKNOWN-PLAG	1.7	1.3	1	29.3	-1.0	-21.9	0.36	-0.06	0.27	0.24	0.08
PST-SAN	2.1	1.3	1	50.4	-6.8	-28.6	0.53	-0.29	0.48	0.27	0.12
Mean Plag	**2.0**	**1.4**	**1**	**42.0**	**-2.2**	**-27.0**	**0.47**	**-0.09**	**0.37**	**0.30**	**0.10**
212-HBL	1.6	1.2	1	28.6	-1.7	-20.8	0.34	-0.11	0.27	0.22	0.08
240-HBl	1.5	1.1	1	29.4	-9.6	-14.6	0.32	-0.73	0.36	0.06	0.14
PHW-2-24-B-HBL	1.6	1.2	1	27.3	-2.3	-19.6	0.33	-0.15	0.26	0.20	0.11
Mean HBL	**1.6**	**1.2**	**1**	**28.4**	**-4.5**	**-18.3**	**0.33**	**-0.33**	**0.30**	**0.16**	**0.11**

Appendix C (Table C.2) Continued

	Length			Apparent constant volume extension			Apparent Strain	Lodes			Total
Sample	X	Y	Z	X	Y	Z	Magnitude	Paremeter	E_1-E_2	E_2-E_3	Error
184-Q	1.7	1.3	1	33.3	-2.1	-23.4	0.39	-0.12	0.31	0.25	0.02
186-Q	1.8	1.3	1	35.8	-2.4	-24.5	0.42	-0.13	0.33	0.26	0.10
188-Q	1.4	1.2	1	18.5	-1.2	-14.6	0.23	-0.11	0.18	0.15	0.04
189-Q	1.5	1.2	1	22.1	-1.0	-17.3	0.28	-0.08	0.21	0.18	0.06
192-Q	1.6	1.2	1	25.9	-1.7	-19.2	0.31	-0.12	0.25	0.20	0.10
193-Q	1.5	1.3	1	22.7	1.3	-19.5	0.30	0.09	0.19	0.23	0.05
194-Q	1.6	1.3	1	27.5	-0.4	-21.2	0.34	-0.03	0.25	0.23	0.05
195-Q	1.6	1.2	1	27.5	-1.4	-20.5	0.33	-0.09	0.26	0.22	0.06
196-Q	1.8	1.3	1	35.0	-1.5	-24.8	0.41	-0.08	0.32	0.27	0.08
198-Q	1.9	1.3	1	42.0	-5.4	-25.6	0.46	-0.26	0.41	0.24	0.02
200-Q	1.5	1.2	1	19.6	1.8	-17.9	0.27	0.14	0.16	0.22	0.05
202-Q	1.5	1.2	1	21.5	-1.7	-16.3	0.26	-0.14	0.21	0.16	0.05
203-Q	1.5	1.2	1	20.8	0.0	-17.2	0.27	0.00	0.19	0.19	0.05
220-Q	1.8	1.3	1	33.3	0.4	-25.3	0.41	0.02	0.28	0.30	0.13
221-Q	1.8	1.3	1	35.7	-0.4	-26.0	0.43	-0.02	0.31	0.30	0.05
229-Q	1.4	1.2	1	20.4	-0.8	-16.3	0.26	-0.07	0.19	0.17	0.06
262-Q	1.4	1.2	1	20.2	0.2	-17.0	0.26	0.02	0.18	0.19	0.07
P-4-Q	1.6	1.3	1	26.5	0.4	-21.2	0.34	0.02	0.23	0.24	0.06
PHW-2-25-A2-Q	1.7	1.3	1	32.2	-0.7	-23.8	0.39	-0.04	0.29	0.27	0.07
Mean Quartz	**1.6**	**1.3**	**1**	**27.4**	**-0.9**	**-20.6**	**0.33**	**-0.05**	**0.25**	**0.22**	**0.06**
184-P	1.4	1.2	1	17.6	0.0	-14.9	0.23	0.00	0.16	0.16	0.20
186-P	3.4	1.7	1	88.3	-5.2	-44.0	0.86	-0.13	0.69	0.53	0.08
188-P	2.7	1.3	1	77.3	-14.3	-34.2	0.73	-0.47	0.73	0.26	0.17
189-P	3.8	1.6	1	107.6	-12.4	-45.0	0.95	-0.30	0.86	0.47	0.23
192-P	1.9	1.3	1	40.2	-3.6	-26.0	0.45	-0.17	0.37	0.27	0.09
193.P	4.8	3.3	1	91.0	31.5	-60.2	1.16	0.52	0.37	1.19	0.07
194-P	4.1	3.1	1	74.5	33.8	-57.1	1.06	0.62	0.27	1.14	0.11
195-P	2.9	1.2	1	91.2	-21.2	-33.6	0.80	-0.68	0.89	0.17	0.14
196-P	5.1	1.8	1	143.0	-13.2	-52.6	1.17	-0.26	1.03	0.60	0.28
198-P	2.1	1.4	1	47.0	-3.2	-29.8	0.52	-0.13	0.42	0.32	0.05
200-P	2.7	1.7	1	61.7	2.0	-39.4	0.69	0.06	0.46	0.52	0.08
202-P	3.4	1.4	1	99.1	-14.9	-41.0	0.88	-0.40	0.85	0.37	0.17
203-P	2.0	1.2	1	48.3	-8.3	-26.5	0.51	-0.37	0.48	0.22	0.25
212-P	1.8	1.2	1	36.4	-5.6	-22.3	0.40	-0.31	0.37	0.19	0.08
262-P	1.9	1.2	1	42.6	-8.3	-23.6	0.45	-0.41	0.44	0.18	0.11
PHW-UNKNOWN-P	3.6	2.0	1	86.6	3.2	-48.1	0.91	0.07	0.59	0.69	0.13
PST-P	3.8	1.7	1	105.4	-9.7	-46.1	0.95	-0.23	0.82	0.52	0.27
Mean Pumic	**3.0**	**1.7**	**1**	**74.0**	**-2.9**	**-37.9**	**0.75**	**-0.15**	**0.58**	**0.46**	**0.15**
PP1	1.7	1.3	1	31.6	-2.1	-22.4	0.37	-0.25	0.30	0.23	0.08
PP2	1.7	1.3	1	33.3	-3.2	-22.5	0.39	-0.31	0.32	0.22	0.06
PP3	1.6	1.2	1	29.5	-3.4	-20.1	0.34	-0.33	0.29	0.19	0.06
PP4	1.7	1.3	1	28.9	-0.7	-21.9	0.35	-0.17	0.26	0.24	0.05
PP5	1.7	1.3	1	30.3	-0.7	-22.8	0.37	-0.17	0.27	0.25	0.08
PP6	1.8	1.3	1	36.8	-2.1	-25.4	0.43	-0.25	0.33	0.27	0.06
PP7	1.7	1.3	1	28.7	0.3	-22.5	0.36	-0.11	0.25	0.26	0.07
PP8	1.8	1.3	1	35.2	-2.5	-24.2	0.41	-0.27	0.33	0.25	0.07
PP9	1.8	1.3	1	36.3	-2.4	-24.8	0.42	-0.27	0.33	0.26	0.06
PP10	1.6	1.3	1	28.3	-0.9	-21.4	0.35	-0.17	0.26	0.23	0.09
Mean Sandstone	**1.7**	**1.3**	**1**	**31.9**	**-1.8**	**-22.8**	**0.38**	**-0.23**	**0.29**	**0.24**	**0.07**